3D Printed Metal and Metal-Ceramic Cellular Lattice Structures for Wear and Thermoacoustic Applications

YAROSLAV HOLOVENKO

**TAL
TECH** PRESS

TALLINN UNIVERSITY OF TECHNOLOGY
School of Engineering
Department of Mechanical and Industrial Engineering
This dissertation was accepted for the defence of the degree 30/04/2019

Supervisors: Prof. Renno Veinthal
                                         Department of Mechanical and Industrial Engineering
                                         School of Engineering, Tallinn University of Technology
                                         Tallinn, Estonia

Co-supervisor: Dr. Lauri Kollo
                                         Department of Mechanical and Industrial Engineering
                                         School of Engineering, Tallinn University of Technology
                                         Tallinn, Estonia

Opponents: Prof. Paolo Colombo
                                         Centre for Mechanics of Biological Materials
                                         University of Padova
                                         e-mail: paolo.colombo@unipd.it

                                         Arkadi Žikin, PhD
                                         Head of Technology / Laser Surface Engineering / Laser
                                         Cladding. Oerlikon Solutions
                                         Arkadi.zikin@oerlikon.com

Defence of the thesis: 19/06/2019, Tallinn

Declaration:
Hereby I declare that this doctoral thesis, my original investigation and achievement, submitted for the doctoral degree at Tallinn University of Technology has not been submitted for doctoral or equivalent academic degree.

Yaroslav Holovenko

                                         _____
                                                             signature

3D prinditud metall- ja metall-keraamilised kärgvõre struktuurid triboloogilistele- ja termoakustilistele rakendustele

YAROSLAV HOLOVENKO

**TAL
TECH**
KIRJASTUS

Contents

List of Publications

The list of author's publications, on the basis of which the thesis has been prepared:

I   **Holovenko, Y.**; Kollo, L.; Jõeleht, M.; Pohlak, M.; Veinthal, R., Effect of Hot Isostatic Pressing on Cellular Lattice Structures Obtained by Selective Laser Melting. *World PM2016 proceedings: World PM2016 Congress & Exhibition, Hamburg, Germany, 9-13 October 2016. European Powder Metallurgy Association,* (2016), USB.

II **Holovenko, Y**; Kollo, L; Jõeleht, M; Ivanov, R; Soloviova, T; Veinthal, R., Production of metal-ceramic lattice structures by selective laser melting and carburizing or nitriding. *Proceedings of the Estonian Academy of Sciences*, 68 (2), (2019), 131–139.

III **Holovenko, Y.**; Antonov, M.; Kollo, L.; Hussainova, I., Friction studies of metal surfaces with various 3D printed patterns tested in dry sliding conditions. *Proceedings of the Institution of Mechanical Engineers, Part J: Journal of Engineering Tribology*, 232 (1), (2018), 43–53.

IV Auriemma, Fabio; **Holovenko, Yaroslav**, Performance of Additive Manufactured Stacks in a Small Scale Thermoacoustic Heat Engine. *SAE Technical Paper 2019-01-1534*, (2019), 1–9.

Author's Contribution to the Publications

In the papers listed in the previous section, the author of the present doctoral thesis has designed and conducted the experiment; made results analysis and data visualization; prepared and wrote original drafts; and was involved in the revision of the final paper versions.

Contribution to the papers:

I   First author. Design and production of cellular lattice structures; definition of the dependence between process parameters and lattice feature characteristics; mechanical properties testing; analysis of the results. Manuscript preparation.

II First author. Design and production of cellular lattice structures; choosing the post processing parameters; mechanical properties testing; analysis of the results. Manuscript preparation.

III First author. Design and production of patterned surfaces for abrasive wear testing; investigation of worn surfaces; analyzing of the results. Manuscript preparation.

IV Co-author. Design and production of various stacks for thermoacoustic heat engine, including cellular lattice structures; analyzing of the results. Partially drafting the manuscript.

Other author's publications

List of author's publications, not included into the thesis:

1. Jaworska, L.; Cyboron, J.; Cygan, S.; Laszkiewicz-Lukasik, J.; Podsiadlo, M.; Novak, P.; Holovenko, Y., New materials through a variety of sintering methods. *IOP Conference Series: Materials Science and Engineering*, 329 (1), (2018), 012004.

2. Holovenko, Y.; Kollo, L.; Jõeleht, M.; Soloviova, T.; Veinthal, R., Evaluation of titanium matrix composites with additions of 5 vol. % B4C and TiC processed via Selective Laser Melting. *EuroPM 2018 proceedings: Euro PM2018 Congress & Exhibition, Bilbao, Spain, 14 - 18 October 2018. European Powder Metallurgy Association (EPMA)*, (2018), USB.

3. Auriemma, F.; Holovenko, Y., Use of Selective Laser Melting for Manufacturing the Porous Stack of a Thermoacoustic Engine. In: K. Karjust, J. Kübarsepp, T. Otto, I. Hussainova (Ed.). *Modern Materials and Manufacturing, Trans Tech Publications. (Key Engineering Materials),* (2019), 246–251.

4. Antonov, M.; Ivanov, R.; Holovenko, Y.; Goljandin, D.; Rahmaniahranjani, R.; Kollo, L.; Hussainova, I., 3D printing of plain and gradient cermets with efficient use of raw materials. In: K. Karjust, J. Kübarsepp, T. Otto, I. Hussainova (Ed.). *Modern Materials and Manufacturing, Trans Tech Publications. (Key Engineering Materials),* (2019), 239–245.

5. Minasyan, T.; Liu, L.; Holovenko, Y.; Aydinyan, S.; Hussainova, I. Additively manufactured mesostructured MoSi2-Si3N4 ceramic lattice. *Ceramics International*, 45, (2019), 9926–9933.

Intellectual property:

1. Invention: Multifunctional composite material and method for its preparation; Owners: Tallinna Tehnikaülikool; Authors: Maksim Antonov, Yaroslav Holovenko; Priority number: P201900006; Priority date: 24.01.2019.

PARTICIPATION AT INTERNATIONAL CONFERENCES

1. World PM2016 Congress & Exhibition, Hamburg, Germany, October 9 – 13, 2016. (Oral presentation)

2. E-MRS 2017 Fall Meeting, Symposium "Solutions for Critical Raw Materials Under Extreme Conditions", Warsaw, Poland, September 18 – 21, 2017. (Oral presentation)

3. Euro PM2018 Congress & Exhibition, Bilbao, Spain, October 14 – 18, 2018. (Oral presentation)

4. 11th International Conference on the Science of Hard Materials (ICSHM11), Khao Lak, Thailand, March 25 – 29, 2019. (Oral presentation)

5. Modern Materials and Manufacturing, Tallinn, Estonia, April 23-26, 2019. (Oral presentation)

Introduction

In 1981 the idea of fabricating a plastic object layer by layer was first published [1]. A few years later, in 1984, stereolithography, the first 3D-printing technique was invented [2]. Almost a decade later, in 1992, the world's first selective laser sintering (SLS) machine was produced. The main idea was in using of powder feedstock instead of liquid photopolymer and applying laser exposure in order to sinter powder particles.

The proposed technology was slow and had many quality problems, but its potential was undeniable. From that time on, the additive manufacturing (AM) technology was developed and adapted for producing fully dense metal parts, some types of ceramics, etc. However, the full potential of AM is still unfolding and plenty of related engineering challenges have remained unsolved.

During the last 15 years, AM technology has shown a rapid development. Progress in additive manufacturing has made it possible to produce complex geometrical shapes such as cellular lattice structures [3–5]. These structures have a great industrial potential. The lattice structures can increase the efficiency of aerospace parts by weight reduction, which leads to reduced fuel consumption [6] as one of the aspects. Also, lattice structures reduce production time of medical implants, they can improve the material properties by acting in the role of reinforcing frame in IPCs [7,8]. However, their full potential has not been disclosed yet. Application areas of such lightweight lattice structures can be expanded, first of all, by understanding the lattice performance in specific working conditions. They can be beneficial in tribology [9] and thermoacoustics [10].

Extension of the lifetime of the parts is an important task. It can be achieved by providing low friction coefficients or high wear resistance of the material or simultaneous combination of both.

Precise control of the lattice geometry is vital for thermoacoustic applications. Thin struts combined with low thermal conductivity should improve thermoacoustic performance.

AISI 316L, one of the most common materials for metal AM, was considered perfectly suitable in the initial stage of investigations due to high manufacturability. In order to solve initial challenges for the application of the lattices, it is required to conduct the thermoacoustic parametric studies. For tribology, the patterning of the surface with cellular lattice structures should be tested. AM is not widely spread in mass production due to slow production speed and high cost. A possible solution to overcome this problem is to combine the conventional fast and cheap production process with AM in order to add lattice structures to the green part only in the places where necessary. Directed energy deposition (DED) provides the possibility of manufacturing cellular lattice structures on the surface of a green part with the almost arbitrary initial shape. It gives a capability for combining traditional production techniques with AM, which can be time and cost efficient.

Lattice structures made from ceramic or metal-ceramic should increase both wear resistance and thermoacoustic performance. However, the fabrication of ceramics or metal-ceramics via direct AM is a difficult and challenging task. That is why a two-step approach was introduced in this work. Additively manufactured cellular lattice structures were post-treated by nitriding and carburizing to obtain a metal-ceramic composite.

List of abbreviations

3DP	Three Dimensional Printing
AM	Additive Manufacturing
COF	Coefficient of Friction
DED	Directed Energy Deposition
EBM	Electron Beam Melting
EDS	Energy-dispersive X-ray spectroscopy
ET	Exposure Time
FDM	Fused Deposition Modelling
FS	Functional Surface
FV	Functional Volume
IPC	Interpenetrating Phase Composite
LMD	Laser Metal Deposition
LP	Laser Power
PBF	Powder Bed Fusion
PD	Point Distance
SEM	Scanning Electron Microscope (-y)
SLA	Stereolithography
SLM	Selective Laser Melting
SLS	Selective Laser Sintering
TAE	Thermo-acoustic Engine
XRD	X-ray diffraction

1 LITERATURE OVERVIEW

This chapter provides a theoretical background of the powder based additive manufacturing (AM) process and the production of complex geometries such as lattice structures. Materials, microstructure, methods of manufacture, challenges, applications, and costs will be covered. A brief AM history and recent trends in the area will be presented.

1.1 Additive manufacturing techniques for the production of cellular lattice structures

The main advantage of additive manufacturing is its ability to produce parts with complex geometrical shapes that cannot be produced by traditional manufacturing techniques and processes such as casting, forging, injection molding, welding, etc. [11–13]. General classification of AM techniques is presented in Figure 1.1. The AM methods used in the present study are highlighted in red.

Melt-extrusion techniques extrude a material through a nozzle onto a build platform. The moving elements follow a predetermined path building layer-by-layer. The moving element can be a nozzle or a nozzle and a platform simultaneously. Fused deposition modelling (FDM) is the most popular and widespread 3D printing technique. FDM builds parts using solid thermoplastic filaments. The raw materials for some FDM machines can also come as granulated feedstock.

Photosensitive techniques use a photopolymer resin sensitive to the light of a specific wavelength. The light influences a liquid polymer and solidification happens due to a chemical reaction called photopolymerization. In specific cases, it allows building up the whole layer at a time and drastically increases the building speed. This process can be also performed continuously without pauses between layers.

One of the powder based techniques is binder jetting. It uses a binding agent distributed onto a powder bed to build a solid component layer-by-layer. Usually the powders are ceramics or metals. The print head moves over the powder bed, depositing binder droplets. The process of printing is very similar to regular paper 2D printers that are using inks. After the process, the formed green parts require additional post-processing. Often the parts have to be infiltrated by another material (e.g. bronze) to achieve the full density.

Powder Bed Fusion (PBF) produces a solid part using an energy source that causes the fusion (sintering or melting) among the metal or plastic powder particles. A thin layer of powder is spread, followed by the fusion process until the whole part is fabricated. After the process, the final component has to be extracted from the powder and separated from the building platform if needed. As an energy source, lasers or electron beam guns are employed.

Directed energy deposition (DED) creates parts by melting powder material or wire using a laser as an energy source. The powder is delivered through the nozzle and interacts with the laser beam. Quite often it is also referred to as laser metal deposition (LMD). Figure 1.2 gives a general overview of the lattices produced by different AM techniques. A general view can provide a rough estimation of the printing resolution, the quality of the parts, surface roughness and defects.
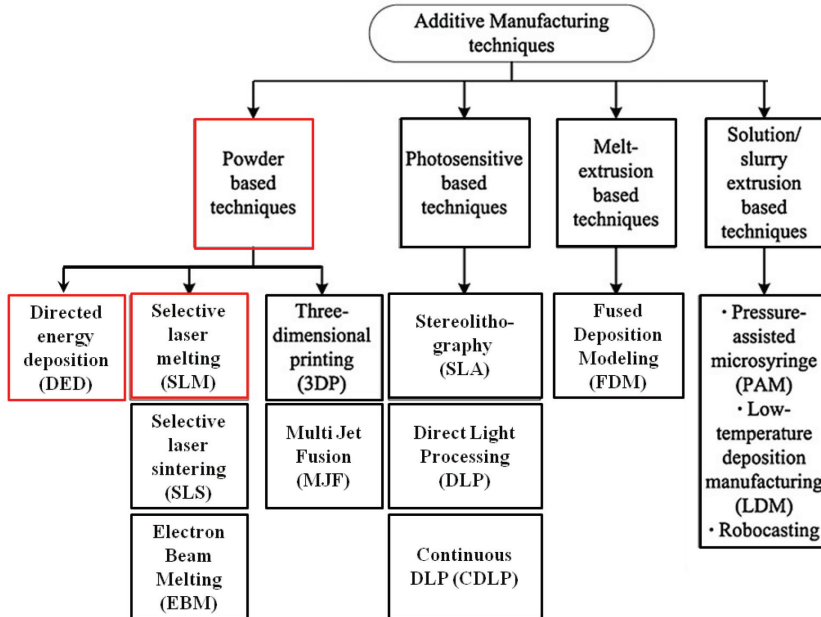
Figure 1.1 General classification of AM techniques (adapted from [14]*).*

The present study is focused on the AM processes that use a laser beam as an energy source. The reason behind this is the ability of employing a pulsed laser scanning strategy which can provide the smallest features. The EBM was not considered for such applications in this study.
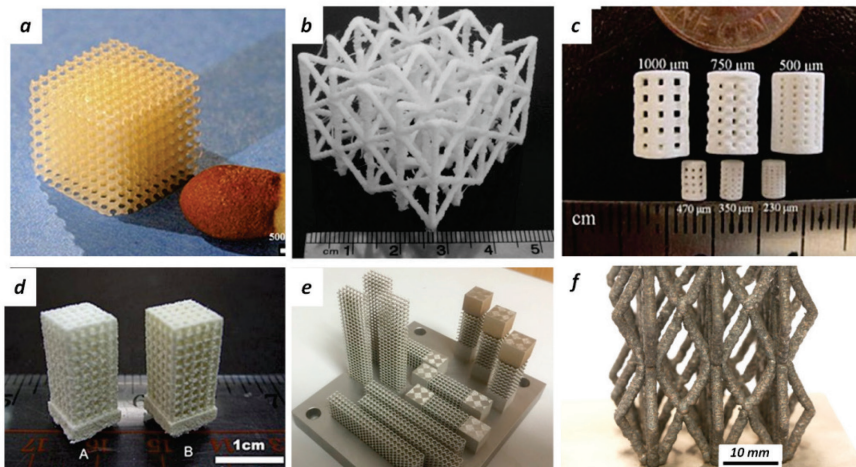
Figure 1.2 General view of cellular structures produced by different AM techniques, SLA (a)[15]*, FDM (b)*[16]*, 3DP(c)*[17]*,SLS (d)*[18]*, SLM (e)*[19]*, and DED (f)* [20]*.*

1.1.1 Powder based additive manufacturing

Metal AM system may be classified/categorized in terms of the material feedstock, energy source, build volume, etc. [21]. In terms of the material feedstock, metallic AM systems are preferably powder or wire based. Powder based AM may be divided into

powder bed and powder feed systems. Each one has its own advantages and disadvantages that define their possibilities and limitations in industrial application. A generic illustration of powder bed and powder feed processes is presented in Figure 1.3.

The work principle of the powder bed systems is illustrated in Figure 1.3 a. The main advantage of powder bed systems over powder feed systems is the ability to produce high-resolution features, internal elements, and ability for precise dimensional control. The main disadvantage is the low speed of the process.

In the powder feed systems, the powder is delivered through a nozzle and simultaneously irradiated by a laser beam, and is deposited on the building substrate (Fig. 1.3 b). A single layer consists of a set of melted tracks. The process is repeated layer over layer in order to build a final three-dimensional part. The main advantage of the powder feed process is large build volumes, high production speeds and the ability to be used for recovering and repairing of worn or damaged components. The main disadvantage is the low resolution and the necessity for mechanical post treatment.

Two main scanning approaches, modulated or continuous laser scanning, can be used. Figure 1.4 illustrates both of the approaches schematically. The modulated mode can also be named as a pulsed laser mode. It is realized by performing a series of laser exposures with a certain distance between them. Each exposure spot has to overlap the previous one partially.
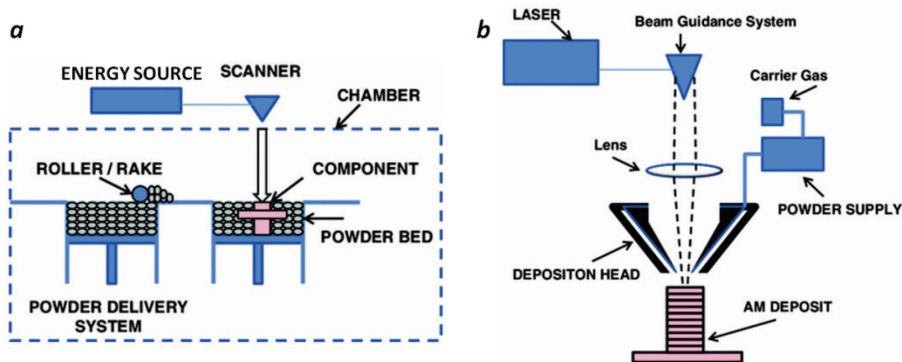
Figure 1.3 A generic illustration of the powder bed (a) and the powder feed (b) processes [21]*.*

The continuous mode operates a laser such that the laser continuously melts the whole line (track). The scanning tracks overlap with each other, so that each next track partially re-melts the previous one. The powder feed systems are easier to operate in a continuous laser scanning mode while powder bed systems are operated by a modulated laser mode.
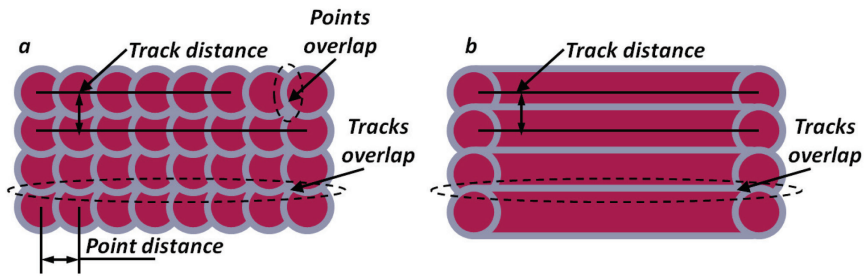
Figure 1.4 Schematic illustrations of the scanning tracks by modulated (a) and continuous (b) laser.

Selective laser melting is the powder bed process used in the present work. SLM process parameters generally define the quantity of laser energy applied to the powder bed and the speed of the process. The main process parameters are:
   • Laser spot size
   • Laser power (LP)
   • Scanning speed (in the present machine defined as point distance (PD) to exposure time (ET) ratio)
   • Hatch distance
   • Layer thickness
In the general case, the operating window of the process parameters can be defined for each specific material. The material density is the main indicator of the quality of the produced part and the efficiency of the process parameters.

The basic idea of the selection of the process parameters is presented in Figure 1.5. Low laser power leads to insufficient penetration of the laser energy in the powder layer, which leaves unmelted powder between layers (pointed as 1 in Fig. 1.5). It results in a printing job failure or weakness in the component. By caption 2 in Figure 1.5, efficient processing inside the so-called operating window is defined. An operating window is an optimal combination of the scanning speed and the laser power. Increased laser power and intense laser spot lead to forming a deep cavity, also known as keyhole effect (3 and 4 in Fig. 1.5.). If the cavity is large, it causes gas trapping in a pore below the solidified metal surface. Extremely fast scanning speed provides an unstable melt pool (Fig. 1.5, caption 5).
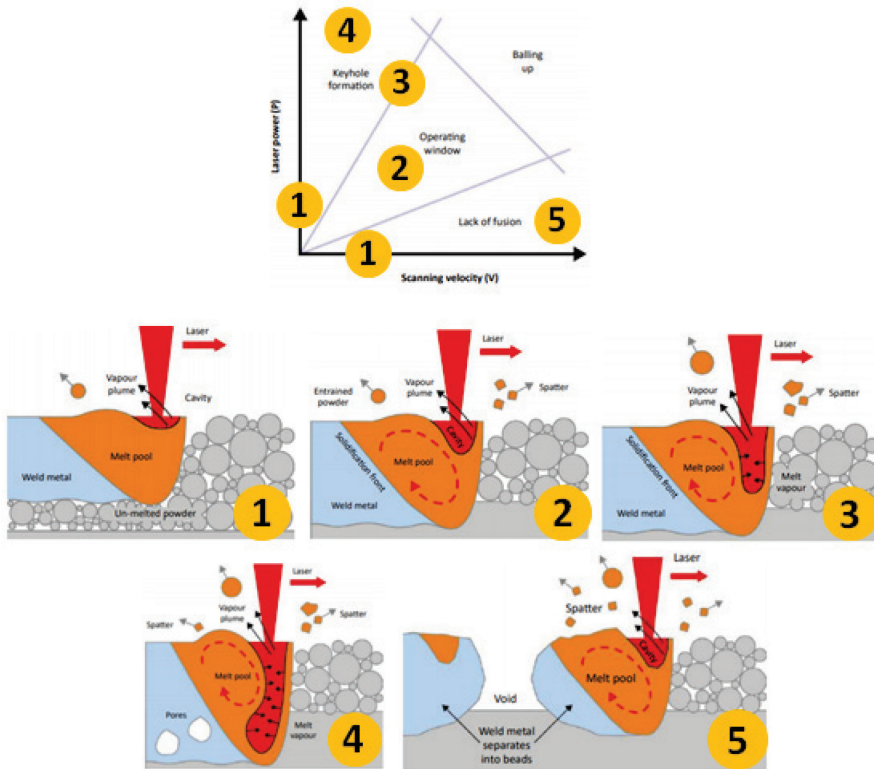
Figure 1.5 Process parameters selection for obtaining solid models via SLM (adapted from [22]*).*

High build rates, which can be provided by powder feed systems, matter for the production of large volumes [23]. Building rate and feature definition are closely linked to each other. The dependence is illustrated in Figure 1.6. These are also defining the surface quality of the part.
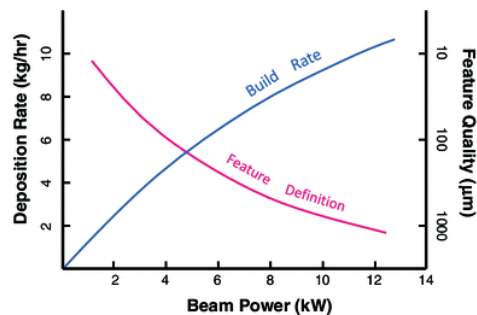
Figure 1.6 General relationship between the build rate and the feature definition [21]*.*

A laser metal deposition, the directed energy deposition powder feed process, was used in the present study. The main process parameters for LMD are:
- Laser spot size
- Laser power
- Scanning speed
- Powder flow rate

These parameters define the single track geometry. Hatch distance and layer thickness depend on the single track geometry.

1.2 Cellular Materials

A cellular solid material is necessarily composed of two phases, one continuous solid phase and the other either continuous or discontinuous gaseous phase. The presence of a gaseous phase makes cellular materials lighter than their former solids. This simple fact involves weight reduction together with a diminution of the amount of raw materials employed, which, in many cases, implies costs savings [24]. Examples of such materials are shown in Figure 1.7. Nowadays, different cellular structures can be produced by various industrial methods.

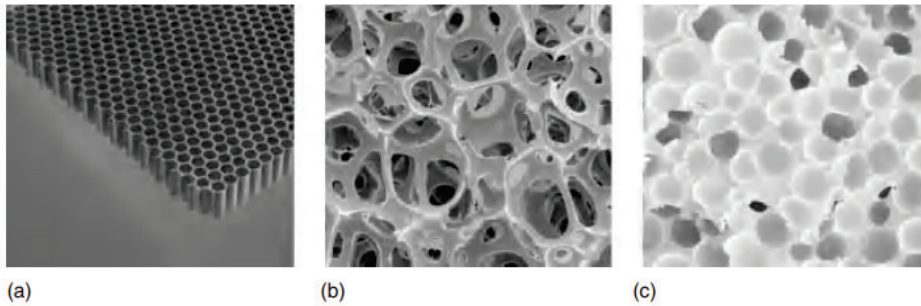(a)   (b)   (c)

Figure 1.7 Examples of cellular structures: honeycomb structure (a), open cell (b), and closed cell (c) foam [24].
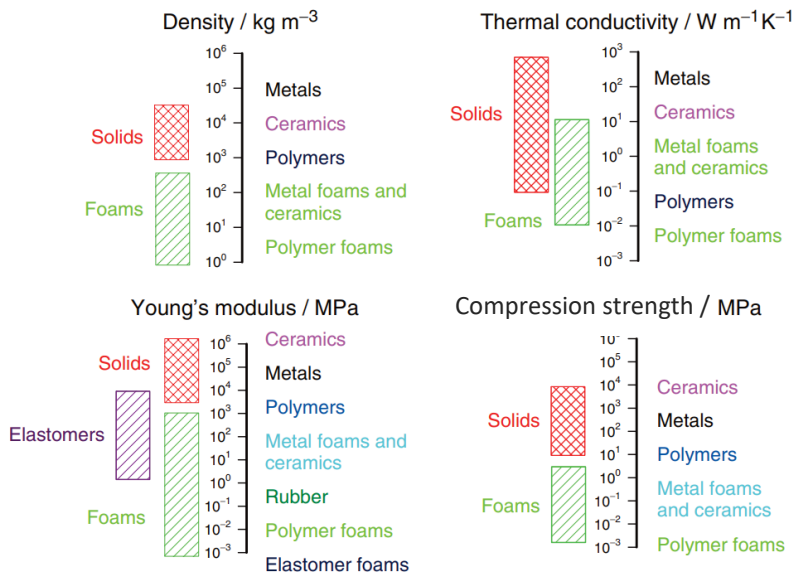

Figure 1.8 Properties of cellular materials [24].

Cellular materials exhibit a unique set of properties that regular solids cannot achieve. The specific characteristics include low thermal conductivity, high energy

absorption and high acoustic absorption. Figure 1.8 summarizes the properties of cellular materials in comparison with solid materials.

1.2.1 Classification of cellular materials

Classification of cellular materials may be composed of various factors. The overall cellular materials can be classified by origin into two main categories: natural and artificial. The main representative examples of natural cellular materials are wood, cork, human bones, etc. Artificial cellular materials are industrially produced (e.g. foams). By periodical characteristics, they may be divided into prismatic (two-dimensional, where the unit cell is translated in two dimensions) and three-dimensional (characterized by three-dimensional periodicity) materials. The most popular classification of the pore type divides such materials into open and closed cellular structures. The open cellular structure is characterized by a continuous gas phase inside the solid one. The closed cellular structure keeps the gas inside the pores, so the solid phase is continuous and a gaseous phase is discontinuous. However, most of the produced cellular materials are characterized by the presence of open cellular and closed cellular pores simultaneously. Cellular materials also differ in porosity distribution. Materials which do not have a single unit cell and are characterized by random porosity distribution (e.g. foams) are called stochastic. Cellular materials characterized by the presence of a unit cell that is translated in the space are referred to as periodic structures. The specific geometry of cellular materials can add additional restrictions to the production route etc. For example, the concept "foam" refers to materials obtained from a liquid state (molten material) and a random porous structure should be provided. Cellular lattice structures in contrast to foams have ordered and precisely controlled geometry that requires a specific production method. The most efficient way to obtain such structures is additive manufacturing. Figure 1.9 represents the classification and the place of cellular lattice structures in there.
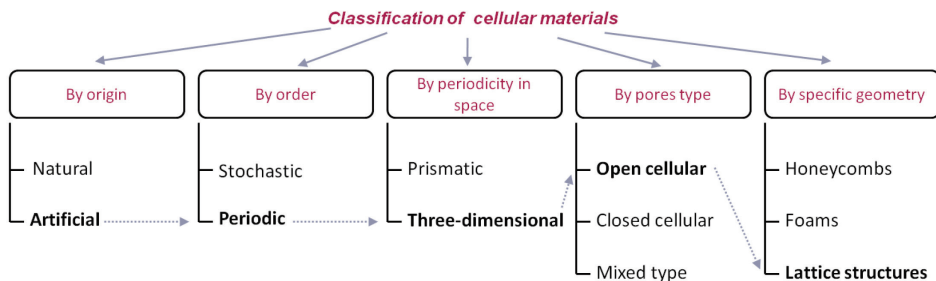
Figure 1.9 Classification of cellular materials.

1.2.2 Cellular lattice structures

Light-weight metal cellular lattice structures are a unique type of materials. Lattice structure is a type of so-called architecture material, which is a combination of a monolithic material and empty space. It is generating a new structure characterized by the equivalent mechanical properties of a new monolithic material [25]. Lattice structures typically exhibit higher structural strength per unit weight than typical foam structures [26]. Periodic metal cellular lattice structures can provide advanced multifunctional, high value performance of engineering and medical products.

From a mechanical engineering viewpoint, the concept of decreasing mass by topology optimization can be easily achieved. Using the material only in the places

where it is needed for a specific application can decrease the weight of the product as well as raw material consumption. Ability of energy absorption by such materials is another point of interest. The geometry of the cellular lattice structures has a significant influence on their properties. A bright example is structured with negative Poisson's ratios [27].

From a medical viewpoint, cellular lattice structures can provide precise control of pores geometry and properties. Precise control of pores geometry and size provides new possibilities in biocompatibility and biomimicry of bone structures.

One of the main mechanical characteristics of lattice structures is compressive strength and modulus, which strongly depends on cell topology and relative density. Dependence of lattice properties on relative density is described by the Gibson-Ashby model [28] for open cellular materials and can be expressed as follows:

$$\frac{E}{E_0} = C_E \times (\frac{\rho}{\rho_0})^2 \qquad (1.1)$$

$$\frac{\sigma}{\sigma_0} = C_\sigma \times \left(\frac{\rho}{\rho_0}\right)^{1.5} \qquad (1.2)$$

where E is compressive modulus, ρ is density and σ is compressive yield strength of an open cellular lattice structure. E_0, ρ_0 and σ_0 are the elastic modulus, density and compressive yield strength of fully dense materials, respectively. C_E and C_σ are the constants and can be calculated based on the experimental results.

Editing the unit cell geometry allows controlling the strength of the cellular lattice structures [29].

1.2.3 Materials for lattice production by SLM

Cellular lattice structures have been widely produced by powder bed additive manufacturing from a wide range of materials. The production of cellular structures by powder feed additive manufacturing systems has not been widely reported. The majority of the studies are attributed to fabrication of lattices from metals. A number of investigations were performed with lattices obtained from stainless steel 316L [30–32], AlSi10Mg [33,34] and Ti6Al4V alloys [35–37].

All materials listed above are widely spread classical alloys for additive manufacturing. However, attempts to obtain lattices from not typical AM alloys have also been reported. Ramirez et al. described the systematic fabrication of various Cu open cellular mesh and foam structures using electron beam melting (EBM) [38].

However, information regarding powder bed fusion of metal-ceramic or ceramic lattice structures is scarce. Only a few successful attempts have been reported with the use of metal-ceramic powder mixtures for SLM of solid parts. TiC/Ti nanocomposites were successfully produced using SLM [39–41]. The maximal value of TiC addition was 22.5 wt.%. The optimal TiC content was defined at 12.5 wt.%, which corresponds to 98.3% density, TiC content above 17.5 wt.% leads to the decreased hardness and reduced wear performance. Ongoing research work in that direction is active. Han et al. investigated the preparation of advanced Al-Al$_2$O$_3$ nanocomposite powder for selective laser melting by ball-milling [42].

Pure ceramics are difficult to process by direct SLM printing due to high heating and cooling rate during the process and the resulting thermal stresses that tend to cause cracks in the material [43]. Another challenge is to achieve full density material. Due to

this, ceramic materials are mostly produced by indirect additive manufacturing [44–46], which requires a second step after 3D-printing of the part.

1.2.4 Thermochemical treatment

The surface hardening or thermochemical treatment can be applied in order to increase the hardness on the surface and keep the initial metal viscosity in the internal volume of the part. As compared to surface hardening, thermochemical treatment has several advantages [47]:

- There is no part shape limitation, which allows treating parts with complex geometry.
- More significant differences exist in the surface properties and internal volume.
- Overheating is not critical.
- The penetration depth is usually controlled by the thermochemical treatment duration.

Carburizing of steels is a process of the surface saturation with carbon. Generally, the process is conducted at the temperatures from 900 to 970 °C. The increase in the temperature leads to a significant increase in the penetration depth (Fig. 1.10). Nitriding is a process of the surface saturation with nitrogen. Usually, the process is carried out at the temperatures 500-600 °C in ammonia atmosphere. The process of nitride layer creation is about 10 times slower than carburizing due to low temperatures of nitriding [48]. The process can be speeded up by the temperature rising. However, it leads to the hardness decreasing (Fig. 1.10).
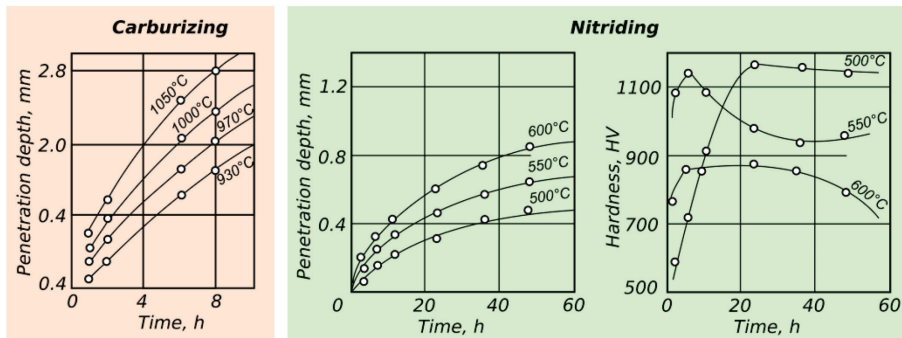
Figure 1.10 Dependence of penetration depth and properties on treatment duration (adapted from [47,49]).

1.3 Current and potential applications of cellular lattice structures

A question about the main benefit of producing complex geometries recently provided by AM arises. To answer this question, it is required to point out the main application areas. Engineering and medical direction can be considered as main application areas of lattices. One of the most important applications of lattice structures in engineering is decreasing the part weight by topology optimization when in medicine they are used in implant production. Current applications of cellular lattice structures are described in detail below.

1.3.1 Topology optimization

Minimizing the material use of the weight of the parts is an important task for many engineering challenges. Figure 1.11 provides a schematic illustration of the route of part's topology optimization by applying the lattice structure and AM. To achieve it for a specific part, it is essential to consider first the functional volume (FV) of the part and functional surfaces (FS) based on an analysis of the functional requirements. FV can be further decomposed into several sub-FVs. These sub-FVs can be divided into two types: FV with solid and FV with lattice structure [50]. The final part will have reduced weight without compromising the required mechanical properties.

The concept of FV and FS is shown in Figure 1.12. The FV and FS represent the geometrical elements designed for certain functional purposes. FS is defined as a surface that fulfils a certain functional requirement. In the figure, skin of the airfoil with a certain thickness provides the lifting force for aircraft. However, the internal volume of the part can provide required mechanical properties without fully dense material [50]. Such approach can be used in the most of engineering tasks, for aerospace, military [27], robotics [13] etc.
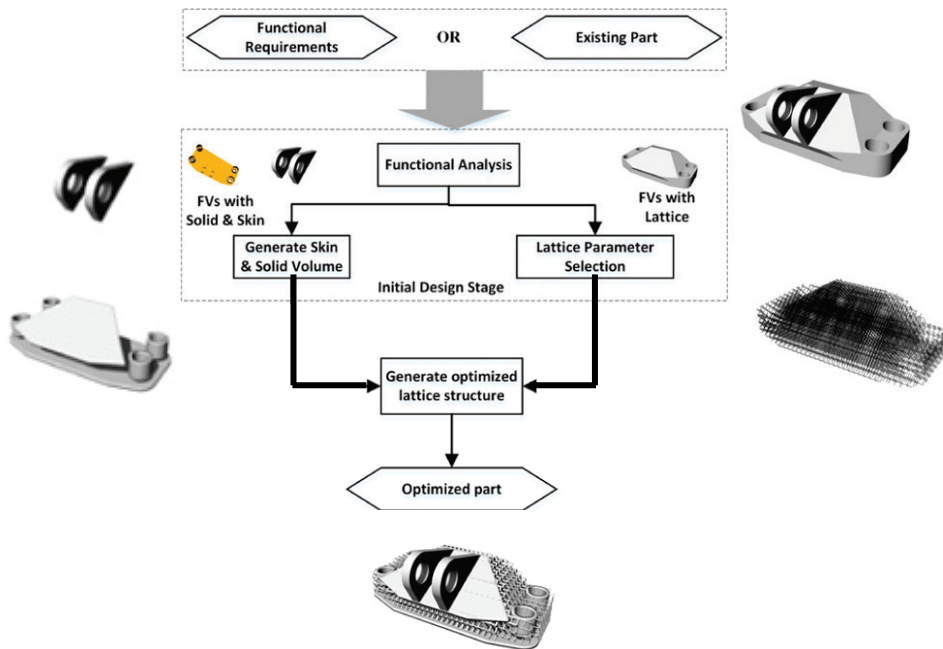

Figure 1.11 Schematic illustration of the part's topology optimization by use of the lattice structure (adapted from [50]).
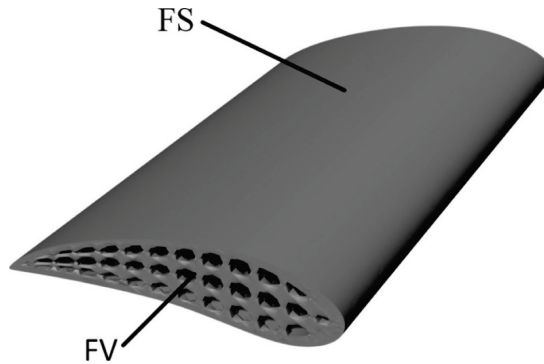
Figure 1.12 The concept of FV and FS of the part [50].

Topology optimization is applied to reduce the weight of the part for specific load conditions. It is beneficial in aerospace and highly required in drone production where weight is an essential issue.

1.3.2 Periodic interpenetrating phase composites (IPCs)

There is an increased scientific and industrial interest related to fiber reinforced [51,52] and 3D composite materials [53,54]. [53,54]. Cellular lattice structures can be used as a reinforcement wireframe to so-called periodic interpenetrating phase composites, materials with co-continuous phases that interpenetrate each other in such a way that if one of the phases is removed, the remaining phase will form a self-supporting cellular structure [55]. The main idea of IPCs is illustrated in Figure 1.13. A number of investigations have been performed on the IPCs in recent years [7,56,57]. Such composites exhibit a number of interesting properties including, perhaps most significantly, a strain to failure that is an order of magnitude greater than that of a monolithic material. It was shown how to achieve specific properties by controlling the volume fraction and the topology of the reinforcement [57].
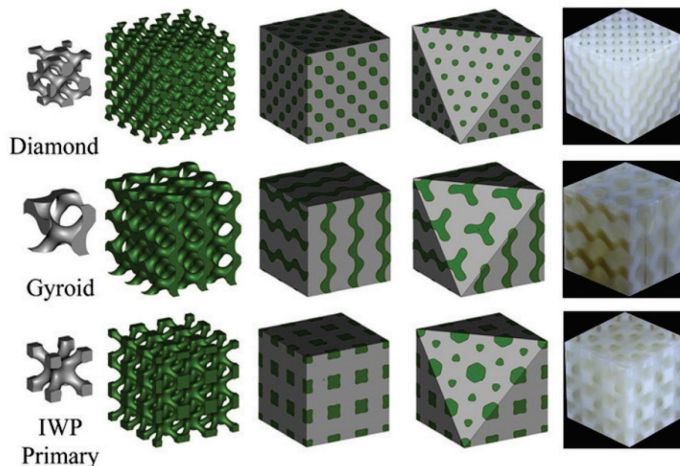

Figure 1.13 Illustration of IPCs with different unit cells (adapted from [55]).

1.3.3 Medical application

For almost fifty years, porous coatings were used to create the surface roughness and porosity in the orthopaedic implants for improving connections with tissues of the surrounding bone and providing bone tissue ingrowth [58–60]. However, contemporary metal additive manufacturing techniques allow producing implants for humans and animals using the lattice structures. Applying lattices allow achieving the modulus values of the implant close to the bone modulus which protect it from destruction with the time. Porous structure allows tissues to grow inside the implant and decreases the biomechanical mismatch between the implant and the surrounding bone. Also, the lattice can be fulfilled by bioactive components to stimulate the tissue ingrowths and regeneration. Such implants are already applied in the medical industry (Fig. 1.14). Wider distribution is also seen in veterinary (Fig. 1.14 b, c) due to simpler regulations and easier process of market entering for the companies.

Deposition of antibiotics on the developed surface of the lattice structure can provide a local drug delivery and make the healing process much faster [61]. Yao et al. reported about the successful fabrication of highly porous scaffolds using Bioglass powder and coating them with polycaprolactone and vancomycin-loaded chitosan to impart a local drug release capability. The coatings increased the compressive strength of initial scaffolds about three times and decreased drug releasing time from 24 to 11 days [62]. In the recent study [63] drug releasing time was increased even to 28 days. This provides uniform local drug delivery during the whole regeneration process.

Cellular lattice structures have disclosed new possibilities for improvements and simplifications in the production of implants and surgery.
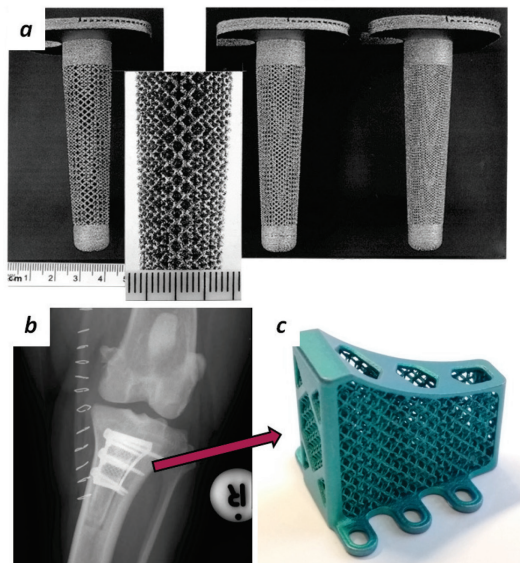
Figure 1.14 Knee implant for a human (a) [64], X-ray image (b) [provided by Rita Leibinger Medical] and general view (c) of TTA implant for a dog produced by Rita Leibinger Medical.

Figure 1.15 illustrates the 3D model and 3D printed implant for the human bone produced at Tallinn University of Technology (TalTech) and implanted in East Tallinn Central Hospital. The implant was customized especially for the patient who lost part of the bone. The coarse lattice structures were employed in the design.
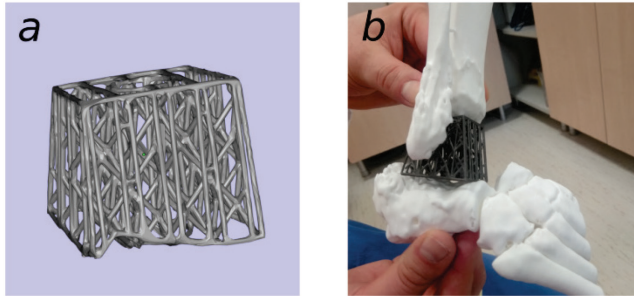
Figure 1.15 3D model (a) and printed implant (b) for the human bone produced in TalTech.

1.3.4 Potential application of cellular lattice structures in thermoacoustics

Thermal-to-acoustic power conversion has been effectively reproduced in Rijke and Sondhauss tubes since the 1850s [65]. Lord Reyleigh described this effect as the result of providing heat to acoustic waves at the moment of greatest condensation and detracting heat at the moment of greatest rarefaction [66]. Rott was the first to publish the governing equations in 1969 [67]. However, the largest contributions to the study and development of thermoacoustic engines (TAEs) came later, with the works of Swift and co-workers from 1983 [68]. The Swift's textbook published in 2001 is still considered as the main reference in the field [69].

A TAE is a device where low grade thermal energy is partially converted into acoustic waves with high sound pressure levels. The acoustic waves generated in TAEs can be harvested in many different ways, for instance, into purely mechanical energy, into electric energy, or used as sound excitation in thermoacoustically driven thermoacoustic refrigerators.

The core of a TAE is the porous material placed within the resonator, along which a temperature gradient is established by means of a hot and a cold heat exchanger. Thermal-to-acoustic power conversion occurs because of the temperature gradient within the stack. A schematic TAE setup is shown in Figure 1.16.

In 1993, a more effective pin stack array for TAE was described [10]. However, the manufacturing process of such stacks is relatively difficult. Due to this, the majority of used stacks are various configurations of plate stacks [70]. Lattice structures combine the properties of the pin stack arrays with precisely controlled geometry, which allows tailoring thermoacoustic performance.
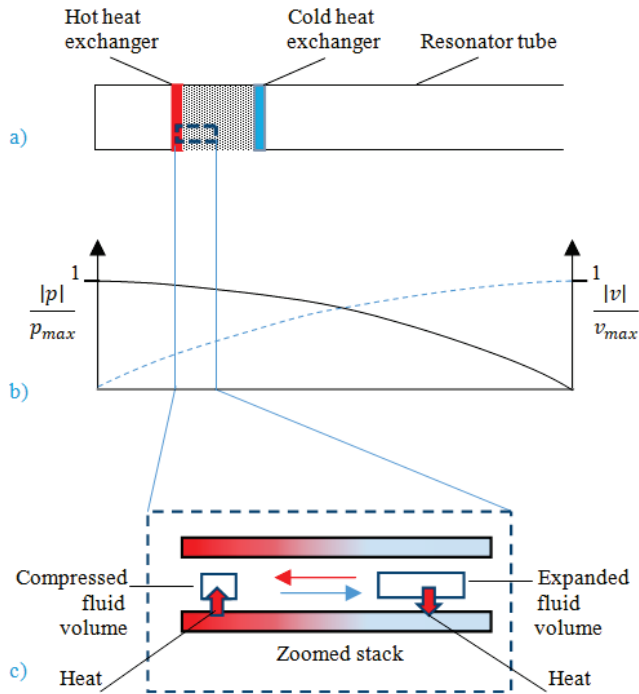
Figure 1.16 Standing-wave thermoacoustic heat engine, schematic setup (a); pressure and particle velocity field (b); heat exchange of fluid particle within the stack (c) [IV].

1.4 Objectives of the work

The motivation of the present study is illustrated in Figure 1.17. To disclose new application areas of cellular lattice structures such as tribology and thermoacoustics, it is required to solve related challenges mentioned above. In order to increase the thermoacoustic performance and wear resistance of cellular lattice structures, the two-step approach was proposed in order to produce metal-ceramic composite structures. Cellular lattice structures fabricated by SLM were nitrided and carburized.

The overall objective of this research is to develop and optimize production of metal and metal-ceramic cellular lattice structures and disclose new areas of their application.
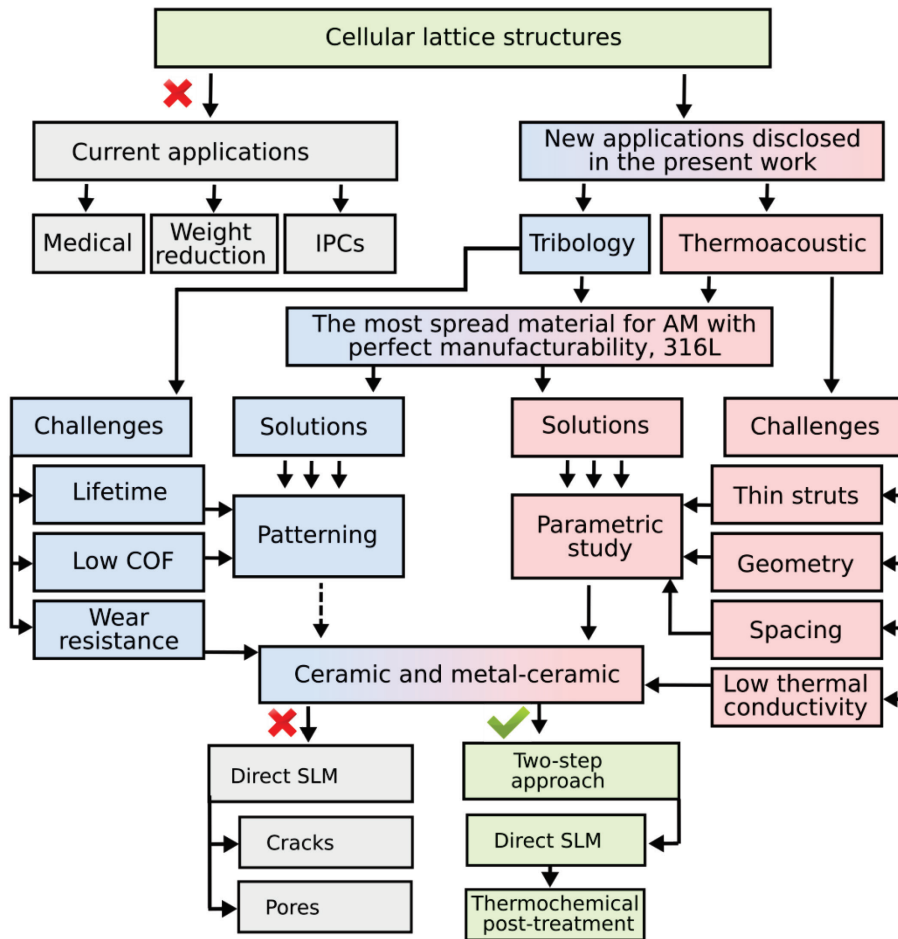
Figure 1.17 The motivation scheme.

The scientific goals of the present study are:

- To perform a parametric study to understand the relationship between the process parameters and the properties of the cellular lattice structures obtained by pulsed laser scanning strategy for powder bed and powder feed AM processes; pulsed laser allows obtaining the thinnest lattice struts;

- To reveal some aspects regarding formation of microstructural features and development of mechanical properties when obtaining metal-ceramic cellular lattice structures by direct and indirect AM;

- To validate the tribological performance of the cellular lattice structures; the ability to tune properties like self-cleaning effect, wear and friction coefficient according to the designed surface structures;

- To validate the effect of mesostructural features and metals and metal/ceramic materials on the thermoacoustical performance of the cellular lattice structures.

The main technological goals of the present study are:

- To develop the process parameters for producing cellular lattice structures with a feature size in order of 100-200 μm using DED. To determine the possibilities and limitations of the DED process for producing such mesostructures;

- To increase the mechanical properties of cellular lattice structures by the fabrication of novel metal-ceramic lattices;

- To open up new application areas for metal and metal-ceramic cellular lattice structures.

The advantage of the lattice structures is the properties of highly porous materials combined with completely controlled geometry which allows tailoring the final properties. The aim is to provide a suitable technological route for metal and metal-ceramic cellular lattice structures, production and make conclusions about their performance in the potential application areas.

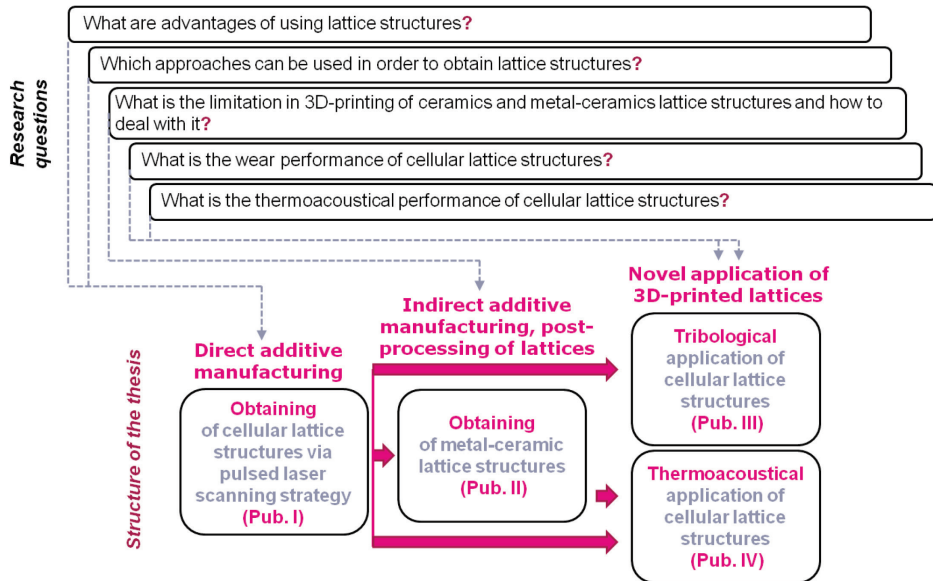Figure 1.18 introduces the overall structure of the thesis.

Figure 1.18 Schematic illustration the thesis content and structure.

2 EXPERIMENTAL

2.1 Materials

In order to investigate the relationship between the process parameters and the strut diameters of cellular lattice structures produced via SLM the most common for additive manufacturing atomized AISI 316L powder with particle size 10-45 µm delivered by Shijiazhuang Daye Metal Powder Factory was used. The chemical composition of AISI 316L is shown in Table 2.1. Figure 2.1 shows the SEM images of a general view of AISI 316L powder and polished cross-section of the powder. Cross-section of the powder was made to investigate the presence of internal porosity.

Table 2.1 Chemical composition of AISI 316L.

Alloying element	Fe	C	Cr	Ni	Mo	Mn	Si	P	S
wt%	Rest	<0.03	16-18.5	10-14	2-3	<2	<1	<0.045	<0.03
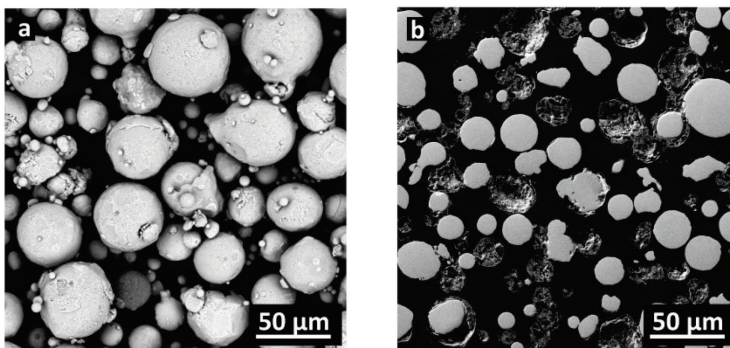
Figure 2.1 SEM images of AISI 316L powder (a) and polished 316L powder (b).

2.2 Process and parameters

SLM and DED were chosen to study a possible implementation of pulsed laser scanning strategy which allows producing the thinnest features of the lattice. EBM process was not considered for such applications in the present study. Process parameters define the amount of energy provided by the source to the feedstock. The process parameters used in the present study are described in detail below.

2.2.1 Selective laser melting

A *Realizer SLM50* selective laser melting machine produced by Realizer GmbH was used for producing cellular lattice structures. Schematic illustration of the building chamber is shown in Figure 2.2. The machine is equipped with a YAG fiber laser to enable reaching the maximal power of 120 W. Argon or nitrogen was used as a protective atmosphere inside the building chamber with the controlled oxygen level during the process, which was kept below 0.2%.
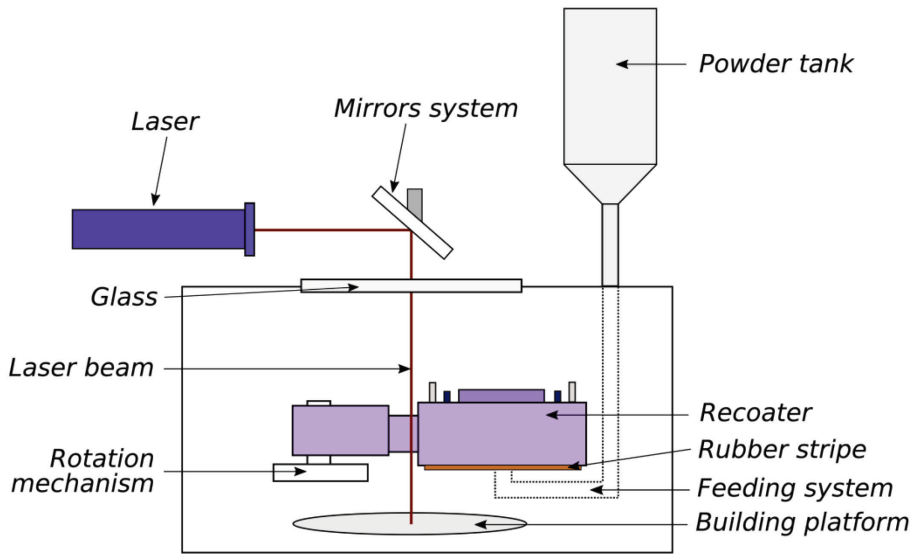
Figure 2.2 Scheme of the SLM machine chamber.

Cellular lattice structures can be obtained using pulsed laser scanning strategy. It means that one slice of the lattice beam model contains a set of discrete points which define the coordinates of laser exposure (Fig. 2.3). The thickness of a strut in this case is related to the melt pool size and is defined by a combination of laser power and exposure time in each point.

The thickness of one layer was 25 µm, laser current was varied from 2500 mA (60 W) to 5000 mA (120W), the exposure time was varied from 250 to 1100 ms. Nitrogen was used as a protective atmosphere during the process with an oxygen level of less than 0.2%.
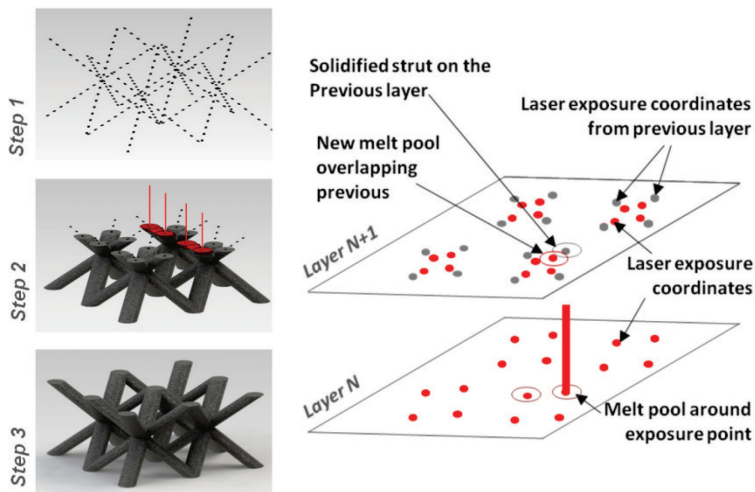
Figure 2.3 Schematic explanation of the pulsed laser scanning strategy for obtaining cellular lattice structures.

2.2.2 Laser metal deposition

Directed energy deposition was performed using a Hermle C20U five axis machine equipped by a Siemens Sinumerik controller (Fig. 2.4). Modular powder nozzle system COAX14 was used. Fiber laser with a maximum power of 200 W is employed in the system. Argon is used as a shielding gas and gas for transporting the powder.

Figure 2.4 Scheme of the DED process.

The laser metal deposition process is carried out by creating a melt pool on the surface of the substrate. Powder flow is conically focused. The powder cone vertex is coaxially coincident with a laser beam.

Process parameters were determined empirically. Straight pillars were produced in order to determine the process parameters that provide a stable deposition process. The aim was to obtain as thin pillars as possible in order to produce thin cellular lattice structures with geometrical characteristics comparable with the lattices produced by SLM. In order to achieve the aim, it is required to determine a specific set of process parameters, including but not limited to, low laser power. In general, laser power determines the diameter of the weld spot. To keep the diameter as small as possible, the laser powers of 20, 30 and 40 W were employed to produce straight pillars. The second important parameter that influences the weld spot diameter and height is exposure time (ET) and break duration. The break time between subsequent laser exposures is needed to avoid accumulation of the heat and uncontrolled melting. The ET was varied from 0.001 to 0.03 s. The break time was equal to the exposure time.

2.3 Lattice generation

The initial step in the lattice production is its modeling in CAD or generation using other specific software. The lattice generation routes used in the present study are described below.

2.3.1 Lattice generation for SLM

Lattices were created using RDesigner software developed by Realizer GmbH. General route of the lattice generation in RDesigner is presented in Figure 2.5. First of all, 3D-model in STL file format has to be imported to the software. Next, the STL 3D-model has to be sliced and lattice (with pre-defined unit cell geometry) generated. The generated lattice structure consists of repeating unit cells, each of them formed by connecting vectors with zero thickness. Sliced lattice at each layer is represented as a set of single, discrete points which determine the location of laser exposures.
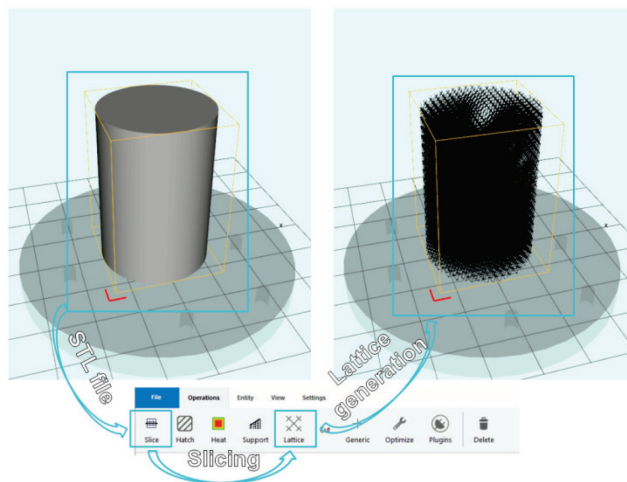

Figure 2.5 Lattice generation route in RDesigner software.

2.3.2 Lattice generation for DED

Lattice geometry was defined by a programmatic method using a custom G-code algorithm. The diamond shaped unit cell was described by a set of simple mathematical equations. The algorithm calculates the geometry layer by layer. Four points on the first layer are located at the nodes of the diamond-shaped cell. The coordinates of laser exposure are defined by these points on each next layer that four points moving towards each other. The points meet at the centre and then move from one another until the end of the unit cell. Schematically, the idea is shown in Figure 2.6. Simple geometric dependencies were employed for the calculation of locations of points on each layer.

The origin in the top view projection is located at the centre of the unit cell. X and Y axes are assigned to the strut projections. According to the building program, laser is treating four equidistant points around Z axis. These four points belong to the initial single unit cell. Total mesh array generation is provided by the initial unit cell tessellation in three dimensions. To achieve this, a certain number of layers that contain two-dimensional point patterns should be generated. After exposure in all points on one layer, the process head moves up for the distance equal to a single layer

thickness (LT). Point coordinates on each next layer are calculated with counting of horizontal displacement (*dX*). It depends on the inclination angle (α) and is calculated as follows:

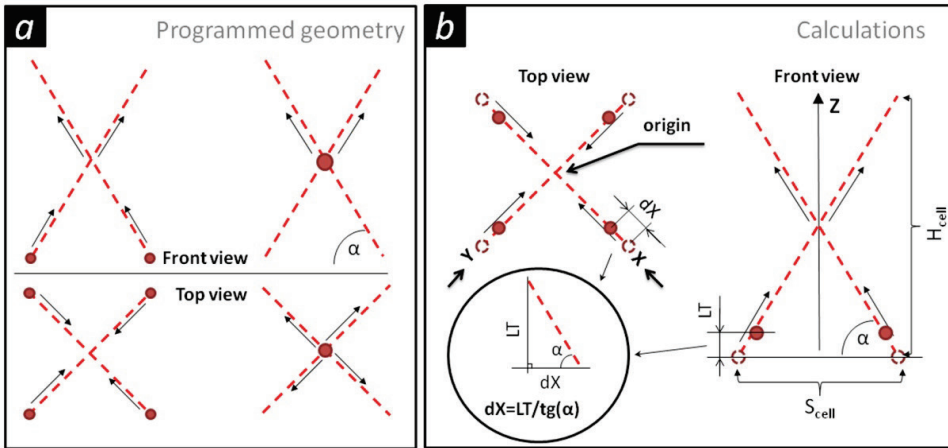$$dX = \frac{LT}{\tan(\alpha)} \tag{2.1}$$

Figure 2.6 Lattice generation route for LMD using a direct G-code algorithm, schematic geometry (a) and illustrations of the calculations (b).

Main input parameters for the program are the size of the unit cell (Scell), strut inclination angle (α) and layer thickness (LT). Other important lattice parameters are calculated based on the input data. These are total unit cell height (Hcell), horizontal displacement at each layer (dX) and the number of layers (N).

The total unit cell height Hcell is calculated based on the input parameters, unit cell size and inclination angle, as shown in equation 2.2:

$$H_{cell} = S_{cell} \times tan(\alpha) \tag{2.2}$$

2.4 Post-processing

Post-processing investigation can be divided into two main categories: preliminary studies and post-processing of cellular lattice structures. Nitriding and carburizing were employed as post-processing procedures. Preliminary tests started by investigating the penetration depth during nitriding and carburizing of 3D-printed specimens. For these purposes, samples with cylinders having diameters 0.3 mm, 0.5 mm, 1.5 mm, and 2.5 mm were produced. The 3D model of the sample is presented in Figure 2.7.
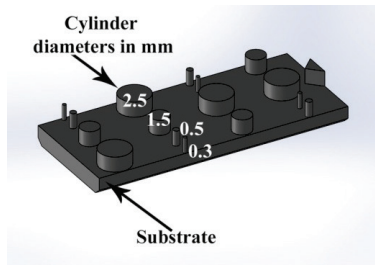
Figure 2.7 3D model of the sample used for preliminary experiments

2.4.1 Nitriding of lattices

Nitriding of the specimens was performed with and without overpressure. In order to apply overpressure, a HIP furnace was employed. The data from the literature confirm a possibility of surface nitriding in N2 atmosphere [71,72]. Hot isostatic pressing was carried out at 1150 °C at 100 MPa under nitrogen. Nitriding without overpressure was performed under atmospheric pressure in nitrogen atmosphere using Dr. Webb Red Devil furnace. All nitriding conditions are shown in Table 2.2.

Table 2.2 Nitriding conditions.

Nomination	Environment	Temperature, °C	Holding time, min	Cooling conditions
N1	N_2, 100 MPa	1150	60	Furnace cooling
N2	N_2, 0.1 MPa	1150	60	Furnace cooling

2.4.2 Carburizing of lattices

Carburizing in the present study was performed by using a custom made thermal "Hot-wall" chemical vapor deposition device. The schematic illustration of the device is presented in Figure 2.8.
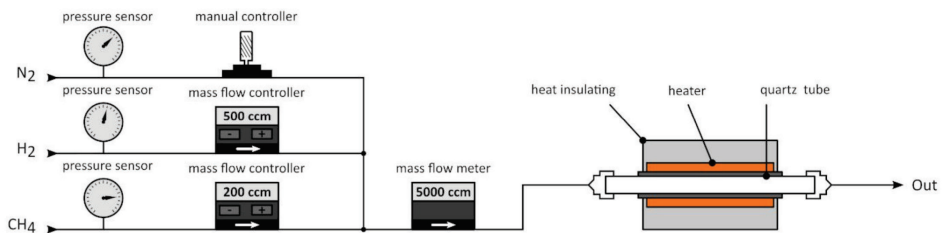

Figure 2.8 Schematic illustration of the CVD device [73]*.*

Carburizing was performed in CH_4 flow at 1000 °C. The holding time was 20 and 60 minutes. CH_4 flow was 250 ccm and 200 ccm for 316L and Ti respectively. For some specimens, heat treatment in vacuum at the 1150 °C for 1 hour and cooling down with the furnace was applied. Table 2.3 summarizes carburizing parameters used in the present study.

Table 2.3 Carburizing conditions.

Nomination	Material	Holding time, min	Cooling conditions	Post treatment
C1	316L	20	in air	N/A
C2	316L	20	in air	1150°C for 1 h in vacuum
C3	316L	60	Furnace cooling	N/A

2.5 Characterization

2.5.1 Description of properties

A microstructural characterization was performed by an optical microscope (OM), a tabletop scanning electron microscope (SEM) Hitachi TM1000 with BSE detector and high resolution electron microscope Zeiss Evo MA15, equipped with an energy dispersive X-ray analyzer (EDS) with a Dual BSE detector and operating at an accelerating voltage of 20 kV.

Compressive strength of lattice structures was measured at the loading rate 1 mm/min, using an Instron 8516 servo-hydraulic testing system. The XRD analysis was carried out on diffractometer "Ultima IV" (Rigaku, Japan) using monochromatic Cu-Kα radiation (the wavelength 1.5406 Å) with step 0.02° along the 2θ and time measuring of 4s/step. Vickers microhardness was measured by using a Buehler Micromet 2001 microhardness tester. Diamond pyramid indenter with an angle at the top 136° was employed.

2.5.2 Wear sliding test

Unidirectional sliding tests were performed using a CETR (Bruker) UMT-2 multi-functional tribo-device in pin-on-disc configuration in dry sliding conditions. The load varied from 5 to 103 N in the beginning and the end of the test respectively. Continuous increase by 9.8 N in a minute in a load was applied. Coefficient of friction (COF) was continuously recorded. The test duration was adjusted to 10 min in order to avoid the wear of the whole structure. This method allows fast estimation of COFs and possible specific changes in the frictional behavior in a wide range of loads during a single experiment. Sliding velocity was 5×10^{-3} m/s. The diameter of the sliding track was 32 mm. The disc was made from AISI 316 stainless steel and polished to Ra 0.2 mm. Before the test, the disc was cleaned by acetone. The surfaces were examined before and after the experiments by the SEM.

2.5.3 Thermoacoustic properties

The experimental setup of a thermo-acoustic engine (TAE) used in the present study is shown in Figure 2.9. It consists of a resonator tube, two heat exchangers and a cellular lattice structure as a stack. One side of the stack is heated by a focused energy source. The stack acts as a thermal reservoir, providing irreversible heat exchanges between the solid, immobile surface and the fluid. Heat is provided to the air at the cross-section of the stack, which is closer to the closed end, and taken away at the other one. In this way, the first resonant mode (characterized by pressure antinode at the closed-end and pressure node at the open-end) is excited. In fact, the Rayleigh's principle is satisfied, since the heat is given (respectively taken) where the pressure is higher (respectively lower).
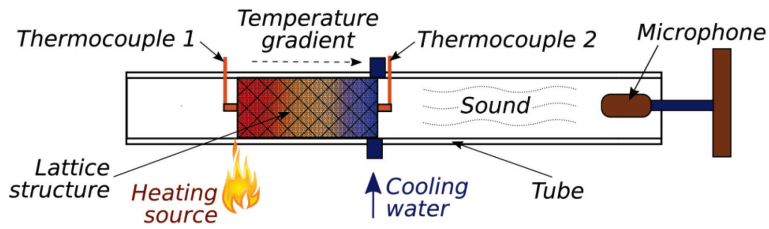
Figure 2.9 TAE experimental setup.

As a result, when a certain value of the temperature gradient is achieved (typically in the range of 150-250 °C), generation of strong acoustic standing waves is started within the resonator. In order to measure the temperature gradient and the sound level, two thermocouples and three microphones are employed in the experimental setup.

The geometries of the stacks tested in the present study are characterized in Table 2.4. The parameter D represents the thickness of the plates or the diameter of the pins (diameter of the strut in the case of lattice structure), H is the distance between the plates or pins, ρ is the porosity and HD is the hydraulic radius previously defined.

Table 2.4 Main geometrical parameters of the stacks.

| Sample name	Stack type	D [mm]	H [mm]	ρ, %	HD [mm]
Stack 1	Parallel plates	0.18	0.88	76.6	0,329
Stack 2	Oblique pins	0.18	0.89	87.3	0.370
Stack 3	Parallel plates	0.18	0,73	78.7	0.286
Stack 4	Oblique pin	0.21	0.63	86.9	0.343
Stack 5	Parallel plates	0.18	1.98	91.2	0.859
Stack 6	Lattice	0.18	1.5×1.5×2*	96.4	0.864
* A diamond shaped lattice structure was used, the size of the unit cell is provided					

3 RESULTS

3.1 Fabrication of cellular lattice structures from metals

One of the approaches of obtaining cellular lattice structures with a small feature size is pulsed laser scanning strategy. However, to understand the relationship between the process parameters and the properties of the cellular lattice structures obtained by pulsed laser scanning strategy, a parametric study is required. In the present study, cellular lattice structures were fabricated by the powder bed and powder feed AM techniques, selective laser melting, and directed energy deposition respectively.

3.1.1 Selective laser melting
Figure 3.1 shows a general view of the lattice structures obtained by pulsed laser scanning strategy via selective laser melting.
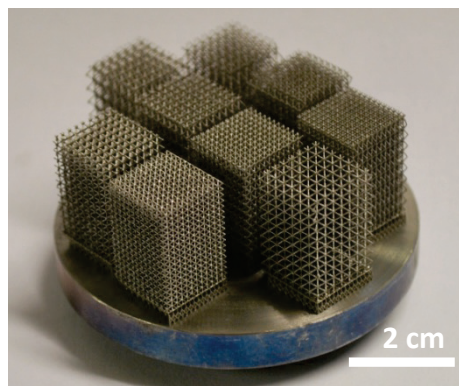
Figure 3.1 Lattice structures obtained by SLM.

The diameter of the single strut was measured under SEM. In general, the strut diameter of the lattices obtained by pulsed laser scanning strategy via SLM is defined by the combination of laser power, exposure time and spot size. These parameters also influence the morphology of the strut surface. In order to study the influence of the SLM process parameters on the resulted strut diameter and surface morphology, a broad range of parameters were tested: the laser power at 60, 70, 75, 100 and 120 W and exposure time at 0.25, 0.30, 0.35, 0.40, 0.60, 0.80, 1.10, 1.40 and 2.00 ms. The spot size was constant and approximately equal to 40 μm. Figure 3.2 illustrates the effect of laser power and exposure time on the strut diameter and surface of the strut. Significant increase of the strut diameter with laser power (LP) is visible. The lattices obtained at 60 W are characterized by the thinnest struts covered by a number of bonded particles. Two types of bonded particles were detected: from the feedstock powder and formed during the SLM process. Increasing of LP reduces the amount of bonded particles. More details about the SLM parameter study and strut diameters can be found in the Publication I.
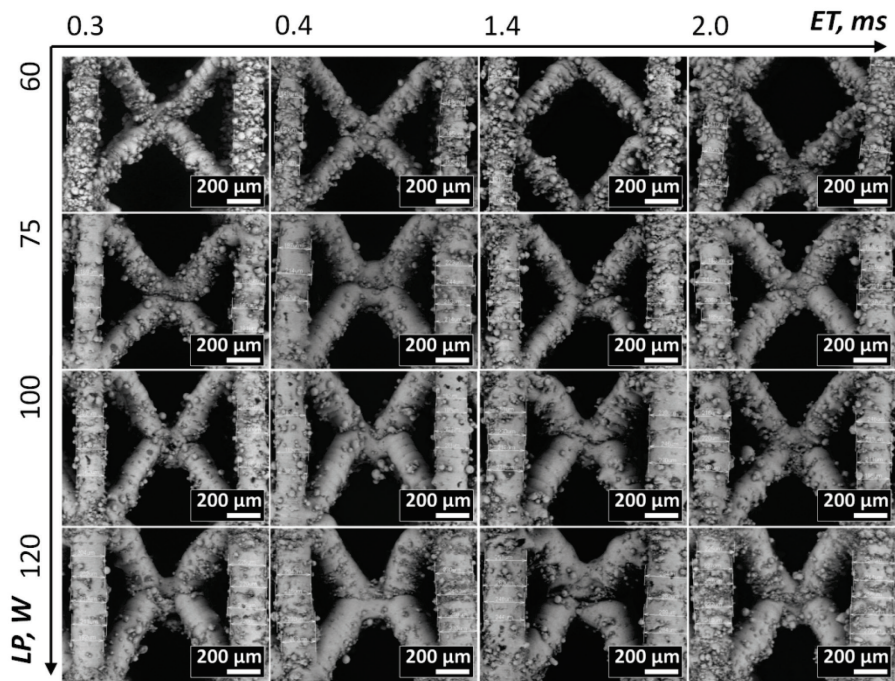
Figure 3.2 SEM images of lattice struts obtained via SLM using various parameter combinations.

3.1.2 Directed energy deposition

General view and SEM images of cellular lattice structures obtained by pulsed laser scanning strategy via directed energy deposition are shown in Figure 3.3. Figure 3.3 a and b visually illustrate the difference between the lattices obtained using different parameters and unit cell sizes. Figure 3.3 c and d show SEM images of cellular lattice structures produced with the same parameters but with different unit cell sizes, 0.7 and 0.5 mm respectively. Bonded particles are present on the struts surfaces. The origin of the particles is feedstock powder. All bonded particles stick to the molten material or were partially melted. The formation of secondary bonded particles was not observed.

In the case of DED process, spot size, LP, ET and powder flow rate influence the layer thickness, which should be used in the process as well as the final strut diameter. To obtain thin lattice structures comparable with those produced by SLM, the effect of laser power at 20, 30 and 40 W and exposure time at 30, 18, 1.8 and 1 ms was investigated. The laser spot size was kept constant at 30 μm.

Table 3.1 summarizes layer thicknesses and strut diameters for various LP and ET combinations. Decreasing of LP and ET leads to decreasing of strut diameter. In general, for each tested ET, the layer thickness is increasing with LP. However, at the highest tested ET, 30 ms, this dependence is the opposite.
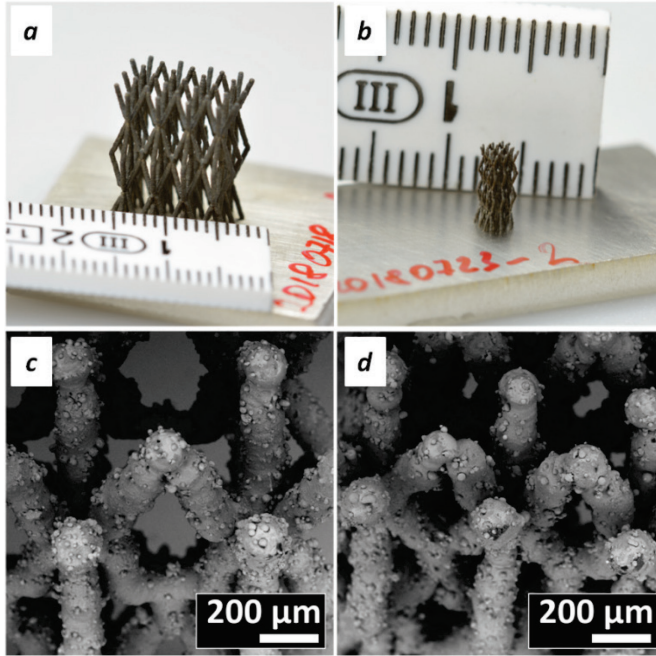
Figure 3.3 General view and SEM images of lattice structures obtained via DED: LP 40 W, cell 3 mm (a); LP 20 W, cell 0.7 mm (b, c); LP 20 W, cell 0.5 mm (d).

Table 3.1 Estimated layer thickness.

Power, W		Exposure time, ms			
		30	18	1.8	1
20	LT, mm	0.117	0.069	0.031	0.026
	D, mm	0.270	0.230	0.160	0.160
30	LT, mm	0.104	0.067	0.033	0.031
	D, mm	0.440	0.410	0.280	0.280
40	LT, mm	0.100	0.073	0.035	0.034
	D, mm	0.530	0.490	0.370	0.370

The smallest inclination angle for the stable process was determined at 60 degrees. Successful printing of lattice structures with lower inclination angle, 53 degrees, was also achieved. However, the repeatability of the process requires additional adjustment of processing parameters.

Figure 3.4 shows optical microscope images of cross-sections of the struts after polishing and etching. The images give a complemented overview on the porosity of the specimens obtained using different process parameters. The SEM images of the cross-sections of the struts obtained via SLM are shown in Figure 3.4 (e). The amount of pores and their sizes varied in the different specimens. Only a few pores were observed on the cross-section of the sample with the largest strut diameter (LP = 40 W, ET = 30 ms). Decreasing the exposure time leads to an increase in the number of pores (Fig. 3.4 b,c).

Minor porosity was observed in the specimen with the smallest strut diameter obtained using LP 20 W and ET 1 ms.
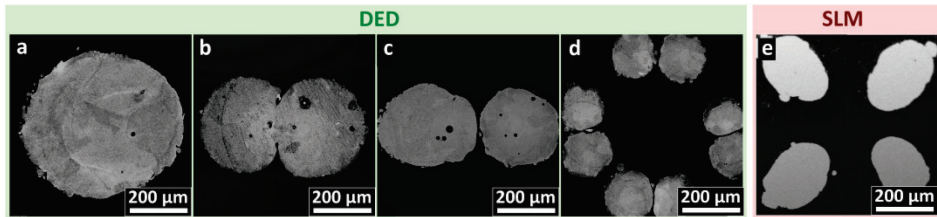

Figure 3.4 Optical micrograph of etched cross sections of the lattices obtained via DED using the next parameter sets: LP 40 W and ET 30 ms (a); LP 40 W and ET 1.8 ms (b); LP 30 W and ET 1 ms (c); LP 20 W and ET 1 ms (d), and SEM image of lattice obtained via SLM cross section (e).

3.2 Nitriding and carburizing of cellular lattice structures

In order to produce metal-ceramic lattice structures, a two-step approach is proposed, where nitriding and carburizing are applied to 3D printed lattice structures as post- processing procedures. Metal-ceramic lattice structures are expected to be more beneficial in tribological and thermoacoustic applications.

Post-processing parameters were preliminarily tested using samples with diameters 0.3, 0.5, 1.5 and 2.5 mm (Fig. 2.8). The main aim was to evaluate the thickness of the penetration zone and to estimate mechanical properties preliminarily. The diameter of the smallest cylindrical specimen is very close to the lattice strut diameter.

The difference between untreated 316 L specimens and nitrided samples under N1 and N2 conditions can be visually observed in Figure 3.5.
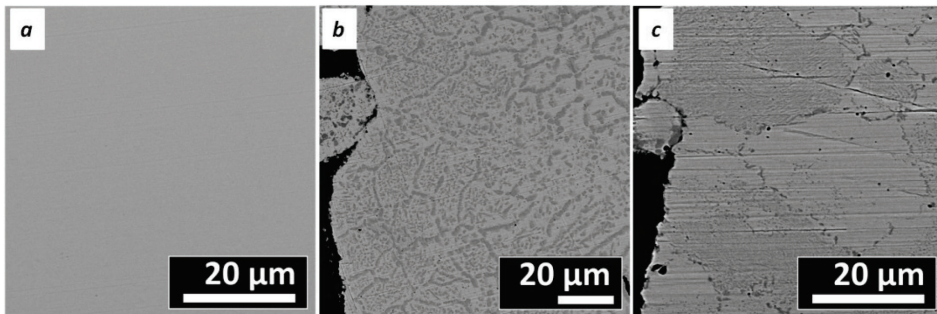

Figure 3.5 SEM images of reference 316L (a) microstructure and nitrided specimens with diameter 0.5 mm under N1 (b) and N2 (c) conditions.

The microstructures of the cross-sections of cylindrical samples nitrided with applied overpressure (N1 conditions) and at atmospheric pressure (N2 conditions) are shown in Figure 3.6. Applying overpressure causes more obvious microstructural changes, namely appearing in the second phase. The structure of 0.3 mm cylindrical sample consists of sets of submicron round shaped inclusions divided into sections by elongated inclusions of the same phase precipitated along grain boundaries. The distribution of the second phase in the microstructure is uniform across the whole cross section for the specimens with diameters 0.3 and 0.5 mm. In the case of 1.5 and

2.5 mm diameter, inclusions were observed in the narrow zone near the surface. The thickness of the zone is slightly above 90 µm.

The structure of 0.3 and 0.5 mm cylinders processed by N1 conditions consists of sets of spot-like inclusions divided into sections by elongated inclusions, precipitated along grain boundaries. It has been found that for N1 conditions elongated inclusions prevail in the cylinders with a larger diameter.
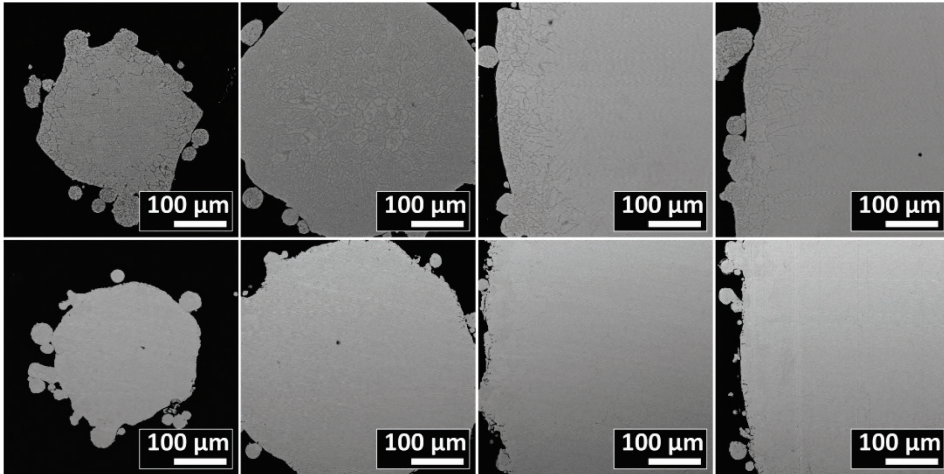
Figure 3.6 Cross sections of specimens with various diameters nitrided with N1 and N2 conditions.

Nitriding without overpressure (N2 conditions) caused almost no visible changes in the microstructure. The appearance of most of the specimens cross-sections is similar to the microstructure of reference 316 L sample (Fig. 3.6 a). The changes in the microstructure of N2 specimens were detected under higher magnification in the area located close to the specimen surface.

Carburizing was performed for 20 min with or without following annealing (C1 and C2 conditions respectively). C3 conditions are characterized by an increased carburizing time – 60 minutes. It was found that after the carburizing process in CH_4 flow for 20 min at 1000 °C (C1 conditions), a significant amount of deposited carbon is located on the surface of the samples (Fig. 3.7). Additional vacuum annealing (C2 conditions) was performed in order to activate the diffusion process of the deposited carbon towards the sample volume.
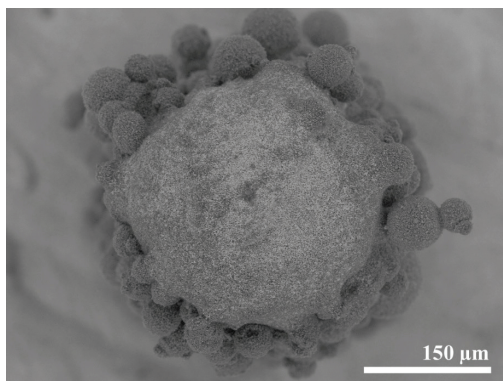
Figure 3.7 Specimen with 0.3 mm diameter covered with carbon after 20 min of carburizing in CH$_4$ flow (C1 conditions).

Table 3.2 shows the microstructural differences of the specimens with various diameters for C1, C2 and C3 carburizing conditions. Increasing the diameter of the specimen yields a decrease of the penetration depth. The distribution of the inclusions is uniform throughout the cross-section under C2 and C3 conditions and specimens diameters 0.3 and 0.5 mm. For the rest of the specimens, a gradient of distribution was present between the external surface and the central area. In general, the penetration depth in C3 condition was slightly higher as compared to C2 conditions.

Microhardness values for post-processed samples with different cross-section diameters are presented in Figure 3.8. The hardness measurements were taken in the center of the cross-section of cylindrical specimens. The microhardness of post-processed samples tends to decrease with an increase in the diameter. In general, for all post processing conditions, hardness for samples with 0.3 mm in diameter is about twice higher than for samples with 2.5 mm in diameter. For nitrided samples with diameters 1.5 and 2.5 mm, the Vickers microhardness values were compatible with the reference value taken from untreated 316L.

Table 3.2 Penetration depth in samples with various diameters.

Specimen diameter, mm	Thickness of reaction zone		
	C1	C2	C3
0.3	100-120 µm	full	full
0.5	50-70 µm	full	full
1.5	~30-50* µm	up to 100 µm	150-160 µm
2.5	~40-60* µm	30-50 µm	100-120 µm

*Rare inclusions precipitated along grain boundaries

Based on preliminary tests, post-treatment conditions N1 and C2 were chosen to be applied to the lattice structures in order to obtain uniform nitrides and carbides distribution. A set of lattice structures obtained at LP 100 W and ET of 1100 µs was used for nitriding (N1 conditions) and carburizing (C2 conditions). Such lattices have the closest strut dimensions to preliminarily tested cylinders with diameters of 0.3 mm.

3.3 Properties of metal and metal-ceramic lattice structures

3.3.1 Mechanical properties

Nitrided and carburized lattice structures exhibit higher hardness and strength characteristics. The structure and properties of produced metal-ceramic lattice structures are described in detail in Publication II.
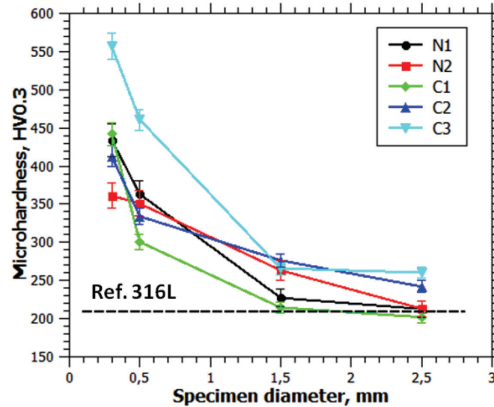

Figure 3.8 Microhardness values for specimens with different diameters used for preliminary tests.

Figure 3.9 shows the strength characteristics of untreated lattices. Compressive yield strength of metal lattice structures measured experimentally and calculated according to the Gibson-Ashby model depends on the relative density. Compressive yield strength tends to grow with the relative density. As seen from the graph, in general, the result obtained correlates with the Gibson-Ashby model [28]. The calculated coefficient of correlation R = 0.9865.
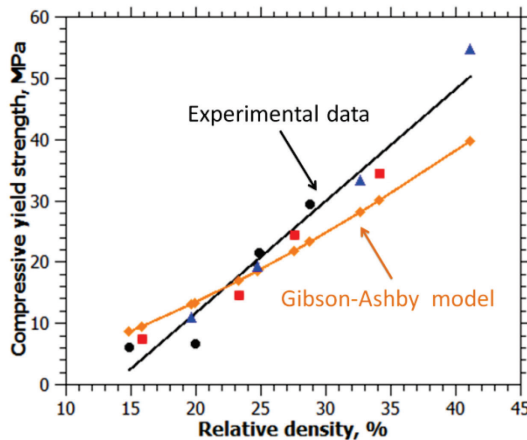

Figure 3.9 Measured and theoretically calculated compressive yield strength values of untreated lattices.

The compressive strength data for untreated, nitrided and carburized lattices are collected in Table 3.3. All nitrided lattices collapsed without plastic deformation, having 2-3% of shortening before collapsing. In the case of carburized lattices, some plastic deformation was observed. Deformation of carburized lattices before critical failure was from about 4.5 to 8% for lattices with the lowest and with the highest relative density respectively. Compressive yield strength of carburized lattices increased on average 10 MPa, in the whole range of lattice relative densities. With an increase of lattice relative density, the difference between the yield strength and the fracture stress is increasing. Elastic modulus increases with the density (Table 3.3). Post-processing tends to increase the elastic modulus.

Table 3.3 Average results of the compressive test of lattice structures [II].

Lattice density	Compressive Yield Strength, [MPa]		Ultimate fracture stress, [MPa]		Elastic Modulus, [GPa]		
	Not treated	Carburized	Nitrided	Carburized	Not treated	Nitri-ded	Carburi-zed
19.6 %	10.95	18.5	27	21	0.42	0.96	0.59
24.7 %	19.2	30	31.2	33	1.08	1.25	1.10
32.6 %	33.35	42	44.6	69	1.51	2.2	1.95
41.1 %	54.8	66.7	60.7	99,3	1.76	2.33	2.31

3.3.2 Frictional behavior of cellular lattice structures in dry sliding conditions

Publication III is dedicated to the friction studies of various surface patterns produced by powder bed fusion from stainless steel. One type of surface patterns was a single layer of a lattice structure with an octet-truss unit cell. The 3D models of the specimens and SEM images before and after wear testing are presented in Figure 3.10. The 3D model defined the unit cell size equal to 1 mm while the strut diameter was 3D modeled to be 0.15, 0.20 and 0.30 mm. Bonded particles covered the surface of the lattice struts. In the case of the lattice with 0.15 mm strut diameter, the origin of the particles is feedstock powder, for lattices with 0.2 and 0.3 mm diameter, the majority of the particles appeared due to so-called balling phenomenon.

Figure 3.11 summarizes the effect of load on the coefficient of the friction of cellular lattice structures and a flat reference surface. The cellular lattice structures are providing a low and stable friction coefficient in the whole range of loads. The COF is staying low even at the highest load of 103 N (COF 0.2), which is five times lower than that observed in the reference sample with flat surface (Fig. 3.11 a).
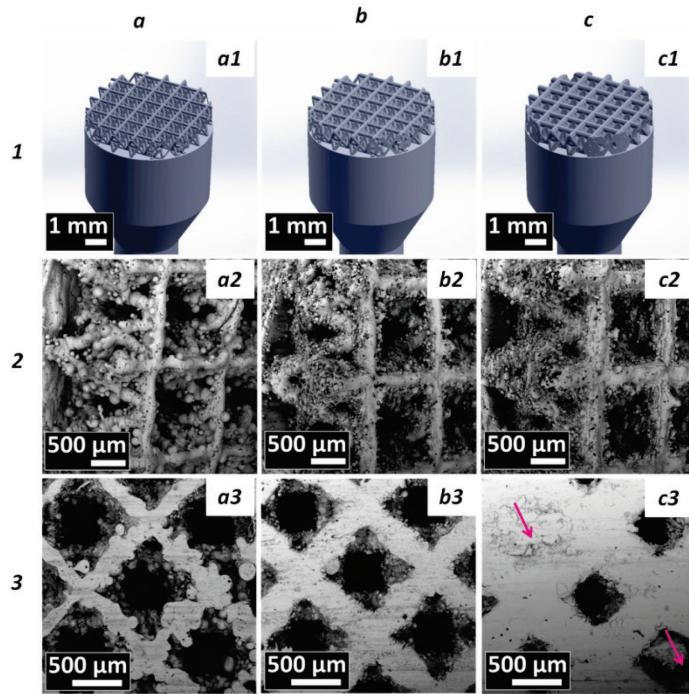
Figure 3.10 3D models (1) of prepared specimens and SEM images of cellular lattice structures with the strut diameter 0.15 mm (a), 0.20 mm (b) and 0.30 mm (c) as a surface pattern, before (2) and after (3) wear.
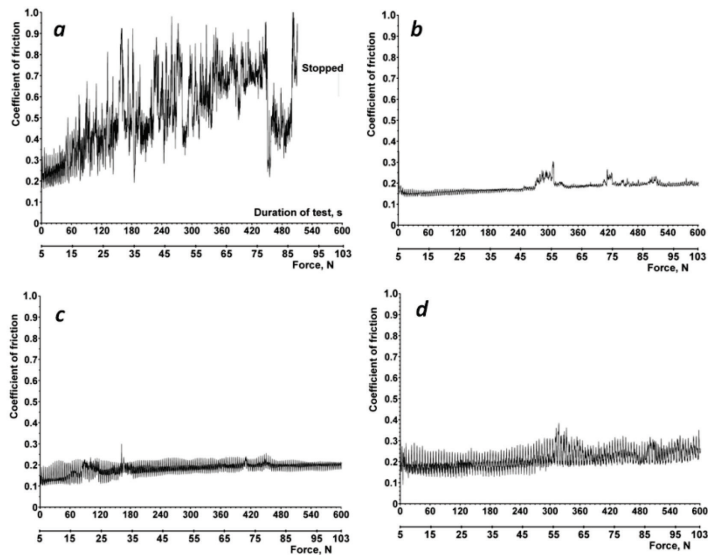

Figure 3.11 The effect of load on the coefficient of friction of reference flat surface (a) and cellular lattice structures with strut diameters 0.15 (b), 0.20 (c) and 0.30 mm (d) (adapted from Publication III).

3.3.3 Performance of cellular lattice structures used as stacks in thermoacoustic heat engine

In Publication IV, various stacks were tested in a small-scale standing-wave thermoacoustic heat engine setup. Figure 3.12 shows the general view and SEM images of the lattice structure (stack 6) used in the present study.

The measurement of the acoustic pressure was performed with the microphone located at 100 mm from the open end of the tube, and the temperature difference across the stack measured by the thermocouples located in the proximity of lattice sides. It is important to notice that due to the location of the thermocouples, there is a temperature gap between the measured temperatures and the actual temperature of the hot and cold surfaces of the stack.
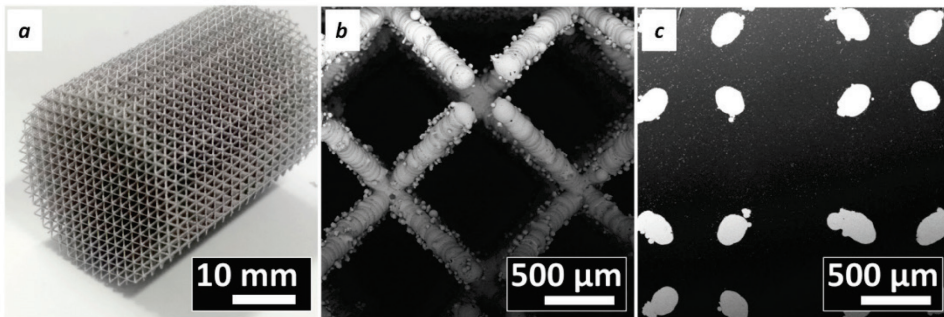

Figure 3.12 3D-printed lattice (stack 6), general view (a) and SEM images: as-printed (b) and cross section (c) (adapted from Publication IV).

Figure 3.13 shows the thermoacoustic behavior of the specimens when a heat flow is applied. Acoustic pressure (blue) and temperature difference (red) in real time are presented on the graphs. When the temperature difference reaches a certain threshold (about 100 to 150 K), the thermoacoustic effect takes place, and the subsequent temperature distribution within and around the stack depends on the thermos-fluid-dynamic characteristics of the stack.

Stacks with various geometries (Table 2.4) were tested at the same conditions. The behavior of stack 3 and stack 4 is similar. The level of acoustic pressure was decreased after thermoacoustic emission started. The emission stopped in a short time. For stack 5, no thermoacoustic effect occurred. Stacks 1, 2 and 6 exhibited the most stable thermoacoustic behavior during the test. Stack 1 and stack 6 generated the highest thermoacoustic pressure, so these struts were additionally tested at high heat power (Fig. 3.14). The level of exhibited acoustic pressure reached 2700 Pa. However, in the case of stack 1, it was continuously decreasing, and emission stopped at approximately 275 s of the test. The thermoacoustic behavior of stack 6 (lattice) was stable for the whole duration of the test with higher acoustic pressure levels. More details are presented in Publication IV.

The lattice structure presented in Figure 3.12 (stack 6) was found to be the best among the tested stacks in terms of stability and level of exhibited acoustic emission.
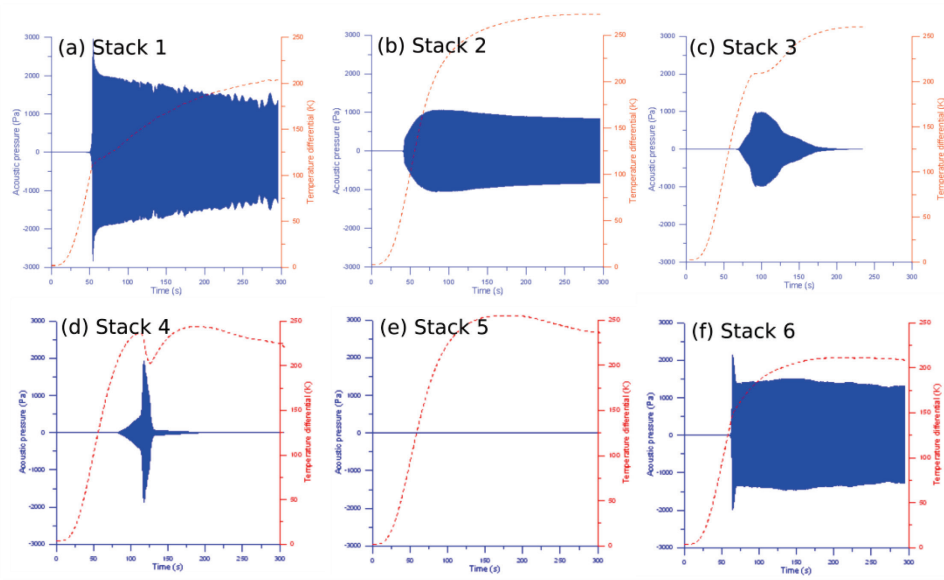
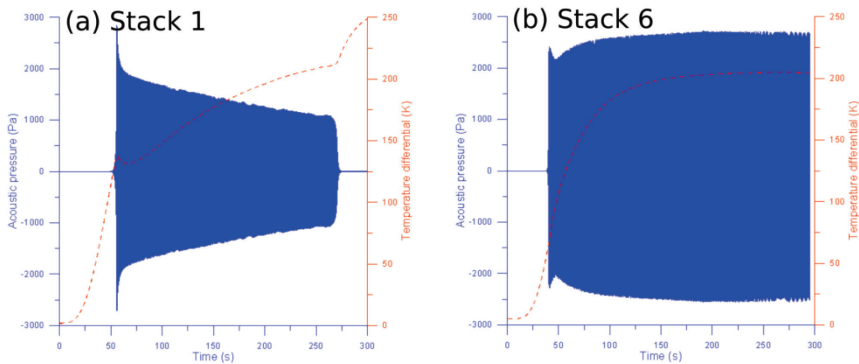*Figure 3.13 Thermoacoustic behavior of stacks with various geometries.*

Figure 3.14 Thermoacoustic behavior of stack 1 (parallel plates) and stack 6 (lattice structure) at high heat power.

In order to validate the influence of the lattice post-treatment on the thermoacoustic performance, the selected stack geometry produced from stainless steel AISI 316L was nitrided with applied overpressure (N1 conditions). TAE experiments were conducted by using similar small-scale standing-wave thermoacoustic heat engine setup as in Publication IV. The stacks were tested using equal conditions to provide comparable results. Measured thermoacoustic pressure generated by untreated and nitrided lattices is shown in Figure 3.15.

The stacks show the anticipated onset that occurs when the temperature difference between hot and cold heat exchangers reaches 100 °C. It happens at ~35 s of the process. The acoustic pressure levels exhibited by 316L stack was up to ~1370 Pa. The behavior was relatively stable until the end of the test. Only a slight decrease in the acoustic pressure was observed between ~125 and ~175 s of the test with a minimum recorded value of ~1200 Pa.
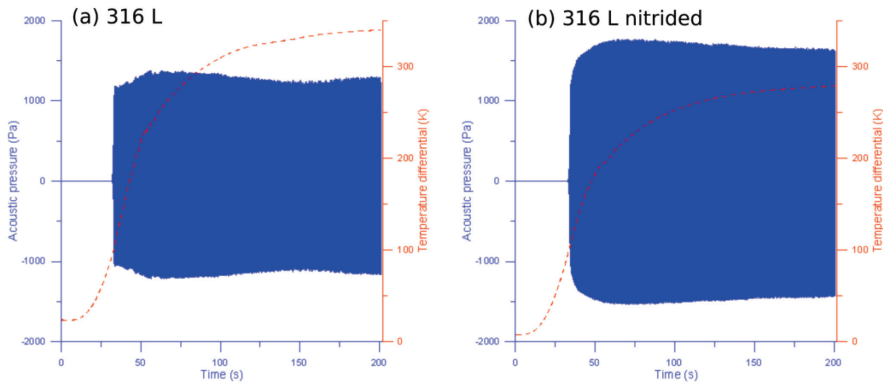
Figure 3.15 Thermoacoustic behavior of lattice stacks (stack 6) produced from stainless steel AISI 316L (a) and nitrided AISI 316L (b).

Nitriding of the 316L lattice has led to an increase in the acoustic pressure to ~1770 Pa. From the beginning to the end of the test, the behavior was very stable and no deviations were observed.

The Fourier transform was used to decompose a signal (a function of time) into its constituent frequencies. Figure 3.16 shows the recorded signal generated by the lattice stacks produced from different materials after Fourier transformation. There is one main frequency followed by a few harmonics. High-frequency domains tend to shift with time. It is also noticeable that some emission was detected before the start of the thermoacoustic effect.
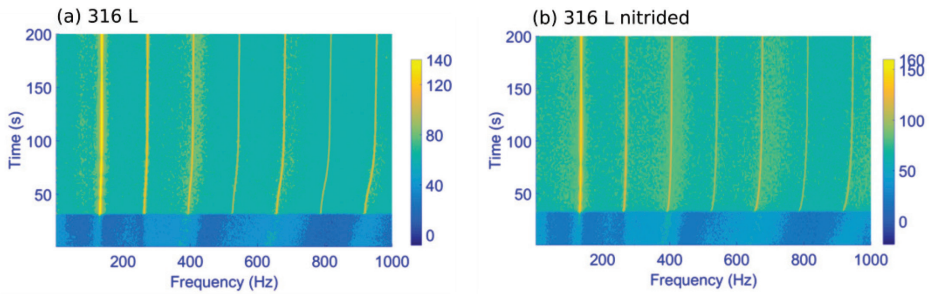

Figure 3.16 Fourier transforms of recorded signal generated by lattice stacks produced from stainless steel AISI 316L (a) and nitrided AISI 316L (b).

4 DISCUSSION

4.1 Fabrication of cellular lattice structures

Cellular lattice structures were obtained by pulsed laser scanning strategy via SLM and DED techniques. Laser exposure in a single point allows achieving the smallest size of the lattice feature. Generally, the smallest size of the feature is limited physically by the powder particle sizes, laser spot size, etc. However, some applications require a very thin lattice feature, for example, in thermoacoustics it leads to increasing the performance of the stacks. The thinnest lattice achieved by SLM average strut diameter in this work was 155 µm. The limiting factors for decreasing the strut diameter are laser spot size and particle size of the feedstock powder. Strut diameter increases with the laser power and exposure time. However, high LP and ET values lead to more intensive spattering effect, which increases the risk of printing defect due to the depositing of large droplets on the cross-sectional areas to be treated by laser.

To obtain cellular lattice structures via DED, layer thickness has to be defined. Generally, for the tested parameters, LT decreases with LP. However, for the highest tested ET (30 ms), the dependence was found to be the opposite. The reason lies in the geometry of the deposited material. Figure 4.1 shows a schematic illustration of the geometry of a single deposited spot of material with various parameters. In a regular deposition process, track geometry (height and width) depends on the laser power, scanning speed, and powder flow rate [74]. In the present case, the powder flow rate is fixed, and scanning does not occur, only single exposures take place. The shape of the single spot is related to the amount of material melted by a certain laser power during a specific ET and surface tension, which forms the geometry of the deposited spot.
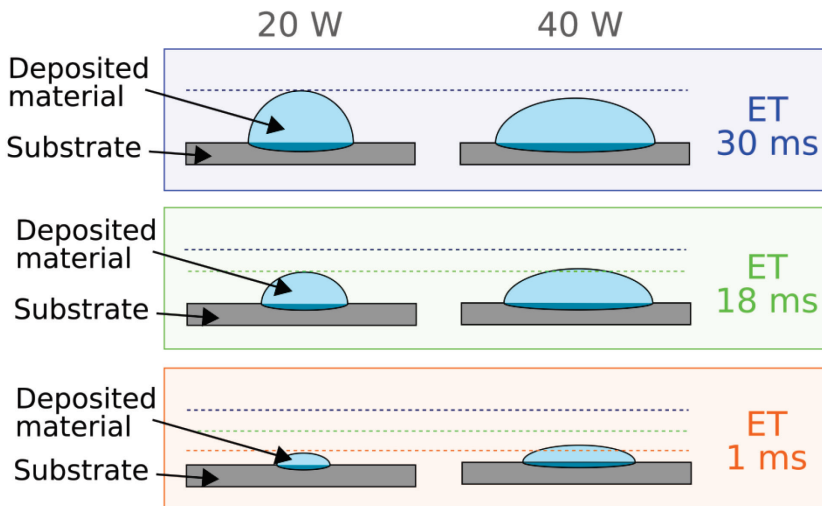
Figure 4.1 Schematic illustration of the geometry of single deposited spot with various parameters.

The smallest obtained lattice strut diameter via DED was 160 µm, which is similar to SLM. However, two significant advantages were noticed. Due to the fact that there is no powder bed, a significantly smaller amount of bonded particles are connected to the strut surface. The surface of the thinnest strut obtained via SLM is almost entirely

covered with partially melted particles that make the strut cross-section non-uniform along its length. The second advantage is the possibility of obtaining smaller unit cell sizes. The smallest cell size obtained via DED was 0.5 mm, which is hardly achievable by SLM due to building up of the part above the powder bed level, which causes the failure of the printing job.

Detected disadvantages of the DED method to produce a cellular lattice structure are the relatively high limitation for the inclination angle (60 degrees and higher) and porosity. The porosity formation can be attributed to the next reasons. It could be gained from the initial powder. Such a phenomenon was confirmed by Murr et al. [75] when closed porosity formed by argon bubbles in the atomized powder remains in the material after the EBM process. The porosity can also be formed during the process when transportation or shielding gas is entrapped between neighboring powder particles.

In order to recognize the main reason of porosity formation, feedstock powder particles were embedded into resin and polished. The initial porosity of the powder is almost absent, and the sizes of the pores in the powder are much smaller than those detected in the cladded structures. It proves that the porosity of the lattices was gained additionally during the process by gas entrapping between powder particles. Figure 4.2 provides a schematic illustration of the probability of gas trapping between powder particles.
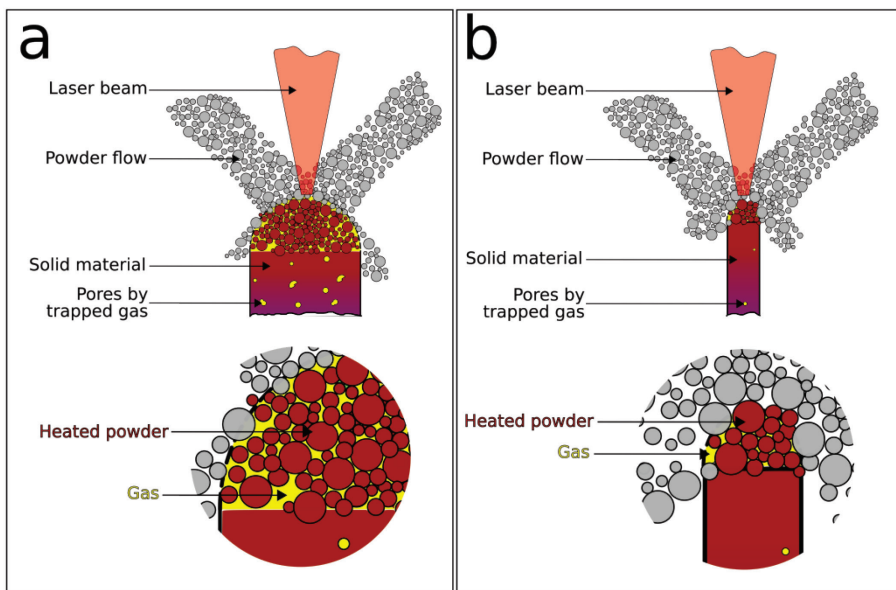

Figure 4.2 Schematic illustration of the probability of gas trapping between powder particles during the DED process in the thick (a) and thin (b) struts.

During laser exposure, particles melt rapidly. Liquid metal surrounds gas and forms bubbles. Decreasing the number of particles that are melted should provide less potential places for trapping the gas. It is the reason why lattices with the smallest strut diameter exhibit the lowest porosity, being almost pore-free (Fig. 3.4 d). The strut diameter of these lattices is equal to only a few powder particle sizes. Accordingly, in this case, there are significantly fewer possible places for gas entrapping between the

particles. The porosity of the lattices with the smallest strut diameter obtained via DED is comparable with lattices produced by SLM.

4.2 Post-processing of cellular lattice structures

Preliminary post-treatment tests show that applied overpressure during nitriding has a positive effect on the acceleration of the process. The penetration depth is also influenced by the cylinder diameter (Fig. 4.3 a-c). Microstructural observations have detected two types of inclusions for N1 conditions: elongated inclusions with round and elongated shape (Fig. 4.3 b, c). The presence of two different inclusions types is related to the nitriding process specifics. Beginning of nitriding forces carbide-rich particles formed from the carbon, which was present in the initial material composition, to precipitate at grain boundaries, after which carbide-rich zone moves more profoundly into the specimen while nitrides start appearing on the surface. At some point of the process, in the way of the nitriding front, eventually, all carbides disappear due to decarburization [76].
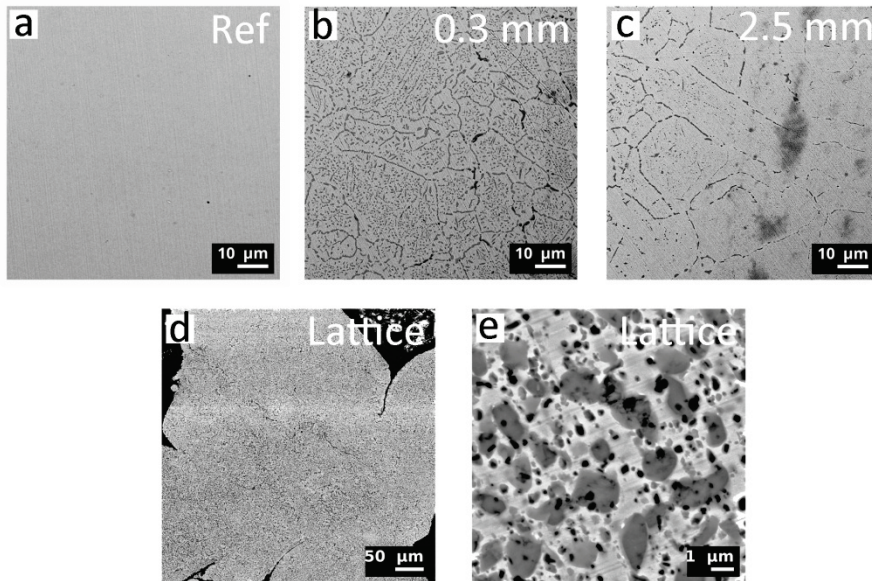

Figure 4.3. The microstructure of nitrided specimens, untreated (a); nitrided with diameter 0.3 mm (b); 0.5 mm (c) and lattice (d, e) with strut diameter ~0.2 mm.

Elongated inclusions at the grain boundaries were not observed in the lattices treated under N1 conditions (Fig. 4.3 d, e). They disappeared because of the strut diameter differences. The lattice strut diameter is less than preliminarily tested 0.3 mm and approximately equal to 0.2 mm. Smaller strut diameter causes a faster nitriding process. According to the EDS and XRD data and data reported in the literature [76], elongated inclusions are carbide-rich particles from the initial material precipitated at grain boundaries. Although the nitriding conditions are equal, decreasing the strut diameter accelerates the decarburization.

Preliminary carburizing tests show that 20 min at 1000 °C in CH4 flow is not enough even for complete modification of the smallest 0.3 mm cylinder. The penetration depth

is slightly above 120 µm. Increase in the specimen's diameter leads to a decrease in the penetration depth. Following dwelling in the furnace at 1150 °C for 60 min causes noticeable growth of the depth of penetration and the size of the inclusions. Deposited carbon from the specimen's surface diffused to the volume. Lower heating and cooling rates contribute to the microstructure homogenization and the increasing of the size of inclusion. The penetration depth of C3 conditions is compatible with C2 in the case of specimens with 0.3 and 0.5 diameters. However, for larger diameters, C3 conditions exhibit deeper penetration. The reason for this is a continuous carbon source (CH_4) during the process that supplies excess carbon to the external surface, while carbon in the material diffuses to the volume of the specimen. The second stage of C2 conditions is limited only to the amount of carbon deposited on the surface of the sample in the solid phase. Smaller lattice strut diameter in the case of C2 parameter resulted in significant size increase of carbide-rich phase inclusions and some porosity formation (Fig. 4.4). The size of pores is less than 1 µm. The main possible reason of the porosity formation is the difference in the diffusion rates between chromium and iron or nickel. Chromium diffuses faster than iron or nickel [77], it also tends to form carbides first. Vacancies formed by the migration of Cr atoms cannot be fulfilled by atoms of other elements with the same speed. It leads to so-called diffusion porosity or the Kirkendall and Frenkel effect [78].
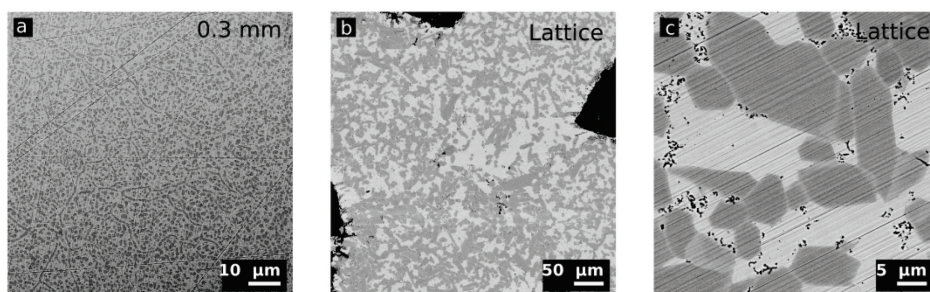

Figure 4.4 The microstructures of the specimen with diameter 0.3 mm (a) and lattice (b, c) carburized under C2 conditions.

4.3 Properties of metal and metal-ceramic lattices

4.3.1 Mechanical properties

Microhardness values of thermochemically treated specimens are in general higher compared to untreated stainless steel. However, for nitrided samples with diameter 2.5 mm, the Vickers microhardness values were comparable with the reference value taken from untreated 316L, which is caused by slow nitriding speed. The same effect was observed for carburized specimens after C1 treatment due to short carburizing time. Nitrided lattices (N1) have higher hardness values than carburized (C2) ones, being 605 HV0.3 and 576 HV0.3 respectively. It can be related to higher hardness of chromium nitrides [79] when compared to chromium carbides [80].

Generally, a compressive strength of the lattices depends on the relative density of the lattice, defects and unit cell geometry. The layer thickness also influences the strength of the lattices obtained by the pulsed laser scanning strategy as it affects the bonding strength with the previous layer due to simple geometrical dependencies. Increasing the layer thickness resulted in increasing the horizontal displacement

between the previous laser exposure point and the next one on the next layer [Publication I]. This contributes to a weaker connection between the layers, and the overall lattice strength is decreasing. The negative effect of increasing the thickness of the layer can be compensated by increasing the strut's inclination angle. Schematic explanation of the effect of layer thickness and inclination angle on the connection between the layers is represented in Figure 4.5.
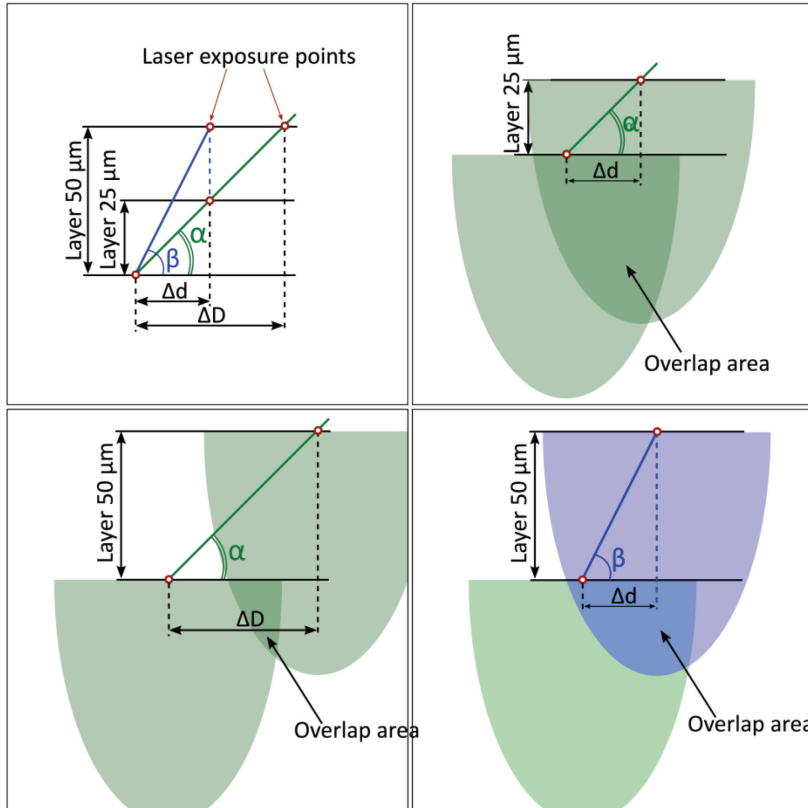

Figure 4.5 Schematic illustration of the influence of layer thickness and inclination angle on the connection between layers.

PUBLICATION II describes the compressive yield strength values of cellular lattice structures with various relative densities produced from the untreated, nitrided and carburized AISI 316L. The obtained results, in general, correlate with the Gibson–Ashby model [81] with R = 0.9865. Nevertheless, the experimental results slightly differ from the calculated data. The difference is related to the residual stresses and more complex geometry of the lattice surface caused by bonded particles [4].

Nitrided and carburized lattices exhibited elevated brittleness compared to untreated ones and collapsed at some point of testing [Publication II]. Untreated stainless steel lattices did not collapse during the testing up to 50% of deformation until the test was stopped due to the programmed limit. Nitrided lattices exhibited 2–3% deformation in the elastic zone before collapsing. Carburized lattices deformed about 4.5 to 8% before critical failure for lattices with the lowest and with the highest relative density respectively. Lower plasticity of nitrided lattices is related to several reasons. First of all,

the structure of the nitrided layer may be divided into two sublayers: a compound zone and a nitrogen diffusion zone [48,76], both consisting of the nitrides Fe_3N (detected by XRD), which is known to be hard but very brittle. The second reason is the formation of chromium nitrides that are harder than chromium carbides and, as a consequence, more brittle. Also, carburized layers usually contain some amount of the metallic phase (ferrite or austenite), which provides relatively high plasticity to the carburized lattice structure.

In conclusion, carburizing was found to be more effective for the improvements of the mechanical properties of the lattice. Based on the general relationship between hardness values and wear resistance of materials [82–84], it can be assumed that carburizing can have a positive effect on the wear resistance of the cellular lattice structures. The influence of lattice post-processing on the tribological behavior has to be studied in the future work.

4.3.2 Tribological behavior of cellular lattice structures

It is generally known that for some special applications it is essential to reduce the friction, improving the lubrication properties as well as reduce the generation of wear debris at the contact surfaces. A possible way of changing the tribological characteristics is the modification of surface texture. Patterning of the wear surface for the bearings and artificial hip implants with dimples confirmed a reduction of abrasive wear and increasing of the lifetime of a product [9,85]. Additive technologies make it possible to improve this approach by applying complex geometrical patterning, which can lead to a better result.

Publication III focuses on the tribological performance of various 3D printed patterns tested in dry sliding conditions. It was shown that usage of dimples provides a positive effect on the frictional behavior by stabilizing the sliding (reduced variation in COF) compared to the reference flat surface. However, a lattice structure as a surface pattern performs better than the dimples. The reason may be a decrease in the abrasive wear level by providing an escape route for wear debris from the wear surface into the dimples of lattice free space. Three different lattice types were tested, the unit cell size was equal, but the strut diameter was 0.15, 0.2 and 0.3 mm. Among them, the lattice with the thinnest struts has shown the lowest and most stable COF with minimal deviations. A possible explanation for this phenomenon lies in the specifics of the wear mechanism of the flat surface and lattice structure.

In the case of a flat specimen, strong adhesion of contacting bodies results in the initiation of so-called solid-phase welding [86]. The wear fragment keeping between the bodies is carrying the whole load that results in rolling and sliding of such fragments along the whole surface width. The fragment is growing during the rolling and sliding. It damages both surfaces (Fig. 4.6 a). Damaged surface provides favorable conditions for the generation of new fragments. The addition of dimples provides a discontinuous surface, which leads to a reduction in the maximum possible size of the wear element. At some point, the dimples remove wear element from the contact surface and store them. The surface of the lattice consists of many small elements and relatively large (3-5 times larger in size) areas of empty space. The probability of the formation and growth of wear fragments is reduced due to the reduction of the contact area. Even if such elements managed to form, they could grow to only small sizes before being removed into the internal volume of the lattice. So, the surface damaging is minimal. Empty space between the struts also provides storing of these small wear fragments that might later escape from the lattice internal empty volume (Fig. 4.6 b).
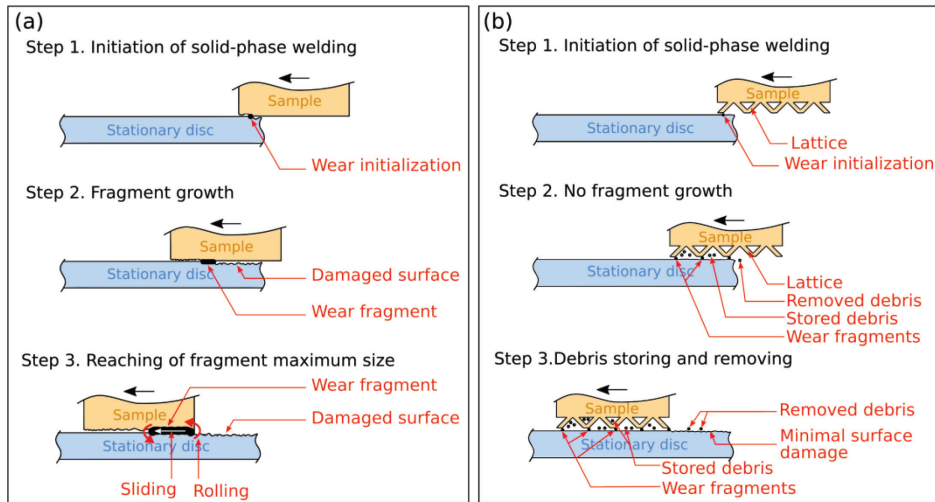
Figure 4.6 Schematic representation of wear fragments formation in case of flat mating surfaces.

The empty volume inside the dimples is quite limited and can be filled by debris with time. It increases the COF and makes the wear behavior closer to the flat surface. In the case of lattices, such a phenomenon was partially observed only for the lattice with the largest struts, 0.3 mm (Fig. 3.10 c).

DED process can be used as an additional step to functionalize the surface of existing parts (Fig. 4.7) in order to provide specific tribological properties, as shown in Publication III. A green part may be produced by conventional techniques, which decreases the total production time and the final cost of the part. Fabrication of cellular lattice structures on such non-planar surfaces is also possible with some additional software adjustments. Another reason for fabrication of the lattice structure layer on the surface of the green part can be adding of the hard metal layer in the specific places where it is needed [87].

Figure 4.7 Pin structure deposited via DED on the curved surface.

4.3.3 Thermoacoustic performance of cellular lattice structures

It is well known that pin stacks are more effective than plate stacks in the case of TAE performance [10,88]. However, they were not widely applied in TAE due to the complicated manufacturing process of such stacks. Additive manufacturing allows overpassing this production limitation. Even more, it will enable producing more

complex geometries such as lattice structures that combine the advantages of the pin stacks with other effects derived from the lattice shape.

Experiments proved that cellular lattice structures could be efficiently used as a stack in TAE. Metal lattice and nitrided lattice were tested. The lattice geometry and testing conditions were equal, but the thermoacoustic performance had some variations.

The highest acoustic pressure was observed for the lattices produced by nitriding of 316L. The result is in good correlation with the thermal conductivity values. Nitrided lattice contains CrN and Fe_3N phases [Publication II]. The thermal conductivity of CrN is much lower than 316L, 3.6 and 13.53 W/m K respectively [89–91]. Lower thermal conductivity keeps a higher temperature gradient between hot and cold heat exchangers, which leads to increased performance.

Harmonics frequencies are shifting with time (Fig.3.16), which is attributed to the material properties changes during heating. Frequency shift stops once the temperature difference between the hot and cold side of the stack becomes stable.

Further investigations can address the thermoacoustic performance of lattice structures with various geometries to determine the dependence of thermoacoustic behavior on the unit cell shape and size and select the most effective one. Another challenge is to produce the lattice stack with the most capable geometry from a ceramic material with low thermal conductivity in order to achieve maximal efficiency. After that, thermoacoustic energy obtained from TAE can be converted to electric power by using a piston carrying neodymium magnets. Sun concentrators can be applied to heat up the stack in TAE [92] and generate electric energy from a renewable source.

5 CONCLUSIONS

The present work was focused on the development and production optimization of metal and metal-ceramic cellular lattice structures. The main focus was on disclosing the potential of cellular lattice structures in tribological and thermoacoustical applications.

Based on the results of the present study, the following conclusions can be drawn:

- Cellular lattice structures with the feature size in order of 100-200 µm were successfully produced via SLM and DED using pulsed laser scanning strategy.
- The relationship between process parameters and produced lattice features was defined in both cases.
- Metal-ceramic cellular lattice structures were successfully produced by the two-step approach, using carburizing and nitriding as post-processing procedures.
- The formation of the microstructure and the phase composition of obtained metal-ceramic lattices were investigated.
- Examination of mechanical properties of produced metal-ceramic structures shows higher hardness, strength and brittleness of the structures compared to those of metallic structures. Microhardness increased around three times, compressive strength – from 21 to 65% depending on the relative density of the lattice.
- New application areas for metal and metal-ceramic cellular lattice structures were introduced.
- Tribological tests of the cellular lattice structures show stable and low coefficient of fiction. Surface damage is minimal compared to reference specimen. Wear debris are removed from sliding surfaces into the internal volume of the structure and later escape due to the so called self-cleaning effect.
- Reducing the thermal conductivity of the material leads to the improved thermoacoustic performance of the stack. Decreasing the thermal conductivity of the lattice structure by nitriding resulted in 30% higher acoustic pressure.

FUTURE WORK

Future research in the field of tribology should address the effects of cellular lattice structures on the wear more carefully. Studies of the influence of thermochemical treatment of the lattices on their wear performance will be essential.

Cellular lattice structures exhibited promising results in thermoacoustics. This is an interesting topic for future work. Further investigations can focus on the determination of the most efficient lattice geometry. AM enables producing functionally graded lattices. Their thermoacoustic performance should be studied. Integration of cooling channels directly to the lattice to increase the efficiency of the cold heat exchanger can be a topic of the future research. Additionally, to produce ceramic lattice structures, the fabrication technique should be chosen and tested. Subsequently, to generate green electrical energy from a renewable source, the thermoacoustic engine setup equipped with sun concentrators to heat the stack should be developed and tested.

References

[1]   H. Kodama, Automatic method for fabricating a three-dimensional plastic model with photo-hardening polymer, *Rev. Sci. Instrum.* 52 (1981) 1770–1773.

[2]   C.W. Hull, C. Arcadia, Apparatus for production of three-dimensional objects by stereolithography, 1986.

[3]   L. Hao, D. Raymont, C. Yan, A. Hussein, P. Young, Design and additive manufacturing of cellular lattice structures, in: Innov. *Dev. Virtual Phys. Prototyp.*, 2011: pp. 249–254.

[4]   C. Yan, L. Hao, A. Hussein, S.L. Bubb, P. Young, D. Raymont, Evaluation of light-weight AlSi10Mg periodic cellular lattice structures fabricated via direct metal laser sintering, *J. Mater. Process. Technol.* 214 (2014) 856–864.

[5]   C. Yan, L. Hao, A. Hussein, D. Raymont, Evaluations of cellular lattice structures manufactured using selective laser melting, *Int. J. Mach. Tools Manuf*. 62 (2012) 32–38.

[6]   L. Nickels, AM and aerospace: an ideal combination, *Met. Powder Rep.* 70 (2015) 300–303.

[7]   C. San Marchi, M. Kouzeli, R. Rao, J.A. Lewis, D.C. Dunand, Alumina-aluminum interpenetrating-phase composites with three-dimensional periodic architecture, *Scr. Mater.* 49 (2003) 861–866.

[8]   O. Al-Ketan, M. Adel Assad, R.K. Abu Al-Rub, Mechanical properties of periodic interpenetrating phase composites with novel architected microstructures, *Compos. Struct.* 176 (2017) 9–19.

[9]   H. Ito, K. Kaneda, T. Yuhta, I. Nishimura, K. Yasuda, T. Matsuno, Reduction of polyethylene wear by concave dimples on the frictional surface in artificial hip joints, *J. Arthroplasty*. 15 (2000) 332–338.

[10]   G.W. Swift, R.M. Keolian, Thermoacoustics in pin-array stacks, *J. Acoust. Soc. Am.* 94 (1993) 941–943.

[11]   K. Prashanth, L. Löber, H.-J. Klauss, U. Kühn, J. Eckert, Characterization of 316L Steel Cellular Dodecahedron Structures Produced by Selective Laser Melting, *Technologies.* (2016).

[12]   T. Minasyan, L. Liu, Y. Holovenko, S. Aydinyan, I. Hussainova, Additively manufactured mesostructured $MoSi_2$-Si_3N_4 ceramic lattice, *Ceram. Int.* 45 (2019) 9926-9933.

[13]   D. Manfredi, F. Calignano, E.P. Ambrosio, M. Krishnan, R. Canali, S. Biamino, M. Pavese, E. Atzeni, L. Luliano, P. Fino, C. Badini, Direct Metal Laser Sintering: An additive manufacturing technology ready to produce lightweight structural parts for robotic applications, *Metall. Ital.* 105 (2013) 15–24.

[14]   C. Mota, D. Puppi, F. Chiellini, E. Chiellini, Additive manufacturing techniques for the production of tissue engineering constructs, *J. Tissue Eng. Regen. Med.* 9 (2015) 174–190.

[15] F.P.W. Melchels, J. Feijen, D.W. Grijpma, A poly(d,l-lactide) resin for the preparation of tissue engineering scaffolds by stereolithography, Biomaterials. 30 (2009) 3801–3809.

[16] M.R. Karamooz Ravari, M. Kadkhodaei, M. Badrossamay, R. Rezaei, Numerical investigation on mechanical properties of cellular lattice structures fabricated by fused deposition modeling, *Int. J. Mech. Sci.* 88 (2014) 154–161.

[17] S. Tarafder, V.K. Balla, N.M. Davies, A. Bandyopadhyay, S. Bose, Microwave-sintered 3D printed tricalcium phosphate scaffolds for bone tissue engineering, *J. Tissue Eng. Regen. Med.* 7 (2013) 631–641.

[18] B. Duan, W.L. Cheung, M. Wang, Optimized fabrication of Ca-P/PHBV nanocomposite scaffolds via selective laser sintering for bone tissue engineering, Biofabrication. 3 (2011).

[19] H. Alsalla, L. Hao, C. Smith, Fracture toughness and tensile strength of 316L stainless steel cellular lattice structures manufactured using the selective laser melting technique, *Mater. Sci. Eng. A.* 669 (2016) 1–6.

[20] M. Sharma, H. Dobbelstein, M. Thiele, A. Ostendorf, Laser metal deposition of lattice structures by columnar built-up, *Procedia CIRP.* 74 (2018) 218–221.

[21] W.E. Frazier, Metal additive manufacturing: A review, *J. Mater. Eng. Perform.* 23 (2014) 1917–1928.

[22] M. Saunders, How process parameters drive successful metal AM part production, *Met. Addit. Manuf.* Vol. 4 No. 2. (2018) 127–135.

[23] F. Brueckner, M. Riede, F. Marquardt, R. Willner, A. Seidel, S. Thieme, C. Leyens, E. Beyer, Process characteristics in high-precision laser metal deposition using wire and powder, *J. Laser Appl.* 29 (2017) 022301.

[24] D. Lehmhus, M. Busse, A.S. Herrmann, K. Kayvantash, Structural Materials and Processes in Transportation, 2013.

[25] M. Ashby, Designing architectured materials, *Scr. Mater.* 68 (2013) 4–7.

[26] M.F. Ashby, The properties of foams and lattices, *Philos. Trans. R. Soc. A Math. Phys. Eng. Sci.* (2006).

[27] Q. Liu, Literature review: materials with negative poisson's ratios and potential applications to Aerospace and Defence, *Aust. Gov. Dep. Def.* (2006) 1–47.

[28] L.J. Gibson, M.F. Ashby, The Mechanics of Three-Dimensional Cellular Materials, *Proc. R. Soc. A Math. Phys. Eng. Sci.* 382 (1982) 43–59.

[29] V.J. Challis, X. Xu, L.C. Zhang, A.P. Roberts, J.F. Grotowski, T.B. Sercombe, High specific strength and stiffness structures produced using selective laser melting, *Mater. Des.* 63 (2014) 783–788.

[30] C. Yan, L. Hao, A. Hussein, D. Raymont, Evaluations of cellular lattice structures manufactured using selective laser melting, *Int. J. Mach. Tools Manuf.* 62 (2012) 32–38.

[31] S. McKown, Y. Shen, W.K. Brookes, C.J. Sutcliffe, W.J. Cantwell, G.S. Langdon, G.N. Nurick, M.D. Theobald, The quasi-static and blast loading response of lattice structures, *Int. J. Impact Eng.* 35 (2008) 795–810.

[32] T. Tancogne-Dejean, A.B. Spierings, D. Mohr, Additively-manufactured metallic micro-lattice materials for high specific energy absorption under static and dynamic loading, *Acta Mater.* 116 (2016) 14–28.

[33] M. Leary, M. Mazur, J. Elambasseril, M. McMillan, T. Chirent, Y. Sun, M. Qian, M. Easton, M. Brandt, Selective laser melting (SLM) of AlSi12Mg lattice structures, *Mater. Des.* 98 (2016) 344–357.

[34] C. Yan, L. Hao, A. Hussein, P. Young, J. Huang, W. Zhu, Microstructure and mechanical properties of aluminium alloy cellular lattice structures manufactured by direct metal laser sintering, *Mater. Sci. Eng. A.* 628 (2015) 238–246.

[35] C. Yan, L. Hao, A. Hussein, P. Young, Ti-6Al-4V triply periodic minimal surface structures for bone implants fabricated via selective laser melting, *J. Mech. Behav. Biomed. Mater.* 51 (2015) 61–73.

[36] B. Gorny, T. Niendorf, J. Lackmann, M. Thoene, T. Troester, H.J. Maier, In situ characterization of the deformation and failure behavior of non-stochastic porous structures processed by selective laser melting, *Mater. Sci. Eng*. A. 528 (2011) 7962–7967.

[37] A. Yánez, A. Herrera, O. Martel, D. Monopoli, H. Afonso, Compressive behaviour of gyroid lattice structures for human cancellous bone implant applications, *Mater. Sci. Eng. C.* 68 (2016) 445–448.

[38] D.A. Ramirez, L.E. Murr, S.J. Li, Y.X. Tian, E. Martinez, J.L. Martinez, B.I. Machado, S.M. Gaytan, F. Medina, R.B. Wicker, Open-cellular copper structures fabricated by additive manufacturing using electron beam melting, *Mater. Sci. Eng. A*. 528 (2011) 5379–5386.

[39] D. Gu, Y.C. Hagedorn, W. Meiners, K. Wissenbach, R. Poprawe, Nanocrystalline TiC reinforced Ti matrix bulk-form nanocomposites by Selective Laser Melting (SLM): Densification, growth mechanism and wear behavior, *Compos. Sci. Technol.* 71 (2011) 1612–1620.

[40] D. Gu, G. Meng, C. Li, W. Meiners, R. Poprawe, Selective laser melting of TiC/Ti bulk nanocomposites: Influence of nanoscale reinforcement, *Scr. Mater*. 67 (2012) 185–188.

[41] D. Gu, H. Wang, G. Zhang, Selective laser melting additive manufacturing of Ti-based nanocomposites: The role of nanopowder, *Metall. Mater. Trans. A Phys. Metall. Mater. Sci.* 45 (2014) 464–476.

[42] Q. Han, R. Setchi, S.L. Evans, Synthesis and characterisation of advanced ball-milled Al-Al2O3 nanocomposites for selective laser melting, *Powder Technol.* 297 (2016) 183–192.

[43] J. Deckers, J. Vleugels, J.P. Kruth, Additive manufacturing of ceramics: A review, *J. Ceram. Sci. Technol.* 5 (2014) 245–260.

[44] K. Shahzad, J. Deckers, S. Boury, B. Neirinck, J.-P. Kruth, J. Vleugels, Preparation and indirect selective laser sintering of alumina/PA microspheres, *Ceram. Int.* 38 (2012) 1241–1247.

[45] K. Shahzad, J. Deckers, Z. Zhang, J.P. Kruth, J. Vleugels, Additive manufacturing of zirconia parts by indirect selective laser sintering, *J. Eur. Ceram. Soc.* 34 (2014) 81–89.

[46] K. Liu, Y. Shi, C. Li, L. Hao, J. Liu, Q. Wei, Indirect selective laser sintering of epoxy resin-Al2O3ceramic powders combined with cold isostatic pressing, *Ceram. Int.* 40 (2014) 7099–7106.

[47] B. Edenhofer, D. Joritz, M. Rink, K. Voges, 13 – Carburizing of steels, 2015.

[48] D. Pye, Practical nitriding and ferritic nitrocarburizing, 2003.

[49] M. Chechel, A. Glotka, W.A.-R. Dhafer, V. Kostyk, K. Kostyk, The choice of the optimal temperature and time parameters of gas nitriding of steel, *Eastern-European J. Enterp. Technol.* 3 (2016) 44.

[50] Y. Tang, A. Kurtz, Y.F. Zhao, Bidirectional Evolutionary Structural Optimization (BESO) based design method for lattice structure to be fabricated by additive manufacturing, *CAD Comput. Aided Des*. 69 (2015) 91–101.

[51] D. Kuksenko, H.J. Böhm, B. Drach, Effect of micromechanical parameters of composites with wavy fibers on their effective response under large deformations, *Adv. Eng. Softw*. 121 (2018) 206–222.

[52] H. Prüß, T. Vietor, Design for Fiber-Reinforced Additive Manufacturing, *J. Mech. Des.* 137 (2015) 111409.

[53] D. Kuksenko, B. Drach, I. Tsukrov, Prediction of damage initiation and simulation of damage propagation in 3D woven composites during processing, in: *32nd Tech. Conf. Am. Soc. Compos*. 2017, 2017.

[54] M. Ansar, W. Xinwei, Z. Chouwei, Modeling strategies of 3D woven composites: A review, *Compos. Struct.* 93 (2011) 1947–1963.

[55] O. Al-Ketan, R.K.A. Al-Rub, R. Rowshan, Mechanical Properties of a New Type of Architected Interpenetrating Phase Composite Materials, *Adv. Mater. Technol*. 2 (2017) 1600235.

[56] S.L. Sing, L.P. Lam, D.Q. Zhang, Z.H. Liu, C.K. Chua, Interfacial characterization of SLM parts in multi-material processing: Intermetallic phase formation between AlSi10Mg and C18400 copper alloy, *Mater. Charact.* 107 (2015) 220–227.

[57] A.E. Pawlowski, Z.C. Cordero, M.R. French, T.R. Muth, J. Keith Carver, R.B. Dinwiddie, A.M. Elliott, A. Shyam, D.A. Splitter, Damage-tolerant metallic composites via melt infiltration of additively manufactured preforms, *Mater. Des.* 127 (2017) 346–351.

[58] J.D. Bobyn, G.J. Stackpool, S.A. Hacking, M. Tanzer, J.J. Krygier, Characteristics of bone ingrowth and interface mechanics of a new porous tantalum biomaterial, *J. Bone Jt. Surg*. 81 (1999) 907–914.

[59] S. a Hacking, E.J. Harvey, M. Tanzer, J.J. Krygier, J.D. Bobyn, Acid-etched microtexture for enhancement of bone growth into porous-coated implants., *J. Bone Joint Surg. Br.* 85 (2003) 1182–1189.

[60] J.D. Bobyn, Zoledronic acid causes enhancement of bone growth into porous implants, *J. Bone Jt. Surg. Br.* 87–B (2005) 416–420.

[61]   H.W. Kim, J.C. Knowles, H.E. Kim, Hydroxyapatite porous scaffold engineered with biological polymer hybrid coating for antibiotic Vancomycin release, *J. Mater. Sci. Mater. Med.* 16 (2005) 189–195.

[62]   Q. Yao, P. Nooeaid, J.A. Roether, Y. Dong, Q. Zhang, A.R. Boccaccini, Bioglass®-based scaffolds incorporating polycaprolactone and chitosan coatings for controlled vancomycin delivery, *Ceram. Int.* 39 (2013) 7517–7522.

[63]   Q. Yao, Y. Liu, B. Selvaratnam, R.T. Koodali, H. Sun, Mesoporous silicate nanoparticles/3D nanofibrous scaffold-mediated dual-drug delivery for bone tissue engineering, *J. Control. Release*. 279 (2018) 69–78.

[64]   L.E. Murr, S.M. Gaytan, F. Medina, H. Lopez, E. Martinez, B.I. MacHado, D.H. Hernandez, L. Martinez, M.I. Lopez, R.B. Wicker, J. Bracke, Next-generation biomedical implants using additive manufacturing of complex cellular and functional mesh arrays, *Philos. Trans. R. Soc. A Math. Phys. Eng. Sci.* 368 (2010) 1999–2032.

[65]   G. Bisio, G. Rubatto, Sondhauss and Rijke oscillations - Thermodynamic analysis, possible applications and analogies, *Energy*. 24 (1999) 117–131.

[66]   J.W.S. Rayleigh, The Theory of Sound, Vol. II, 1896.

[67]   N. Rott, Damped and thermally driven acoustic oscillations in wide and narrow tubes, *Zeitschrift Für Angew. Math. Und Phys. ZAMP.* 20 (1969) 230–243.

[68]   J. Wheatley, T. Hofler, G.W. Swift, A. Migliori, Understanding some simple phenomena in thermoacoustics with applications to acoustical heat engines, *Am. J. Phys.* 53 (2005) 147–162.

[69]   G.W. Swift, Acoustic power, in: Thermoacoustics A Unifying Perspect. *Some Engines Refrig*., 2002: pp. 105–116.

[70]   G.W. Swift, Thermoacoustics: A Unifying perspective for some engines and refrigerators: Second edition, 2017.

[71]   Z. Huang, S.J. Cho, D. Jiang, S. Tan, Surface nitridation of Al2O3 based composite by N2-HIP post-treatment, *J. Mater. Sci.* 34 (1999)2023–2027.

[72]   M. Udyavar, D.. Young, Precipitate morphologies and growth kinetics in the internal carburisation and nitridation of Fe–Ni–Cr alloys, *Corros. Sci.* 42 (2000) 861–883.

[73]   R. Ivanov, Chemical Vapour Deposition of Graphene Coating onto Ceramic Nanofibers Substrates and Applications Thereof, Supervisor: Irina Hussainova, Tallinn University of Technology, 2017

[74]   C. Zhong, T. Biermann, A. Gasser, R. Poprawe, Experimental study of effects of main process parameters on porosity, track geometry, deposition rate, and powder efficiency for high deposition rate laser metal deposition, *J. Laser Appl*. 27 (2015) 042003.

[75]   L.E. Murr, S.M. Gaytan, A. Ceylan, E. Martinez, J.L. Martinez, D.H. Hernandez, B.I. Machado, D.A. Ramirez, F. Medina, S. Collins, Characterization of titanium aluminide alloy components fabricated by additive manufacturing using electron beam melting, *Acta Mater.* 58 (2010) 1887–1894.

[76]   P.C. Van Wiggen, H.C.F. Rozendaal, E.J. Mittemeijer, The nitriding behaviour of iron-chromium-carbon alloys, *J. Mater. Sci*. 20 (1985) 4561–4582.

[77]   S.J. Rothman, L.J. Nowicki, G.E. Murch, Self-diffusion in austenitic Fe-Cr-Ni alloys, *J. Phys. F Met. Phys.* 10 (1980) 383–398.

[78]   B. Wierzba, Competition between Kirkendall and Frenkel effects during multicomponent interdiffusion process, *Phys. A Stat. Mech. Its Appl*. 403 (2014) 29–34.

[79]   X.-M. He, N. Baker, B.A. Kehler, K.C. Walter, M. Nastasi, Y. Nakamura, Structure, hardness, and tribological properties of reactive magnetron sputtered chromium nitride films, *J. Vac. Sci. Technol.* A Vacuum, Surfaces, Film. 18 (2000) 30.

[80]   Y. Li, Y. Gao, B. Xiao, T. Min, Y. Yang, S. Ma, D. Yi, The electronic, mechanical properties and theoretical hardness of chromium carbides by first-principles calculations, *J. Alloys Compd.* 509 (2011) 5242–5249.

[81]   L.J. Gibson, M.F. Ashby, The Mechanics of Three-Dimensional Cellular Materials, *Proc. R. Soc. A Math. Phys. Eng. Sci*. 382 (1982) 43–59.

[82]   J.R. Davis, Surface Engineering for Corrosion and Wear, 2001.

[83]   M.E. Bahrololoom, R. Sani, The influence of pulse plating parameters on the hardness and wear resistance of nickel-alumina composite coatings, *Surf. Coatings Technol*. 192 (2005) 154–163.

[84]   J.E. Zorzi, C.A. Perottoni, J.A.H. Da Jornada, Hardness and wear resistance of B4C ceramics prepared with several additives, *Mater. Lett*. 59 (2005) 2932–2935.

[85]   H. Sawano, S. Warisawa, S. Ishihara, Study on long life of artificial joints by investigating optimal sliding surface geometry for improvement in wear resistance, *Precis. Eng.* 33 (2009) 492–498.

[86]   D.R. Milner, G.W. Rowe, Fundamentals of Solid-Phase Welding, *Metall. Rev.* 7 (2014) 433–480.

[87]   Y. Holovenko, L. Kollo, M. Saarna, R. Rahmani, T. Soloviova, M. Antonov, K.G. Prashanth, S. Cygan, R. Veinthal, Hard metal - titanium interppenetrating phase composites obtained by selective laser melting and spark plasma sintering, in: *11th Int. Conf. Sci. Hard Mater*., Khao Lak, Thailand, 2019: pp. 159–161.

[88]   R.M. Keolian, G.W. Swift, Pin stack array for thermoacoustic energy conversion, *J. Acoust. Soc. Am*. 99 (2005) 1818.

[89]   J.F. Shackelford, W. Alexander, Materials Science Engineering HandBook, 2001.

[90]   V. Moraes, H. Riedl, R. Rachbauer, S. Kolozsvári, M. Ikeda, L. Prochaska, S. Paschen, P.H. Mayrhofer, Thermal conductivity and mechanical properties of AlN-based thin films, *J. Appl. Phys.* 119 (2016).

[91]   G. V. Samsonov, I. V. Bogomol, S.N. L'vov, M.I. Lesnaya, Thermal conductivity of cermets containing titanium carbide, *Sov. Powder Metall. Met. Ceram*. 11 (1972) 910–912.

[92]   M. Perier-Muzet, J.P. Bedecarrats, P. Stouffs, J. Castaing-Lasvignottes, Design and dynamic behaviour of a cold storage system combined with a solar powered thermoacoustic refrigerator, *Appl. Therm. Eng.* 68 (2014) 115–124.

Acknowledgements

I wish to express my special thanks to my supervisors Professor Renno Veinthal and Senior Research Scientist Lauri Kollo for their continuous support, guidance and encouragement, which made this work possible.

I would like to express my very great appreciation to Dr. Maksim Antonov and Dr. Fabio Auriemma for their research cooperation in the framework of this research work and providing valuable and constructive suggestions.

As well, I wish to acknowledge Prof. Frank Brückner and Dr. Elena Lopez for providing me an opportunity to conduct part of my research at Fraunhofer Institute for Material and Beam Technology IWS in Dresden. I am very grateful to Franz Marquardt and Mirko Riede for supervising me during my stay at Fraunhofer IWS. Also, I would like to address special thanks to Knoll Mathias, Christoph Wilsnack and Christian Grunert for their help during experiments conducted at Fraunhofer IWS.

I sincerely thank Hans Vallner, TalTech engineer, for his continuous effort towards solving technical issues related to equipment.

I am grateful to Marek Jõeleht, Roman Ivanov, Tatevik Minasyan, Le Liu, Sofia Aydinyan, Meelis Pohlak, Irina Hussainova, Ramin Rahmaniahranjani, Dmitrii Goljandin, Tetiana Soloviova, and Sławomir Cygan for fruitful common work.

I am also deeply grateful to every teacher at TalTech and the staff of Tallinn University of Technology and Fraunhofer IWS for their shared experience, fruitful and always enjoyable working atmosphere.

My special thanks are expressed to Märt Kolnes and Mart Kolnes for speaking Estonian patiently with me, which provided me some language practice.

Many thanks to Marek Tarraste, Kaspar Kallipp, Fjodor Sergejev and Priit Kulu for valuable advices, support and assistance during my study. I am grateful to prof. Prashanth Konda Gokuldoss and Devarani Konda Prashanth for help in working on this thesis.

Finally, I would like to thank my family and friends for their everyday support and encouragement.

Abstract

3D Printed Metal and Metal-Ceramic Cellular Lattice Structures for Wear and Thermoacoustic Applications

Nature has created a large number of structures that are successfully used by a variety of living organisms which exist in specific environmental conditions. Wooden materials, bones in the human body or corals in the ocean are shining examples of the natural structures with extremely complex geometry. For many years, attempts to reproduce such structures in artificially fabricated materials failed due to technological limits. Only with the development of additive manufacturing (AM) technologies, it has become possible to produce complex geometrical shapes efficiently. It has opened up a new niche in the research and development for designing, manufacturing, and application of nature-inspired materials. One of the artificially fabricated materials that has gained an increased research interest during recent years is cellular lattice structures. These consist of a single unit cell propagated in three dimensions. A resulting structure is a combination of a monolithic material and empty space.

Nowadays cellular lattice structures have found several applications. For instance, they are used for weight reduction of a part using topology optimization for specific load conditions. Clear benefits using lattice structures have been found in aerospace and engineering. Also, in terms of product life cycle there is a high potential for decreased raw material consumption due to a nearly waste-free production. Medical implants with cellular lattice structures provide precise control of a number of pores, their geometry and final mechanical properties, which allows obtaining the value of the elastic modulus similar to that of a bone tissue. The tissue can grow inside the lattice, which provides sufficient natural bonding and healing acceleration. An additional advantage is a possibility of manufacturing the specifically customized implant for a particular patient during a relatively short time period. Also, a growing field for cellular lattice structures is seen as reinforcing frameworks in the manufacturing of so-called interpenetrating phase composites.

The present study is concentrated on the development of technological procedures and disclosing of new potential application areas of metal and metal-ceramic cellular lattice structures. For the first time, cellular lattice structures were applied for manipulating the tribological characteristics of the surface and self-cleaning ability of the structures surface was shown. Less damage to the contact surfaces was found. This was driven by efficient removal of the wear fragments from the surfaces into the empty internal volume of the lattice that decreased the size of the wear fragments. In addition, the obtained result exhibited five times lower COF than that observed for the reference sample.

The use of metal and metal-ceramic cellular lattice structures as stacks for a thermoacoustic heat engine (TAE) was proposed. TAE is a device that partially converts low-grade thermal energy into acoustic waves with high levels of sound pressure. The energy of acoustic waves generated in TAEs can be transformed into mechanical energy or electric energy. Lattice structures used as stacks in TAE were found to be much more effective compared to regular plate stacks. A thermal conductivity of stack material plays a significant role in thermoacoustic behavior. Ceramic stacks with low thermal conductivity values are known to be more efficient. However, the manufacturing of ceramics and metal-ceramics via direct additive manufacturing is a challenging task due to high heating and cooling rates that cause crack formation.

In order to overcome this problem, a two-step approach of fabrication of metal-ceramic lattice structures was proposed in the present study. Nitriding and carburizing applied as post-processing procedures to as printed metallic lattices increase strength and hardness due to the formation of nitrides and carbides respectively. Microhardness values for nitrided lattices were 605 HV0.3 and for carburized lattices - 576 HV0.3. Vickers hardness of reference, virgin AISI 316L was measured at 210 HV0.3. Compressive yield strength of carburized lattices increases in average from 21% to 65% depending on the lattice density. The elastic modulus increases in average in the range from 16 to 46%. Nitrided lattices exhibited 30% higher acoustic pressure than metal ones.

In this thesis, the following aspects are addressed and solved:

- Parametric study of cellular lattice structures obtained by pulsed laser scanning strategy for powder bed and powder feed AM processes was conducted.
- Metal-ceramic cellular lattice structures were produced by direct and indirect approach. A two-step route that combines 3D printing of the lattice from metal, following with carburizing or nitriding, was introduced.
- Increase in mechanical properties of cellular lattice structures was achieved after post-processing procedures.
- Tribological performance of the cellular lattice structures was validated.
- Thermoacoustic behavior of lattice stack made from metal and metal-ceramics was evaluated.

Keywords: Cellular lattice structures, additive manufacturing, selective laser melting, directed energy deposition, tribology, wear, thermoacoustic

Lühikokkuvõte
3D prinditud metall- ja metall-keraamilised kärgvõre struktuurid triboloogilistele ja termoakustilistele rakendustele

Loodus on loonud suure arvu struktuure, mida kasutatakse edukalt erinevate elusorganismide poolt spetsiifilistes keskkondades. Puitmaterjalid, luud inimese kehas või korallid ookeanis on märkimisväärsed näited äärmiselt keeruka geomeetriaga looduslikest struktuuridest. Aastaid on püütud selliseid struktuure jäljendada, kuid taoliste materjalide valmistamine on ebaõnnestunud tehnoloogiliste piirangute tõttu. Lisandustehnoloogia (teisti 3D-printimine) on siinkohal meetod, mis võimaldab esmakordselt efektiivselt valmistada keerulisi geomeetrilisi kujundeid. See on avanud uue niši teadusarenduse valdkonnas, mille eesmärgiks on kujundada, toota ja rakendada loodusest inspireeritud materjale. Üheks kunstlikult valmistatava materjali näiteks, mis on viimastel aastatel populaarseks saanud, on ühikrakuline võrestruktuur. See koosneb ühikrakust, mida korratakse kolmes mõõtmes.

Praeguseks on ühikrakulised võrestruktuurid leidnud mitmeid rakendusi. Näiteks kasutatakse võrestruktuure detaili kaalu vähendamise eesmärgil vastavalt topoloogia optimeerimisele antud koormustingimustel. Märkimisväärset kasu on võrestruktuurid leidnud nii lennunduses kui ka masinaehituses. Arvestades toodete elutsüklit väheneb oluliselt toormaterjali kulu tänu lisandustehnoloogia sisuliselt jäägivabale tootmisele. Võrestruktuuridega meditsiinilised implantaadid võimaldavad täpselt kontrollida toote poorsust, geomeetriat ning mehaanilisi omadusi saamaks luudele sarnast elastsusmoodulit. Kude saab kasvada võre sisse andes vajaliku sidususe omakorda kiirendades paranemise aega. Lisaväärtusena on võimalik valmistada spetsiifiliselt kohandatud implantaate antud patsiendile suhteliselt lühikese ajaperioodi jooksul. Lisaks on ühikraksete võrestruktuuride uurimisel kasvavaks valdkonnaks võrede kasutamine armeeriva võrgustikuna nn põimfaasidega komposiitides.

Käesolev uurimustöö keskendub metalsete ja metall-keraamiliste ühikraksete võrestruktuuride valmistamisele tehnoloogiliste protseduuride arendamisel ning pakub välja nende võimalikud rakendusvaldkonnad. Esmakordselt on katsetatud ühikrakseid võrestruktuure manipuleerimaks pinna triboloogilisi karakteristikuid ning näidatud pinnastruktuuride isepuhastusvõimekust. Täheldati vähendatud kahju kontaktpinnale, mis on tingitud efektiivsest kulumisfragmentide eemaldamisest võre vahele. Lisaks näitasid katsetulemused viis korda madalamat hõõrdekoefitsenti võrreldes algse näidiskatsekehaga.

Metalseid ja metal-keraamilisi ühikrakseid võrestruktuuride pakutavaks kasutusvaldkonnaks on termoakustilises soojusmootori (TAE) akustiline plaadielement. TAE on seade, mis osaliselt konverteerib madalatasemelise soojusenergia kõrge helisurvega akustilisteks laineteks. Antud lainete energiat saab muundada mehaaniliseks või elektriliseks energiaks. Võrestruktuuridega akustilised plaadielementide efektiivsus näitas oluliselt paremaid tulemusi võrreldes seni kasutusel olevatel plaatidega. Termoakustiline käitumine sõltub suurel määral plaatide materjalide soojusjuhtivusest ning seetõttu sobivad sinna keraamilised materjalid tänu oma madalale soojusjuhtivusele. Lisandustehnoloogiaga on keraamilisi ja metall-keraamilisi materjale keeruline valmistada, sest tänu suurtele protsessi jahtumiskiirustele tekivad materjali praod. Selle probleemi vältimiseks kasutati antud uurimustöös kaheastmelist

metall-keraamiliste võrestruktuuride valmistamist. Printimisjärgse sammuna katsetati metalliliste võrede nitriitimist ja karbidiseerimist, tõstes võrede tugevust ja kõvadust tänu nitriitide ja karbiidide tekkele. Nitriiditud võrede mikrokõvadus oli 605 HV0.3 ja karbidiseeritud võredel - 576 HV0.3. Referentsmaterjalina kasutatud AISI 316L kõvadus on 210 HV0.3. Karbidiseeritud võre survetugevus suurenes 21% -lt 65% -le sõltuvalt võre suhtelist tihedust. Elastmoodul suurenes 16% kuni 46%. Nitriiditud võred näitasid võrreldes metalliste katsekehadega 30% kõrgemat akustilist survet.

Uurimistöö käigus adresseeriti ja lahendati järgmisi askpekte:

- Parameetriline uurimine ühikraksete võrestruktuuride valmistamiseks pulseeriva laserskanneerimise meetodiga kasutades pulbrisängi ja pulbri pealesulatamise metalliprintimise tehnoloogiaid;

- Metall-keraamilised ühikraksed võrestruktuurid valmistati otsese ja kaudse lisandustehnoloogiaga. Tutvustati kaheastmelist meetodit, kus kombineeriti võrestiku 3D-printimine sellele järgneva nitriitimise või karbidiseerimisega.

- Ühikraksete võrestruktuuride mehaanilisi omadusi tõsteti printimisjärgsete tehnoloogiliste sammudega.

- Valideeriti ühikraksete võrestruktuuride triboloogiline võimekus.

- Hinnati metalliliste ja metall-keraamiliste termoakustiliste plaadielementide käitumist.

Märksõnad: Ühikraksed võrestruktuurid, lisandustehnoloogia, selektiivne lasersulatus, otsese energiaga pealesadestus, triboloogia, kulumine, termoakustika

Appendix

Publication I
Holovenko, Y.; Kollo, L.; Jõeleht, M.; Pohlak, M.; Veinthal, R., Effect of Hot Isostatic Pressing on Cellular Lattice Structures Obtained by Selective Laser Melting. *World PM2016 proceedings: World PM2016 Congress & Exhibition, Hamburg, Germany, 9-13 October 2016. European Powder Metallurgy Association*, (2016), USB.

Effect of Hot Isostatic Pressing on Cellular Lattice Structures Obtained by Selective Laser Melting

Yaroslav Holovenko (Tallinn University of Technology, Ehitajate tee 5, Estonia) yaholo@ttu.ee; Lauri Kollo (Tallinn University of Technology, Ehitajate tee 5, Estonia) lauri.kollo@ttu.ee; Marek Jõeleht (Tallinn University of Technology, Ehitajate tee 5, Estonia) marek.joeleht@ttu.ee; Meelis Pohlak (Tallinn University of Technology, Ehitajate tee 5, Estonia) meelis.pohlak@ttu.ee; Renno Veinthal (Tallinn University of Technology, Ehitajate tee 5, Estonia) renno.veinthal@ttu.ee

Abstract

Cellular lattice structures have attracted a lot of attention during last years, for allowing design freedom beyond the capacity of solid materials. Selective Laser Melting (SLM) is one of the techniques for obtaining mesoscale lattices, for example from stainless steel with final bulk density less than water. The present study focuses on the SLM process parameters and on Hot Isostatic Pressing (HIP) under nitrogen atmosphere as a post-processing procedures and influence of these on mechanical properties. Surface quality and diameter of the struts were influenced by varying laser current and exposure time. Nitrogen was used as protective atmosphere during the SLM process. Mechanical properties of lattice structure were shown to depend on both, processing conditions and on post-processing.

1 Introduction

Selective Laser Melting (SLM) is an additive manufacturing technique enabling to produce intricate shapes directly from metal powder. Great potential lays in the ability of SLM to construct internal architectures.

Cellular materials produced by SLM have attracted a lot of attention due to their high strength to mass ratio [1], high energy absorption, and thermal and acoustic isolation characteristics [2].

Materials with periodical lattice topology have number of advantages over other traditional foams type materials [2, 3]. Due to this in recent years a number of investigations were performed [4-10]. Lattices made of stainless steel [4, 5, 6], aluminum and titanium alloys [7, 10], and even copper [9] have been reported. New approaches to lattices generation for additive manufacturing were developed [11, 12]. However, influence of post processing on lattice materials properties has not been widely investigated. Different post processing procedures could affect the structure, chemical composition, surface properties etc., which could improve mechanical properties of cellular lattices. Chunze Yan et al. [4] investigated gyroid lattice structures produced from stainless steel 316L and proposed sand blasting as a post processing operation to remove bonded particles from lattice. Aref Yadollahi et al. reported the effect of homogenizing heat treatment at 1150 $^{\circ}$C [5] on microstructure and mechanical properties of SLM stainless steel 316L. Heat treatment increased grain size which resulted in lower strength and higher ductility.

In the present study the influence of SLM process parameters and post-processing procedures on structural features and mechanical properties of lattice structures were investigated. First of all, the relation between laser current (LC), which determines laser power, and laser exposure time (ET) combinations and resulted strut diameter were determined. Post processing was performed with an aim to improve mechanical performance of cellular lattices and change surface properties of struts.

2 Experimental

2.1 SLM process and post processing

Stainless steel AISI 316L powder with particle size 10-45 µm was used as a starting material for producing lattice structures by selective laser melting process.

Selective laser melting (SLM) was carried out using a Realizer SLM50 machine. The thickness of one layer was 25 µm and 50 µm, laser current was varied from 2500 mA (60 W) to 5000 mA (120W), exposure time was varied from 250 to 1100 ms. Nitrogen was used as a protective atmosphere during the process with oxygen level less than 0.2%. Hot isostatic pressing (HIP) was performed at 1150 $^{\circ}$C under pressure of 100 MPa in nitrogen atmospheres.

2.2 Lattice generation

Lattices were generated using RDesigner software. Final lattice structure consists of connected vectors with zero thickness (Fig. 1 a) so each layer of model in cross section consist of single points (Fig. 1 b) which determine places of future laser influence. Combination of laser power and exposure time determines final strut diameters.

Two types of diamond shape unit cell were used. First one (Fig. 2 a), was used for strut diameter measurements. This unit cell has vertical struts which simplifies the measurement process. In this case specimen size was 5x5x5 mm and unit cell size 1 mm. For compressive testing and post processing investigations diamond unit cell (Fig. 2 b) was used.
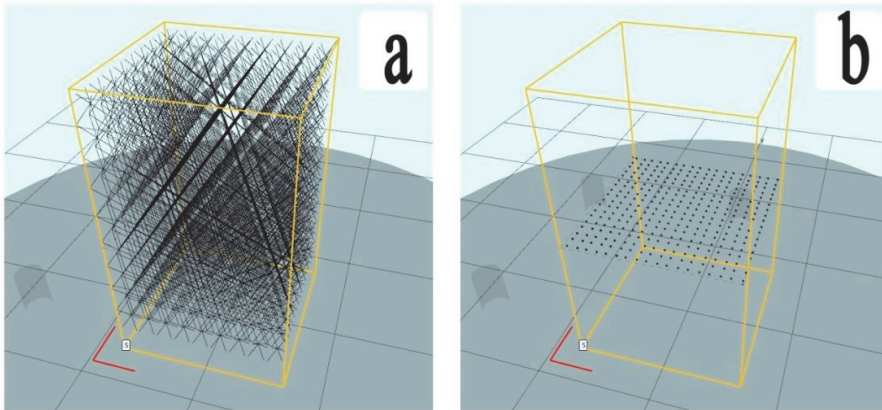
Figure 1 – General view (a) and cross section (b) of generated lattice
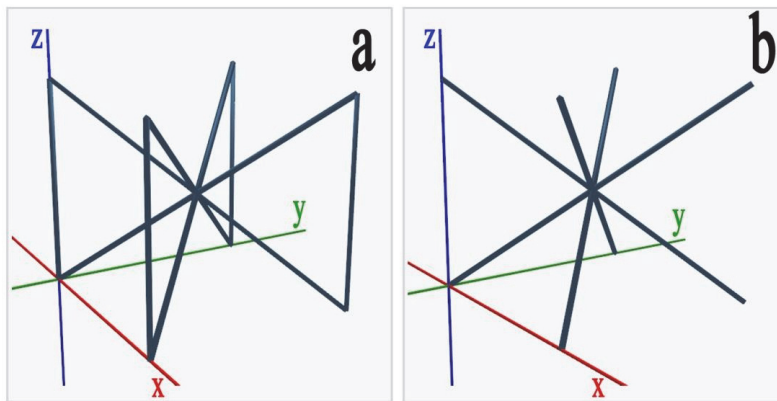
Figure 2 – Unit cells for lattice generation with (a) and without (b) vertical struts

Samples with dimensions of 14.1 mm × 14.1 mm × 21 mm were produced for mechanical testing and post processing procedures. Unit cell size was varied from 1.2 mm to 2.0 mm, and elongation along z axis was 1, 1.5 and 2 times relative to initial unit cell size.

2.3 Measurements

Structural investigations of the lattice structures were performed by using Scanning Electron Microscope (SEM) Hitachi TM1000. Compressive strength was measured at loading rate 1 mm/min at room temperature, using Instron 8516 servohydraulic testing system.

3 Results and discussion

Lattice structures with diamond unit cells and size of 1 mm were manufactured for measuring strut dimensions.

Figure 3 represents SEM micrographs of lattice structure obtained at laser current 2800 mA and exposure time 250 μs and 2000 μs respectively. During measurements two types of struts were found. First one is represented on figure 3 a, when a lot of strut's surface is covered by bonded particles. At low exposure time (less than 600 μs) large amount of bonded particles are connected to struts causing high surface roughness. Such phenomenon can be explained as follows. At low exposure time, particles located on the external border of zone of thermal influence cannot fully melt, and therefore are remained as partially melted bonded particles. Increasing the exposure time homogenizes the temperature in the heat affected zone and amount of liquid phase increases. Second surface type (Fig. 3 b) is representative to samples obtained at exposure time 600 μs and higher. With increasing of ET and LC values, strut diameters are growing. External boundary, at the same time is smoother and bonded particles cover smaller area.
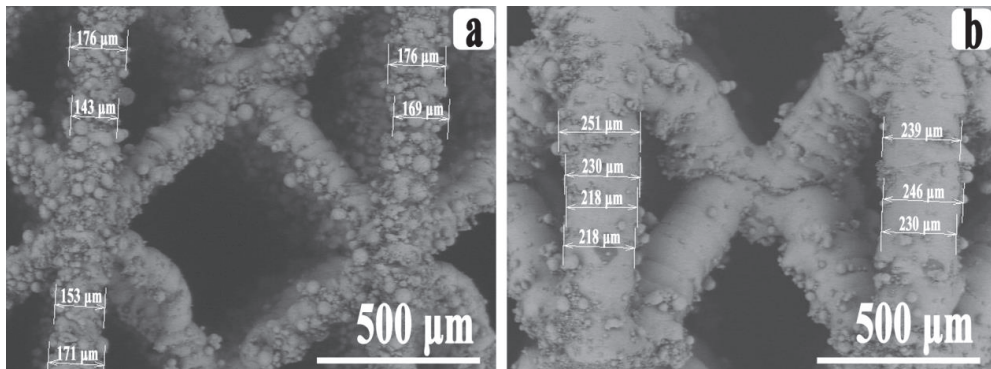
Figure 3 – Bonded particles on struts at LC = 2800 mA, and different exposure time, ET = 250 μs (a) and ET = 2000 μs (b)

The results show that for exposure time less than 400 μs, average strut dimensions are similar and stay in range from 155 μm to 177 μm (Fig. 4). Up to laser current 4000 mA and exposure time 400μs bonded particles covered almost whole strut surface which made the measuring process more difficult and influenced on dimension's distribution along the strut.
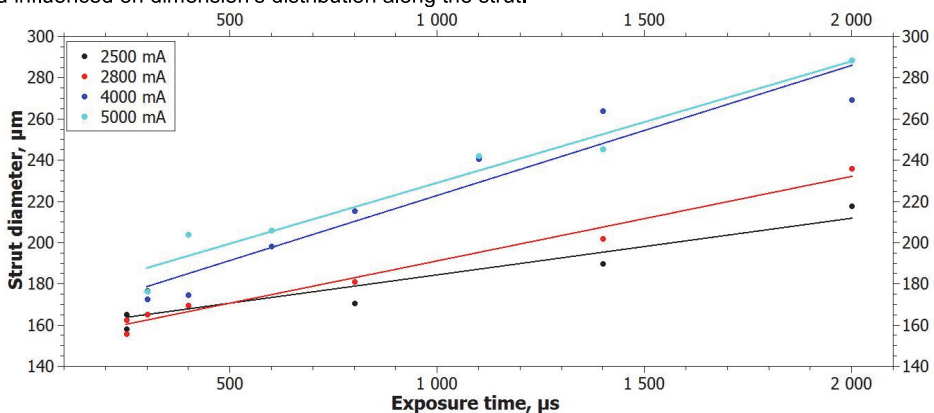
Figure 4 – Dependence of strut diameter on process parameters

To produce diamond lattice without vertical struts for mechanical properties testing and post-processing procedures, combination of laser current 4000 mA and exposure time 900 μs was used. Two sets of samples (table 1) were produced with layer thickness 25 μm and 50 μm respectively. Elongation along z axis was 1x, 1.5x and 2x, where x is initial unit cell size. Figure 5 shows micrograph of diamond lattices obtained with 25 μm and 50 μm layer thickness.
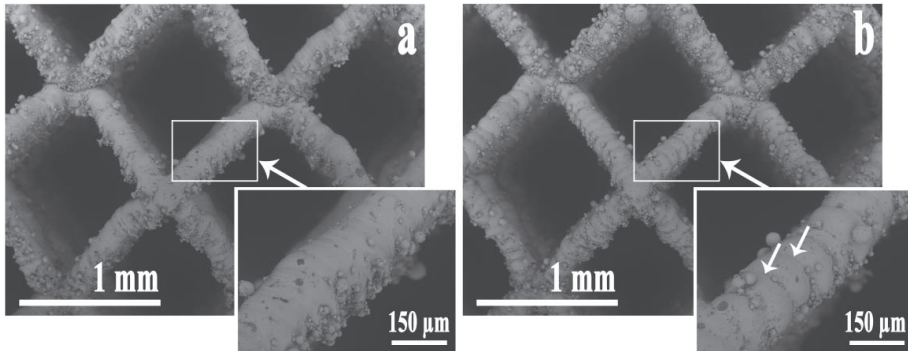
Figure 5 – Micrograph of diamond lattices obtained at LC = 4000 mA and ET = 900 μs with 25 μm (a) and 50 μm (b) layer thickness

Table 1 – Lattices for mechanical testing characteristics

Layer thickness 25 μm				Layer thickness 50 μm			
	Unit cell size				Unit cell size		
Z axis elongation	1.2	1.6	2.0	Z axis elongation	1.2	1.6	2.0
1 x	1	2	3	1 x	1	2	3
1.5x	4	5	6	1.5x	4	5	6
2 x	7	8	9	2 x	7	8	9

As visible from the micrograph in Figure 5a, at 25 μm layer thickness, struts are more uniform and smoother. Using 50 μm layer thickness (Fig. 5 b) melt pool boundary (shown with arrows) on each layer is clearly observed. The reason is schematically explained on figure 6. To simplify the explanation influence of gravity and surface tension force on scheme were neglected. Displacement of laser influence point compared to previous is smaller when smaller layer thickness is used. Moreover, melt pool depth stays the same at the other equal conditions (LC and ET are same) despite changing in layer thickness. Therefore melt pool is more overlapping with remelting of the previous layer at smaller layer thickness (Fig. 6 a). The printing parameters define shape of diagonal strut surface and bonding strength between two neighboring layers.
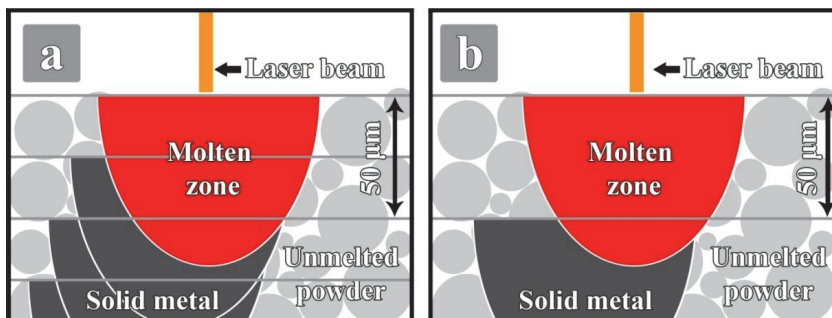
Figure 6 – Schematic explanation of difference in strut shape at 25 μm (a) and 50 μm (b) layer thickness

Density of samples obtained at 25 μm and 50 μm layer thickness was almost the same due to same amount of melted material during the SLM process. Average difference in densities was 2.3 % and for each sample was calculated as follows:

$$\Delta_{dens} = \frac{\gamma_{50} - \gamma_{25}}{\gamma_{25}} \cdot 100\%$$

where γ_{25} and γ_{50} – total density of lattice with 25 µm and 50 µm layer thickness respectively.

HIPing was performed on set of samples with 50 µm layer thickness. Increase of weight for HIPed samples was observed, ranging between 4.71 - 4.98 % depending on the sample Specimens after HIPing become brittle (Fig. 7 a) and got changes in microstructure, which also could be confirmed with existence of nitrides in the material of lattice.
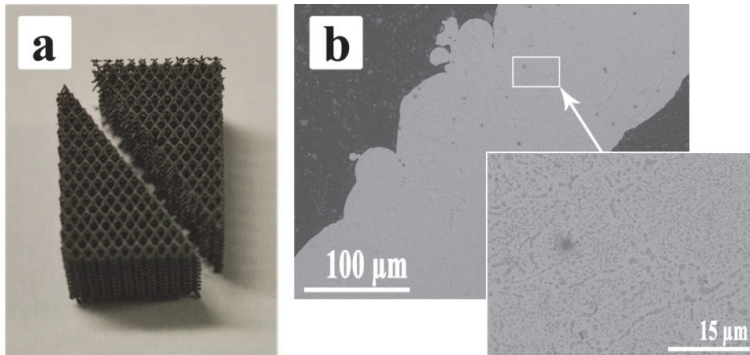

Figure 7 – General view of fractured HIPed lattice (a) and its microstructure (b)

As pointed in the literature data [13] rising of the process temperature causes higher saturation velocity. Due to relatively small strut diameter, high temperature and high pressure, nitrogen diffuses into strut surface and creates a nitride layer, which is homogeneous throughout the lattice volume (Fig 7 b). This still need to be confirmed by XRD studies. In consequence of formation of nitrides lattices lost their plasticity, and specimens showed brittle failure during compressive test. Figure 8 represents compressive yield strength dependence from unit cell size. Compressive yield strength of lattices obtained at 50 µm layer was lower than at 25 µm, especially in case of equal in all directions unit cell size (Fig. 8 a).

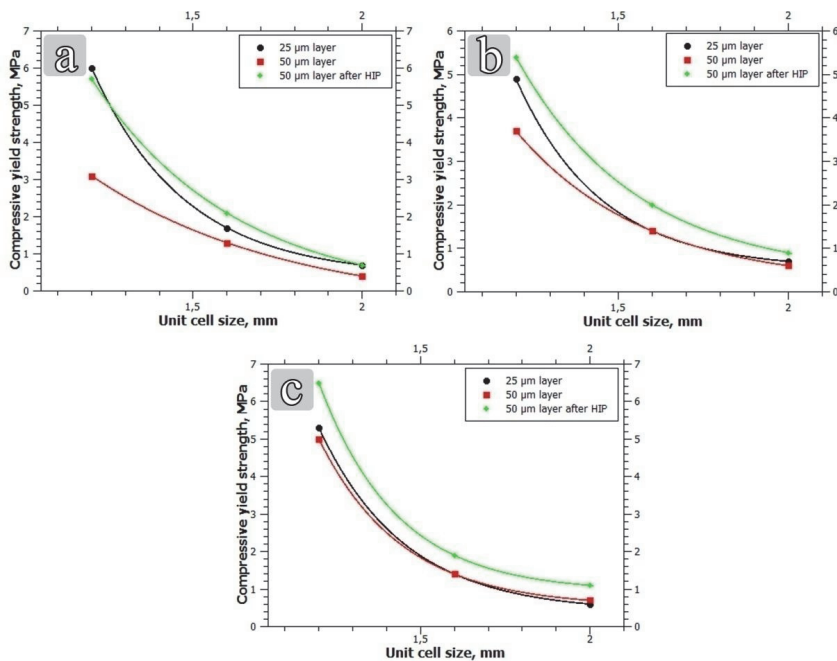Figure 8 – Dependence of compressive yield strength from unit cell size with unit cell elongation along z axis 1x (a), 1.5x (b) and 2x (c)

As visible from Figure 8, with elongation of unit cell along z axis difference in yield strength values between lattices with 25 µm and 50 µm layer thickness became minor. The reason is decreased displacement of laser influence point on each next layer, which caused stronger connection between two neighboring melt pools (schematically shown on Fig. 6) despite of increasing layer thickness. Therefore angle of struts is an important parameter which defines overlapping area of melt pools with increasing layer thickness. The main reason to increase the layer thickness lays in need to make production process faster. HIPing in nitrogen increased strength of lattice due to nitriding of the struts.

4 Conclusions

Mechanical properties of lattice structure obtained at different process parameters by SLM have been investigated. According to experimental results in this work following conclusions can be made:
- Struts produced with low ET (less than 600 microseconds) have large amount of bonded particles on the surface. Increasing the exposure time (ET at least 600 microseconds) decreases the number of bonded particles.
- Melt pools remelting with the previous layer increases the bonding strength between two neighboring layers. Higher influence of the layer thickness is seen for struts under lower angles and for smaller cell sizes.
- Due to relatively small strut diameter, high temperature and high pressure, nitrogen diffuses into strut surface and creates nitrides, which are distributed throughout the lattice volume. Mass changing after HIP process could be evidence of chemical transformation. In consequence of nitrides formation lattices lost their plasticity.
- Phase composition of nitrided lattices, influence of HIPing parameters on nitride layer thickness, on structure and properties of lattice are objective to further investigations

Reference

1. Yang, Li. "Experimental assisted design development for a 3D reticulate octahedral cellular structure using additive manufacturing." Review.
2. Chu, Jane, et al. "A comparison of synthesis methods for cellular structures with application to additive manufacturing." *Rapid Prototyping Journal* 16.4 (2010): 275-283.
3. Bele, E., B. A. Bouwhuis, and G. D. Hibbard. "Work hardening as a strengthening mechanism in periodic cellular materials." *Materials Science and Engineering: A* 489.1 (2008): 29-37.
4. Yan, Chunze, et al. "Evaluations of cellular lattice structures manufactured using selective laser melting." *International Journal of Machine Tools and Manufacture* 62 (2012): 32-38.
5. Yadollahi, Aref, et al. "Effects of process time interval and heat treatment on the mechanical and microstructural properties of direct laser deposited 316L stainless steel." *Materials Science and Engineering: A* 644 (2015): 171-183.
6. McKown, S., et al. "The quasi-static and blast loading response of lattice structures." *International Journal of Impact Engineering* 35.8 (2008): 795-810.
7. Yan, Chunze, et al. "Microstructure and mechanical properties of aluminium alloy cellular lattice structures manufactured by direct metal laser sintering." *Materials Science and Engineering: A* 628 (2015): 238-246.
8. Ramirez, D. A., et al. "Open-cellular copper structures fabricated by additive manufacturing using electron beam melting." *Materials Science and Engineering: A* 528.16 (2011): 5379-5386.
9. Ramirez, D. A., et al. "Open-cellular copper structures fabricated by additive manufacturing using electron beam melting." *Materials Science and Engineering: A* 528.16 (2011): 5379-5386.
10. Gorny, B., et al. "In situ characterization of the deformation and failure behavior of non-stochastic porous structures processed by selective laser melting." *Materials Science and Engineering: A* 528.27 (2011): 7962-7967.
11. McMillan, Matthew, et al. "Programmatic Lattice Generation for Additive Manufacture." *Procedia Technology* 20 (2015): 178-184.
12. Hao, Liang, and D. Raymond. "Design and additive manufacturing of cellular lattice structures." *The International Conference on Advanced Research in Virtual and Rapid Prototyping (VRAP). Taylor & Francis Group, Leiria*. 2011.
13. Gulyaev, A. P. "Metallurgy: Textbook for high technical schools." Moscow.: Metallurgy (1986).

Publication II
Holovenko, Y; Kollo, L; Jõeleht, M; Ivanov, R; Soloviova, T; Veinthal, R., Production of metal-ceramic lattice structures by selective laser melting and carburizing or nitriding. *Proceedings of the Estonian Academy of Sciences*, 68 (2), (2019), 131–139.

Production of metal–ceramic lattice structures by selective laser melting and carburizing or nitriding

Yaroslav Holovenko[a*], Lauri Kollo[a], Marek Jõeleht[a], Roman Ivanov[a], Tetiana Soloviova[b], and Renno Veinthal[a]

[a] Department of Mechanical and Industrial Engineering, Tallinn University of Technology, Ehitajate tee 5, 12611 Tallinn, Estonia
[b] Faculty of Physical Engineering, National Technical University of Ukraine "Igor Sikorsky Kyiv Polytechnic Institute", Peremohy Av. 37, 03680 Kyiv, Ukraine

Abstract. Selective Laser Melting (SLM) allows obtaining light-weight cellular lattice structures with complex geometry. However, producing metal–ceramic components, as well as cellular lattice structures, by SLM is limited. The present study focuses on obtaining metal–ceramic lattice structures by a two-step approach: SLM and post-processing. Nitriding and carburizing were applied to stainless steel cellular lattice structures. A set of post-processing parameters is estimated in order to nitridize and carburize metallic cellular lattice structures. Compared to the initial material, post-processed lattices exhibited higher average Vickers hardness values, measured for nitrided and carburized structures at 605 and 576 HV0.3, respectively, while the reference microhardness of steel 316L is 210 HV0.3. The highest average compressive yield strength value for untreated lattice was 60.7 MPa and for carburized lattices, 99.3 MPa.

Key words: selective laser melting, lattice structure, ceramic, nitriding, carburizing.

1. INTRODUCTION

Additive manufacturing enables to produce parts of complex shape directly from metal powder. The unique feature of this technique is the possibility of creating three-dimensional (3D) architected cellular lattice structures with properties determined by the structure and geometry of the object rather than by its composition [1,2].

Advanced ceramics are a group of materials that have high hardness with the temperature and corrosion resistance needed for many engineering applications. Production of ceramics by additive manufacturing has attracted great interest due to difficulties faced in processing complex objects by classical powder metallurgy methods, especially in small batch sizes. Another distinct benefit is the low demand for post-processing, as ceramic materials are hard to machine. Producing ceramic and metal–ceramic shapes or cellular lattice structures has been found difficult to be achieved by direct printing methods [3]. High cooling rates during the process give rise to thermal stresses, and due to the brittle nature of ceramics, tend to cause cracks in end products [4]. Instead of direct 3D printing, ceramic parts are more commonly produced by using indirect methods, where organic binders and ceramic particles are mixed and shaping is performed by polymer printing methods such as fused deposition modelling, selective laser

---

[*] Corresponding author, yaholo@taltech.ee

sintering, or binder jetting. In these cases an additional sintering step is required. Such approach allows producing ceramics with near full density and high mechanical performance [5,6]. Another indirect approach uses the polymer pyrolysis route for obtaining ceramic parts [7]. Eckel et al. [8] reported a successful attempt at obtaining a ceramic cellular lattice structure with fine detail size using the stereolithography process for forming the polymer. Pyrolysis was applied as post-processing in order to form ceramic structures [8]. The limitation of such an approach is the restricted number of ceramics that can be obtained by this route. A similar two-step approach can be applied also to metal lattice structures. A well-known method for creating protective metal–ceramic composite layers on metal surfaces is case hardening, mainly through nitriding [9,10], or carburizing [11]. When such treatments are applied to thin lattice structures, the maximal penetration depth can be higher than the size of the lattice strut diameter. Therefore, it can be assumed that all-directional influence on the strut will lead to changes in the material with a minimal gradient. Post-treatment increases hardness, strength, wear resistance, load carrying capability, and fatigue strength.

The aim of the present study was to introduce and estimate a new processing route for metal–ceramic composite lightweight cellular lattice structures by combining selective laser melting and thermochemical treatment. Metal–ceramic lattices produced by the presented approach may also have an advantage over metallic ones in thermoacoustic applications due to the changed thermal properties of the material.

2. EXPERIMENTAL

2.1. Materials

The cellular lattice structures were produced from atomized AISI 316L powder delivered by Shijiazhuang Daye Metal Powder Factory. The particle size was in the range from 10 to 45 μm. The chemical composition of stainless steel 316L powder is presented in Table 1.

2.2. Lattice generation

Lattices were created using RDesigner software developed by Realizer GmbH. The lattice geometry is represented as a beam model. A modified octet truss unit cell (Fig. 1a) was used in this study. All horizontal elements were removed from the initial octet truss unit cell due to pulsed laser scanning strategy limitation. Samples with the dimensions of 10 mm × 10 mm × 15 mm were produced

Table 1. Chemical composition of AISI 316L

Alloying element	Content, wt%
Fe	Rest
C	<0.03
Cr	16–18.5
Ni	10–14
Mo	2–3
Mn	<2
Si	<1
P	<0.045
S	<0.03

(Fig. 1b). The unit cell size was varied from 1 mm to 1.47 mm. A set of lattice structures was chosen in order to investigate the influence of thermochemical treatment with minor changes in relative density.

2.3. Selective Laser Melting (SLM) process and post-processing

All the printing experiments were performed on a Realizer SLM50 selective laser melting machine. Pulsed laser scanning strategy was employed to obtain lattices. The laser current was kept constant at 4000 mA, which is approximately equal to 100 W laser power. The exposure time (ET) was varied from 400 μs to 1100 μs. During the process nitrogen was used as a protective atmosphere, and the oxygen level was kept at less than 0.2%. Hot isostatic pressing (HIP) and carburizing were used as post-processing procedures. HIP was used in order to perform the nitriding of lattice structures with applying overpressure. HIP was carried out at 1150 °C at 100 MPa under nitrogen. Carburizing was performed in CH_4 flow of 250 ccm under atmospheric pressure at 1000 °C for 20 min, which was followed by dwelling in furnace under vacuum at 1150 °C for 1 hour.

2.4. Measurements and characterizations

Structural investigations of the lattices were performed by using Scanning Electron Microscope (SEM) Hitachi TM1000 and Zeiss Evo MA15. In order to investigate microstructural changes, specimens were embedded inside a polymer matrix, ground, and polished. Compressive strength of the lattice structures was measured at a loading rate of 1 mm/min, using the Instron 8516 servo-hydraulic testing system. X-ray diffraction (XRD) was carried out on a Rigaku Ultima IV machine with a Cu Kα beam and measuring step width of 0.05°. A Buehler Micromet 2001 microhardness tester was used for Vickers hardness measurements with the load of 300 gf.
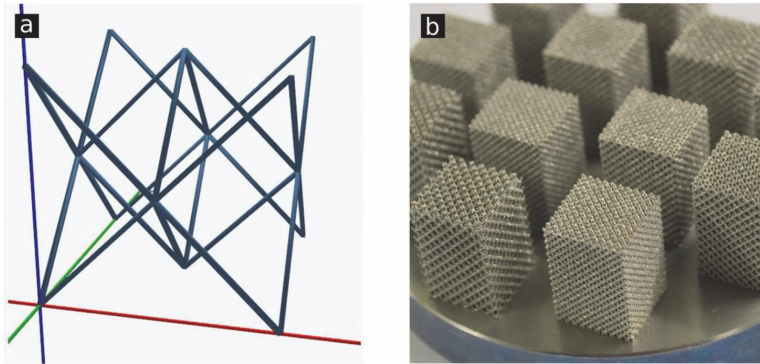
**Fig. 1.** Beam model of the lattice unit cell (a) and image of produced lattice structures (b).

3. RESULTS AND DISCUSSION

3.1. Morphology and relative density of the lattices

The SEM image of the 3D printed lattice structure obtained at the lowest exposure time (ET = 400 µs) clearly shows that a number of bonded particles are connected to the downface side of oblique struts whereas their top surface is relatively smooth (Fig. 2). The highest exposure time (ET = 1100 µs) caused longer existence of the liquid phase and higher thermal influence on the surrounding unmelted powder (Fig. 2b). As a result, the downface surface of lattice struts is covered with a significant number of bonded particles and waves caused by solidified inflows of molten material in overhanging regions. The strut diameter increased with the exposure time.

Due to the presence of an inclination angle, certain phenomena were observed. First of all, some of the molten material overhung the previous solid layer. This molten material had been pulled down by gravity and particles located underneath became connected to the strut surface. A similar phenomenon was observed by Suard et al. [12] and Yan et al. [13]. At the same time, particles located under the oblique strut can be partially melted or sintered due to thermal flux specifics during the SLM process [14].

According to the Gibson–Ashby model, the strength and modulus of the porous cellular lattice structure depend on the ratio of lattice density to bulk material density [15]. In this study, the relative density of the obtained lattice structures varied from 14.85% to 41.14%; these values are related to the lattice densities
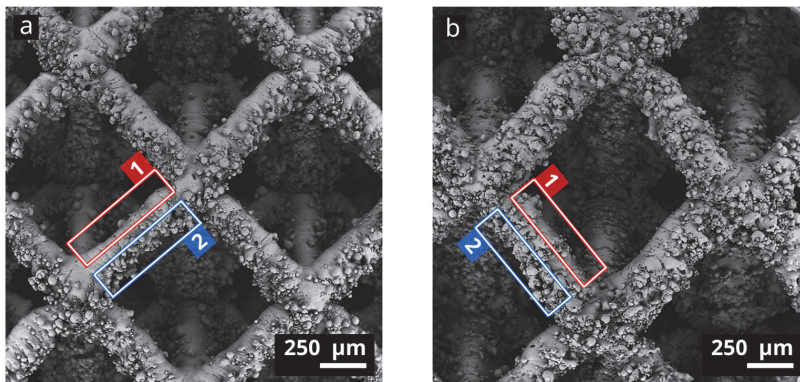
uus-ok

Fig. 2. Octet truss lattice structure obtained at ET 400 µs (a) and at ET 1100 µs (b); 1 – upper side and 2 – downface side of the oblique strut surface.

of 1.19 g/cm^3 and 3.29 g/cm^3, respectively. The smallest relative density values were obtained for lattices with 1.47 mm unit cell size, and the highest for 1 mm unit cell size. Table 2 provides relative densities of lattices.

3.2. Microstructure

Cross-sections specific at different heights of the lattice are illustrated in Fig. 3. The node of the lattice is the place of struts interconnection. Usually locations of nodes correspond to unit cell vertexes. The cross-sections in the places located close to a node are characterized by a larger area compared to the cross-section of a single strut. This leads to local differences in post-processing conditions. However, thermochemical treatment is all-directional and the penetration depth is larger than the element size. The approximate penetration depth of up to 0.6 mm in the case of nitriding [16] and up to 1 mm for carburizing [17] can be achieved under conditions similar to those used in this work. The sizes of the lattice elements were smaller than the mentioned penetration depth, which provides full transformation of the whole lattice volume into the metal–ceramic composite.

Additionally, some geometrical irregularities were present at the bottom of the node area. These are related to bonded particles below the struts. Also, close proximity of laser exposure points leads to material sintering between them. The cross-sections of the lattice nodes after nitriding and carburizing are represented in Fig. 4a

and 4d, respectively. In Fig. 4a, it is visible how individual struts start detaching from the node. In these places crack-like spacing appears.

The main feature of the carburization process in this study was the occurrence of a gas flow, which could theoretically cause the presence of a deposition gradient. In previous works [18,19] the deposition of a graphene layer on the bundle of ceramic nanofibres was observed. In case of nanofibres, gas penetration inside the sample was challenged by the fact that the distance between fibres was around 20–50 nm. The deposition gradient was found to be present for the specimens over 3 cm in length and the gas flow more than 500 ccm. In the case of the lattices, the porosity was much higher, but specimen sizes and gas flow were two times below the reported values. The microstructures of nitrided and carburized lattices were characterized by the absence of any significant gradient in the phase distribution. This shows that the penetration depth during the thermo-chemical treatment was sufficient through the whole cross-section of struts. Several phases were evenly distributed through the cross-section when the initial material was a one-phase alloy.

The microstructure of the nitrided lattice consisted of three phases: matrix (marked as N-1A) and two types of inclusions (marked as N-1B for an average linear size of 0.86 µm and as N-1C for 0.32 µm size (shown in Fig. 4b)). Visual representation of Energy-Dispersive X-ray Spectroscopy (EDS) data is shown in Fig. 4c

Table 2. Relative densities of the lattices

Exposure time [µs]	Relative density [%]			
	Unit cell size [mm]			
	1	1.11	1.26	1.47
600	28.8 ± 0.3	24.8 ± 0.3	19.9 ± 0.2	14.9 ± 0.5
800	34.1 ± 0.4	27.5 ± 0.5	23.3 ± 0.3	15.8 ± 0.6
1100	41.1 ± 0.3	32.6 ± 0.4	24.7 ± 0.4	19.6 ± 0.4
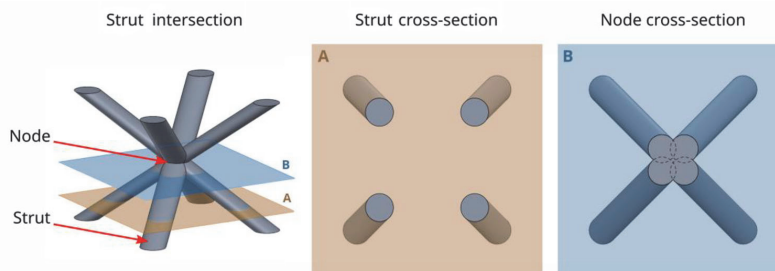
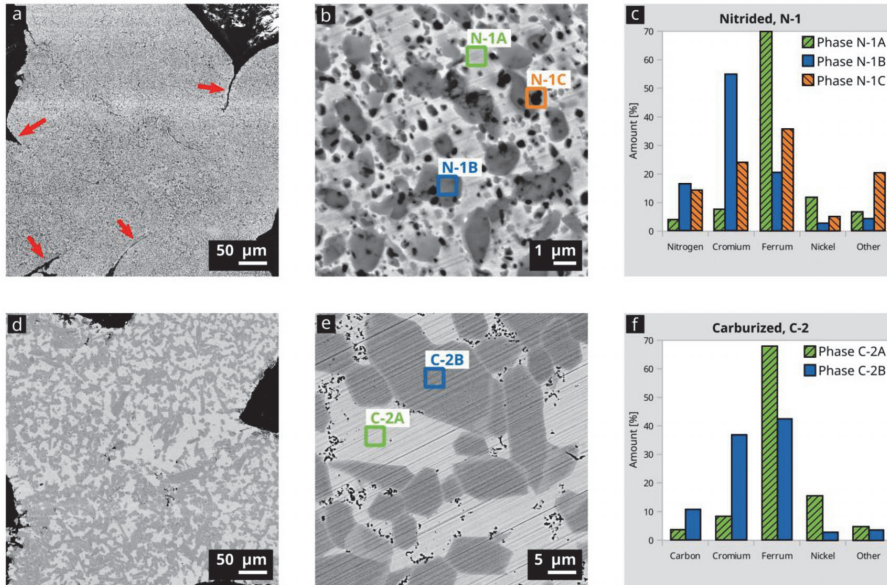**Fig. 3.** Schematic illustration of cross-sections specific to different places of the lattice.

Fig. 4. SEM micrographs and EDS results of nitrided (a, b, c) and carburized (d, e, f) lattices. Arrows point to crack-like spacing.

and 4f. The size of the N-1C phase is always less than 1 µm, resulting in inaccurate EDS analysis since it also includes information about the surrounding phases. The XRD results provide evidence of chromium nitride in the sample as well as iron nitride (Fig. 5a). The XRD patterns of pure 316L powder do not exhibit such additional peaks [20]. Considering also EDS results, it can be concluded that during the HIP process chromium

and iron form nitrides resulting in a multiphase metal–ceramic lattice structure.

The microstructure of the carburized lattice consists of two main phases: C-2A and C-2B (Fig. 4e). Compared to nitrided lattices, the C-2B phase showed significantly larger sizes averaging at 12.3 µm. In combination with XRD results (Fig. 5b), it can be concluded that chromium tended to form carbides. Black dots in the microstructure
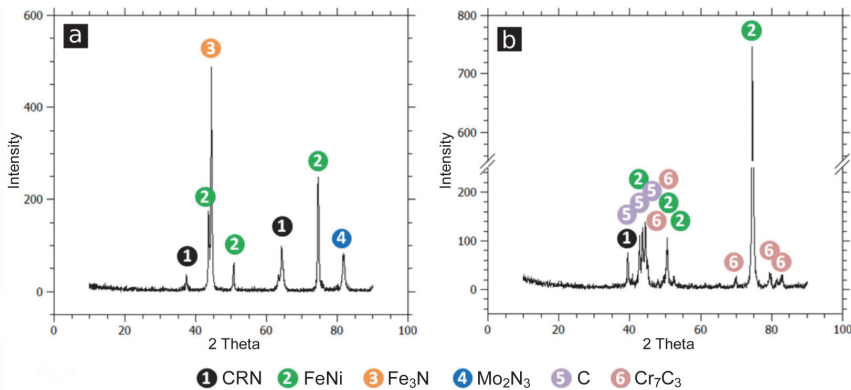
Fig. 5. XRD patterns for nitrided (a) and carburized (b) lattices.

are microscopic voids (Fig. 4e), which are located on the interfacial boundaries. The size of the single pore was less than 1 μm. The main possible reason of the formation of voids is the so-called diffusion porosity or Kirkendall and Frenkel effect [21]. Chromium diffuses faster than iron or nickel [22], it also tends to form carbides first. Vacancies formed by the migration of Cr atoms cannot be fulfilled by atoms of other elements with the same speed. Therefore, pores are forming in such a specific location as the interfacial boundaries. The presence of carbon peaks in Fig. 5b can be attributed to the residual deposited graphite on the surface.

3.3. Microhardness and mechanical properties

The average microhardness of nitrided lattices was 605 HV0.3 and of carburized lattices, 576 HV0.3. Vickers hardness of the bulk SLM processed virgin AISI 316L was measured at 210 HV0.3. These results are in good agreement with the values reported in the literature

[23–25]. Figure 6 shows strength characteristics of lattices. Compressive yield strength tended to grow with relative density (Fig. 6a). The obtained results, in general, correlate with the Gibson–Ashby model [15]. The calculated coefficient of correlation $R = 0.9865$. Nevertheless, it is also clear that experimental data slightly differ from the compressive yield strength estimated by the Gibson–Ashby model. As was concluded in [13], the differences in theoretical and experimentally tested values can be attributed to the residual stress and more complex geometry caused by bonded particles. Nitrided and carburized lattices became brittle and collapsed at some point of testing (Fig. 6c, 6d) while the untreated stainless steel lattices did not collapse at all during the testing up to 50% of deformation when the test stopped due to the programmed limit. The average ultimate fracture strength of carburized and nitrided lattices with relative density in the range of 19.6–24.7% was comparable. However, with increasing relative density values, the difference in strength became more
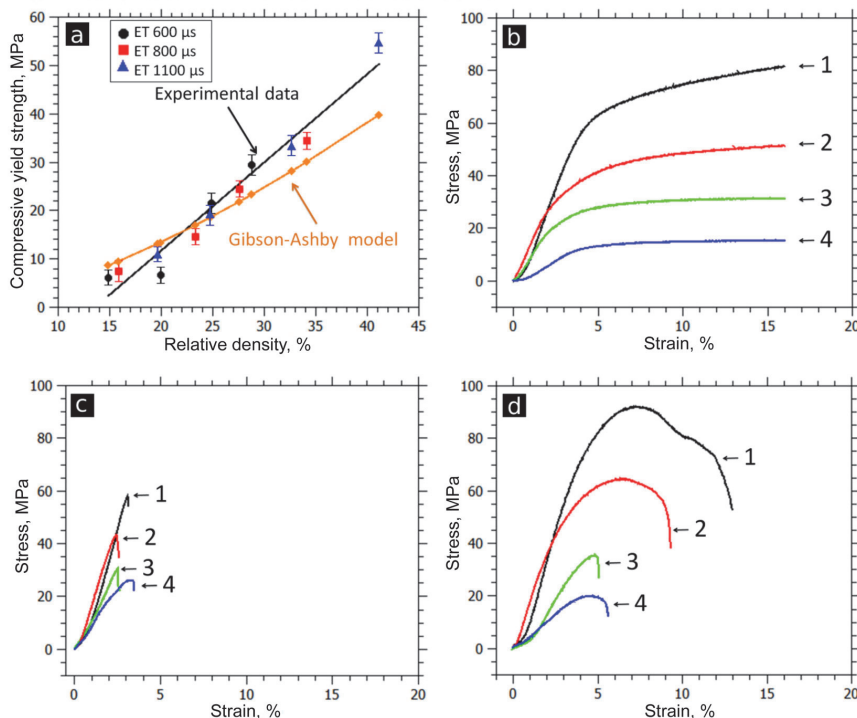
Fig. 6. Measured and calculated according to the Gibson–Ashby model compressive yield strength values of untreated lattices vs relative density (a) and stress–strain curves for untreated (b), nitrided (c), and carburized (d) lattices. Relative densities: 1 – 41.1%, 2 – 32.6%, 3 – 24.7%, 4 – 19.6%.

noticeable. Lattices with relative density of 41.1% showed compressive ultimate strength (fracture stress) of carburized lattices about 1.5 times as high as nitrided lattices. Nitrided lattices exhibited 2–3% deformation in the elastic zone before collapsing without plastic deformation. In the case of carburized lattices, some plastic deformation was observed. Deformation for carburized lattices before critical failure was from about 4.5% to 8% for lattices with the lowest and with the highest relative density, respectively (Fig. 6d). Lower plasticity of nitrided structures is caused by the peculiarities of the structure of the nitrided layer. In general, the nitrided structure may be divided into two sublayers: a compound zone and a nitrogen diffusion zone [10,16], both consisting of the nitrides Fe_3N and Fe_4N phase. The Fe_2-Fe_3N phase (detected by XRD in the current case) is known to be hard but very brittle. Carburized layers usually contain some amount of the metallic phase (ferrite or austenite) in their structure, which provides them a relatively high plasticity.

Table 3 summarizes compressive yield strength, fracture stress, and elastic modulus of untreated lattices as well as nitrided and carburized lattices. Compressive yield strength of carburized lattices increased on average by 10 MPa over the whole range of lattice relative densities. With the increasing of the lattice relative density, the difference between the yield strength and the fracture stress increased. Compressive yield strength values are not available for nitrided lattices because of the absence of the yield point (0.2% offset line did not cross the strain–stress curve). The fracture occurred in the linear elastic region. Elastic modulus increased with density (Table 3). Post-processing tended to increase the elastic modulus.

Further research could be focused on wear properties of such metal–ceramic lattices. Regular metal as printed lattices has a stable coefficient of friction and exhibits wear debris removal by the self-cleaning effect due to the ordered geometry and designed porosity lattices [26]. An increase of wear resistance is expected after post-processing. One more study direction could be application of metal–ceramic lattice structures as a porous acoustic material [27] with predefined geometry. Their application

as stacks [28] for thermoacoustic energy harvesting [29] is expected to be more efficient compared with the use of stacks produced by traditional manufacturing or similar lattices made from metal. Post-treatment of metallic lattices resulted in phase transformation and, as a consequence, change of thermal and acoustic properties.

4. CONCLUSIONS

In this study metal AISI 316L lattices were produced by selective laser melting and post-processed by thermochemical treatment in methane and nitrogen. The following conclusions can be drawn:

- Nitriding and carburizing transformed the metallic lattice structure into a metal–ceramic composite material.
- Hardness increased about three times compared to untreated specimens in both cases.
- Compressive yield strength of carburized lattices increased on average 10 MPa, which corresponds to 21–65% increase depending on lattice density. The elastic modulus increased on average in the range from 16% to 46%.
- Carburized lattices were found to be more efficient than nitrided ones due to their higher strength and slightly higher plasticity with comparable hardness.

ACKNOWLEDGEMENTS

Table 3. Results of compressive test

Lattice relative density [%]	Compressive yield strength [MPa]		Ultimate fracture stress [MPa]		Elastic modulus [GPa]		
	Untreated	Carburized	Nitrided	Carburized	Untreated	Nitrided	Carburized
19.6	10.95	18.5	27	21	0.42	0.96	0.59
24.7	19.2	30	31.2	33	1.08	1.25	1.10
32.6	33.35	42	44.6	69	1.51	2.2	1.95
41.1	54.8	66.7	60.7	99.3	1.76	2.33	2.31

Proceedings of the Estonian Academy of Sciences, 2019, 68, 2, 131–139

REFERENCES

1. Yan, C., Hao, L., Hussein, A., and Raymont, D. Evaluations of cellular lattice structures manufactured using selective laser melting. *Int. J. Mach. Tool. Manu.*, 2012, **62**, 32–38.

2. Yang, L. Experimental-assisted design development for a 3D reticulate octahedral cellular structure using additive manufacturing. *Rapid Prototyping J.*, 2015, **21**(2), 168–176.

3. Shishkovsky, I., Yadroitsev, I., Bertrand, Ph., and Smurov, I. Alumina-zirconium ceramics synthesis by selective laser sintering/melting. *Appl. Surf. Sci.*, 2007, **254**, 966–970.

4. Davydova, A., Domashenkov, A., Sova, A., Movtchan, I., Bertrand, P., Desplanques, B., et al. Selective laser melting of boron carbide particles coated by a cobalt-based metal layer. *J. Mater. Process. Technol.*, 2016, **229**, 361–366.

5. Shahzad, K., Deckers, J., Zhang, Z., Kruth, J. P., and Vleugels, J. Additive manufacturing of zirconia parts by indirect selective laser sintering. *J. Eur. Ceram. Soc.*, 2014, **34**, 81–89.

6. Leu, M. C., Pattnaik, S., and Hilmas, G. E. Investigation of laser sintering for freeform fabrication of zirconium diboride parts. *Virtual Phys. Prototyp.*, 2012, **7**, 25–36.

7. Riedel, R., Mera, G., Hauser, R., and Klonczynsky, A. Silicon-based polymer-derived ceramics: synthesis properties and applications – a review. *J. Ceram. Soc. Jpn.*, 2006, **114**, 425–444.

8. Eckel, Z. C., Zhou, C., Martin, J. H., Jacobsen, A. J., Carter, W. B., and Schaedler, T. A. Additive manufacturing of polymer-derived ceramics. *Science*, 2016, **351**, 58–62.

9. Barrallier, L. Classical nitriding of heat treatable steel. In *Thermochemical Surface Engineering of Steels* (Mittemeijer, E. J. and Somers, M. A. J., eds). Woodhead Publishing, 2015, 392–411.

10. Van Wiggen, P. C., Rozendaal, H. C. F., and Mittemeijer, E. J. The nitriding behaviour of iron-chromium-carbon alloys. *J. Mater. Sci.*, 1985, **20**, 4561–4582.

11. Edenhofer, B., Joritz, D., Rink, M., and Voges, K. Carburizing of steels. In *Thermochemical Surface Engineering of steels* (Mittemeijer, E. J and Somers, M. A. J., eds). Woodhead Publishing, 2015, 485–554.

12. Suard, M., Martin, G., Lhuissier, P., Dendievel, R., Vignat, F., Blandin, J. J., and Villeneuve, F. Mechanical equivalent diameter of single struts for the stiffness prediction of lattice structures produced by Electron Beam Melting. *Addit. Manuf.*, 2015, **8**, 124–131.

13. Yan, C., Hao, L., Hussein, A., Bubb, S. L., Young, P., and Raymont, D. Evaluation of light-weight AlSi10Mg periodic cellular lattice structures fabricated via direct metal laser sintering. *J. Mater. Process. Technol.*, 2014, **214**, 856–864.

14. Wauthle, R., Vrancken, B., Beynaerts, B., Jorissen, K., Schrooten, J., Kruth, J. P., and Van Humbeeck, J. Effects of build orientation and heat treatment on the microstructure and mechanical properties of selective laser melted Ti6Al4V lattice structures. *Addit. Manuf.*, 2015, **5**, 77–84.

15. Gibson, L. J. and Ashby, M. F. The mechanics of three-dimensional cellular materials. *Proc. R. Soc. A Math. Phys. Eng. Sci.*, 1982, **382**, 43–59.

16. Pye, D. *Practical Nitriding and Ferritic Nitrocarburizing*. ASM International, Materials Park, Ohio, 2003.

17. Parrish, G. *Carburizing: Microstructures and Properties*. ASM International, Materials Park, Ohio, 1999.

18. Hussainova, I., Ivanov, R., Stamatin, S. N., Anoshkin, I. V., Skou, E. M., and Nasibulin, A. G. A few-layered graphene on alumina nanofibers for electrochemical energy conversion. *Carbon*, 2015, **88**, 157–164.

19. Drozdova, M., Hussainova, I., Pérez-Coll, D., Aghayan, M., Ivanov, R., and Rodríguez, M. A. A novel approach to electroconductive ceramics filled by graphene covered nanofibers. *Mater. Des.*, 2016, **90**, 291–298.

20. Liu, Y., Yang, Y., Mai, S., Wang, D., and Song, C. Investigation into spatter behavior during selective laser melting of AISI 316L stainless steel powder. *Mater. Des.*, 2015, **87**, 797–806.

21. Wierzba, B. Competition between Kirkendall and Frenkel effects during multicomponent interdiffusion process. *Phys. A Stat. Mech. Appl.*, 2014, **403**, 29–34.

22. Rothman, S. J., Nowicki, L. J., and Murch, G. E. Self-diffusion in austenitic Fe-Cr-Ni alloys. *J. Phys. F Met. Phys.*, 1980, **10**, 383–398.

23. Tolosa, I., Garciandía, F., Zubiri, F., Zapirain, F, and Esnaola, A. Study of mechanical properties of AISI 316 stainless steel processed by "selective laser melting", following different manufacturing strategies. *Int. J. Adv. Manuf. Technol.*, 2010, **51**, 639–647.

24. Chang, C-N. and Chen, F-S. Wear resistance evaluation of plasma nitrocarburized AISI 316L stainless steel. *Mater. Chem. Phys.*, 2003, **82**, 281–287.

25. Muthukumaran, V., Selladurai, V., Nandhakumar, S., and Senthilkumar, M. Experimental investigation on corrosion and hardness of ion implanted AISI 316L stainless steel. *Mater. Des.*, 2010, **31**, 2813–2817.

26. Holovenko, Y., Antonov, M., Kollo, L., and Hussainova, I. Friction studies of metal surfaces with various 3D printed patterns tested in dry sliding conditions. *Proc. Inst. Mech. Eng. Part J J. Eng. Tribol.*, 2018, **232**, 43–53.

27. Auriemma, F. Study of a new highly absorptive acoustic element. *Acoust. Aust.*, 2017, **45**, 411–419.

28. Swift, G. W. and Keolian, R. M. Thermoacoustics in pin-array stacks. *J. Acoust. Soc. Am.*, 1993, **94**, 941–943.

29. Avent, A. W. and Bowen, C. R. Principles of thermo-acoustic energy harvesting. *Eur. Phys. J. Spec. Top.*, 2015, **224**, 2967–2992.

Metall-keraamiliste võrestruktuuride valmistamine selektiivse lasersulatustehnoloogia ja nitreerimise ning karbidiseerimise teel

Yaroslav Holovenko, Lauri Kollo, Marek Jõeleht, Roman Ivanov,
Tetiana Soloviova ja Renno Veinthal

Selektiivne lasersulatustehnoloogia (SLM) võimaldab saada keerulise geomeetriaga kergeid võrestruktuure. Võimalused metall-keraamiliste komponentide ja võrestruktuuride tootmiseks SLM-tehnoloogia abil on siiski piiratud. Käesolevas uurimuses on keskendutud metall-keraamiliste võrestruktuuride saamisele kaheastmelise lähenemise abil, kasutades SLM-i ja järeltöötlust. Roostevabast terasest võrestruktuuridele rakendati nitreerimist ja karbidiseerimist, mille puhul hinnatakse järeltöötlusparameetrite komplekti mõju. Pärast võre töötlemist on Vickersi keskmised kõvaduse väärtused kõrgemad kui algmaterjalil. Vickersi kõvadus nitriiditud ja karbidiseeritud detailide puhul on vastavalt 605 ning 576 HV0.3, samas kui töötlemata 316L terase mikrokõvadus on 210 HV0.3. Suurim keskmine survetugevuse väärtus töötlemata võre puhul oli 60,7 MPa ja karbidiseeritud võre puhul 99,3 MPa.

Publication III
Holovenko, Y.; Antonov, M.; Kollo, L.; Hussainova, I., Friction studies of metal surfaces with various 3D printed patterns tested in dry sliding conditions. *Proceedings of the Institution of Mechanical Engineers, Part J: Journal of Engineering Tribology*, 232 (1), (2018), 43–53.

Original Article

Friction studies of metal surfaces with various 3D printed patterns tested in dry sliding conditions

Y Holovenko, M Antonov, L Kollo and I Hussainova

Abstract

In recent years, 3D scanning and printing of plastics has rapidly matured while printing of metallic parts is only gaining popularity due to required refinements of technology combined with cost- and resources effectiveness for the main components of printers and consumables. The 3D printing allows producing complicated shapes that can be hardly produced by conventional mechanical tools and can provide the functionalization of surfaces. In this work, several different stainless steel (AISI 316 L) surface patterns (flat, gecko's fibrils, dimples, pyramids, mushrooms, mesh, brush, inclined brush) intended for controlling the coefficient of friction were printed with the help of a 3D metal printer by selective laser melting technique. Unidirectional sliding tests were performed with pin-on-disc configuration. Sliding velocity of 5×10^{-3} m/s and continuously increasing load ranged from 5 to 103 N has been applied in the course of "scanning" mode and accompanied by simultaneous recording of the coefficient of friction. A stainless steel (AISI 316) disc counterbody was used in this series of the tests. It was found that the 3D printed structures allow to control the value and stability of the coefficient of friction in a wide range of loads. Microstructural analysis of the worn samples was performed to support the conclusions regarding wear mechanism.

Introduction

Recent developments of additive manufacturing (AM) technique designed to use high power density laser to melt and fuse metallic powders enabled to process different metallic components of medium and small size and required geometry.[1] A selective laser melting (SLM) is one of the additive manufacturing techniques enabling production of complex-shaped objects directly from a metal powder. An advantage of this process is the possibility to manufacture fully-dense metal parts without post-processing.[2] The most commonly used material for SLM is the stainless steel AISI 316 L. Stainless steels are characterized by relatively poor wear and galling resistance, but are often required for the applications where their corrosion resistance in certain environments is of a primary importance.[3] These materials are generally quite soft, and thus are susceptible to many common forms of wear and contact damage.[3] Because of the inherently poor wear resistance of these alloys, the range of their potential applications is limited. Therefore, modification of the surface of stainless steels to change wear properties without compromising other important properties is a challenge.

Nature has found a way to achieve effective tribological performance by variation of surface feature shapes and sizes. Currently, biomimetic approaches for production of tribological materials attract a great attention when addressing new challenges.[4–9] Gorb et al.[5] reported more than twofold higher adhesive properties of a biomimetic mushroom-shaped fibrillar microstructure as compared to a flat surface. Climbing ability of geckos due to fibrillar arrays, which cover their feet, resulted in many attempts to mimic it for engineering materials.[6,7] Study of the effect of hard and soft segments ratio of the bulk polyurethane and microarrays radius on adhesive surface properties was performed in

Department of Mechanical and Industrial Engineering, Tallinn University of Technology, Tallinn, Estonia

Corresponding author:
M Antonov, Department of Mechanical and Industrial Engineering, Tallinn University of Technology, Ehitajate tee 5, 19086 Tallinn, Estonia.
Email: Maksim.Antonov@ttu.ee

Li et al.[7] Voigt et al.[8] focused on the tarsal morphology of the Colorado potato beetle and its friction on different surface types. With the aim of increasing abrasion resistance, a pyramidal tip shape on the surface[9] can also be used. However, if reduction in friction and, therefore, increase the lifetime of parts, is required, the surface can be modified by dimples. The tribological effect of dimpled surface of laser textured stainless steel rings and favourable reduction in coefficient of friction was demonstrated in Qiu and Khonsari.[10] Furthermore, Roy et al.[11] carried out a detailed tribological study of ceramic hip prostheses with micro-dimples arrays and found a nearly 22% and 53% reduction in friction and wear rate, correspondingly.

With an attempt of using 3D metal printing for bio-mimicking and production of unique topographies for controlling tribological properties, the present study is focused on tribological response of different structural patterns produced from AISI 316 L by SLM process.

Materials and methods

SLM process

Stainless steel AISI 316 L powder with particle size of 10–45 μm was used as a material for producing samples with different surface structures by the selective laser melting process (SLM). In general, a finer powder is available and can be used to provide smoother surface of the printed part; however, it has worse flowability influencing uniformity of powder dispersion and resulting in formation of structural defects such as pores, voids, etc. The selective laser melting process was carried out using a *Realizer* SLM50 machine. The controlled parameters were as following (Figure 1 and Table 1): (1) the laser current
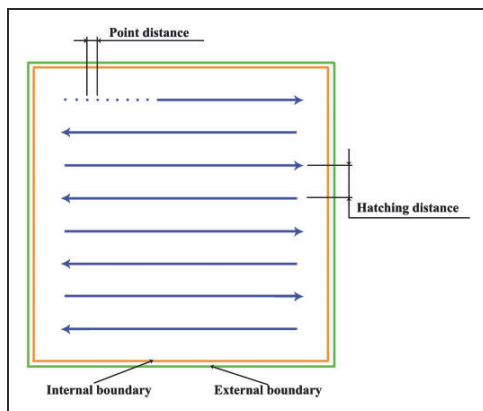
(power), (2) the distance between two neighboring points (point distance) of laser strike (influence) during scanning, (3) the duration of laser strike (exposure time) in each point, (4) the distance between laser hatches (scanning tracks).

Nitrogen was used as a protective atmosphere during the process with an oxygen level less than 0.2 %. To decrease the surface roughness of the outer sections (boundary) of the processed part, the laser current and the point distance were reduced to 1500 mA (36 W) and 10 μm, respectively. The build platform (bed for supporting the 3D structure) was heated up to 200° C prior to and during the printing in order to reduce thermal stresses.

Table 1. The parameters of the SLM process.

Parameter	Value
Thickness of one layer (μm)	25
Hatching distance (μm)	60
Point distance (μm)	20
Laser current (mA) (power, W)	2500 (60 W)
Exposure time (μs)	40
Atmosphere	Nitrogen
Temperature of supporting platform (°C)	200

Figure 1. Illustration of basic SLM process parameters.
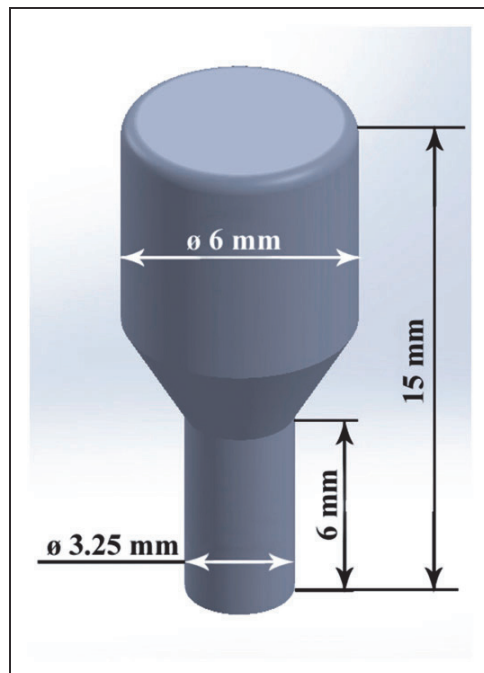

Figure 2. Schematic view of model sample.

Surface patterns

For the current study, the specimens (pins) were modelled with the help of the SolidWorks software. Samples with different surface patterns and the reference flat sample were prepared for comparison of their frictional behavior. A schematic view of the sample model with a flat surface (type 1) is shown in Figure 2. The lower cylindrical part with a diameter of 3.25 mm and height of 6 mm was used for fixation of the sample in the holder of the testing machine. The diameter of the tested part was varied from 6.0 to 7.5 mm depending on the type of the printed sample.

Figure 3 gives the overview of surface pattern types, which were studied in the present work. Table 2 summarizes the main characteristics of the surface patterns being under investigation. Type 1 (Figure 3(a)) is the flat reference surface without any pattern. Types 2 (Figure 3(b)) and 3 are the surfaces with dimples of different sizes. Types 4 (Figure 3(c)) and 5 are the samples with pyramids of a varied height. Types 6 and 7 (Figure 3(d) and (e)) are the mushroom-shaped patterns with either cup-shaped or flat cap. Each small mushroom (type 7) has three pillars (foots) while large mushrooms (type 6) has only one supporting pillar. To simulate gecko's fibrils (pattern type 8), the sample was modelled from cylinders with hierarchically decreased diameter (Figure 3(f)). The smallest cylinder had 170 μm in diameter and 400 μm in height. The next type of the surface pattern was an octet-truss lattice structure (Figure 3(g)). The unit cell size was $1000 \times 1000 \times 1000$ μm^3 and strut diameter was set to be 300 μm (pattern type 9), 200 μm (pattern type 10), or 150 μm (pattern type 11). The last three types of patterns are also mimicking gecko's fibrils but possessing only one level of cylindrical elements (types 12–14). The diameter of cylinders, being in contact with counter-body, is the same for types 8, 12, 13, and 14. Types 12 and 13 are similar to brush with fibrils positioned normally with respect to the support (perpendicularly to the direction of sliding), while the fibrils of type 14
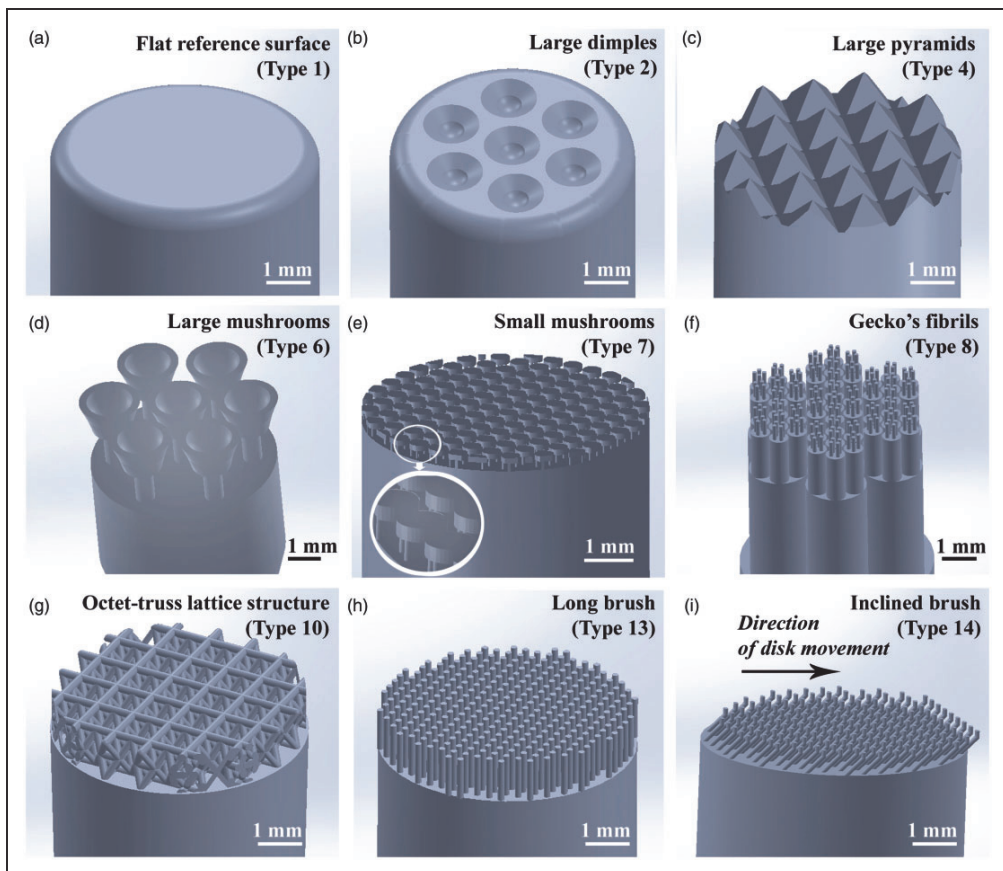
Figure 3. Surface patterns with characteristic features and indication of their types.

Table 2. Description of surface pattern types.

Pattern type	Name of surface pattern	Main characteristic of surface patterns
1	Flat reference surface	No pattern
2	Large dimples	Dimple: $d = 1000$ μm, depth $= 500$ μm, distance $= 1700$ μm
3	Small dimples	Dimple: $d = 400$ μm, depth $= 200$ μm, distance $= 850$ μm
4	Large pyramids	Base: 1400 μm × 1400 μm, $h = 1000$ μm
5	Small pyramids	Base: 500 μm × 500 μm, $h = 500$ μm
6	Large mushrooms with cup-shaped cap	Cap: $d = 1600$ μm, $h = 1000$ μm;
		Foot: $h = 1000$ μm, $d = 500$ μm
7	Linear array of small mushrooms with flat caps	Cap: $d = 500$ μm, $h = 150$ μm;
		Foot: $h = 400$ μm, $d = 100$ μm
8	Gecko's fibrils	First cylinder: $d = 6000$ μm, $h = 3000$ μm
		Second cylinder: $d = 2000$ μm, $h = 4000$ μm
		Third cylinder: $d = 550$ μm, $h = 1650$ μm
		Fourth cylinder: $d = 170$ μm, $h = 400$ μm
9	Octet-truss lattice structure 300	Unit cell size $1000 \times 1000 \times 1000$ μm^3, strut $d = 300$ μm
10	Octet-truss lattice structure 200	Unit cell size $1000 \times 1000 \times 1000$ μm^3, strut $d = 200$ μm
11	Octet-truss lattice structure 150	Unit cell size $1000 \times 1000 \times 1000$ μm^3, strut $d = 150$ μm
12	Short brush	$d = 170$ μm, $h = 500$ μm, step $= 300$ μm
13	Long brush	$d = 170$ μm, $h = 1000$ μm, step $= 300$ μm
14	Inclined brush	$d = 170$ μm, $h = 350$ μm (inclined 45°), $h = 150$ μm (vertical), distance $= 300$ μm

are inclined by 45° with a short cylindrical elements positioned normally to the support. Fibrils of the inclined brush are serving as springs during testing.

Sliding test

Unidirectional sliding tests were carried out with the help of CETR (now Bruker) UMT-2 multi-functional tribo-device in pin-on-disc configuration in dry conditions (without lubrication). The tests were performed in "scanning" mode with the single continuous stepless increase (by 9.8 N in minute) in a load from 5 (start of test) to 103 N (end of test) (0.5–10.5 kg) and continuous recording coefficient of friction (COF) as detailed in Gutsev et al.[12] Duration of the test was 10 min to avoid the complete wear of the structures. This method allows fast estimation of COFs and possible specific changes in frictional behavior in a wide range of loads during a single experiment. Sliding velocity was 5×10^{-3} m/s. The diameter of sliding track was 32 mm. Prior to the test, the disc made from AISI 316 stainless steel and polished to Ra 0.2 μm was cleaned by acetone. Pins of type 1, 2, 3, 6, 8, 9, 10, 11, 12, and 13 were polished by P400 SiC sandpaper with a load of 5 N to improve the parallelism of mating bodies in the CETR UMT-2 device. The roughness of the pin type 1 after polishing was Ra 0.4 μm. Pins of type 4, 5, 7, and 14 were tested without preliminary polishing in as-received conditions. Duration of polishing was varied depending on the type of structure (1–20 min). It was longer for the flat sample (type 1) and shorter for the fine structures like type 8 and 11. After polishing, the sandpaper was substituted by the stainless disc. Tests were repeated at least two times with fresh samples. The test with the same sample of type 11 was repeated four times to study the change in frictional behavior. Examination of the surfaces before and after the experiments was performed by the scanning electron microscope (SEM) Hitachi TM1000.

## Results and discussion

Printed structures

The SEM images of different types of surface patterns are shown in Figure 4. It was initially planned to print the smallest cylinders of gecko's fibrils with the diameter of 140 μm while the fibrils were deformed and distorted during processing. As a consequence, the fibrils with a diameter of 170 μm were successfully prepared and studied (Figure 4(e)). In order to obtain fine structures, an optimization of the processing route in terms of the point distance, laser current and exposure time is required. Bonded powder particles are usually observed on the slope and lateral
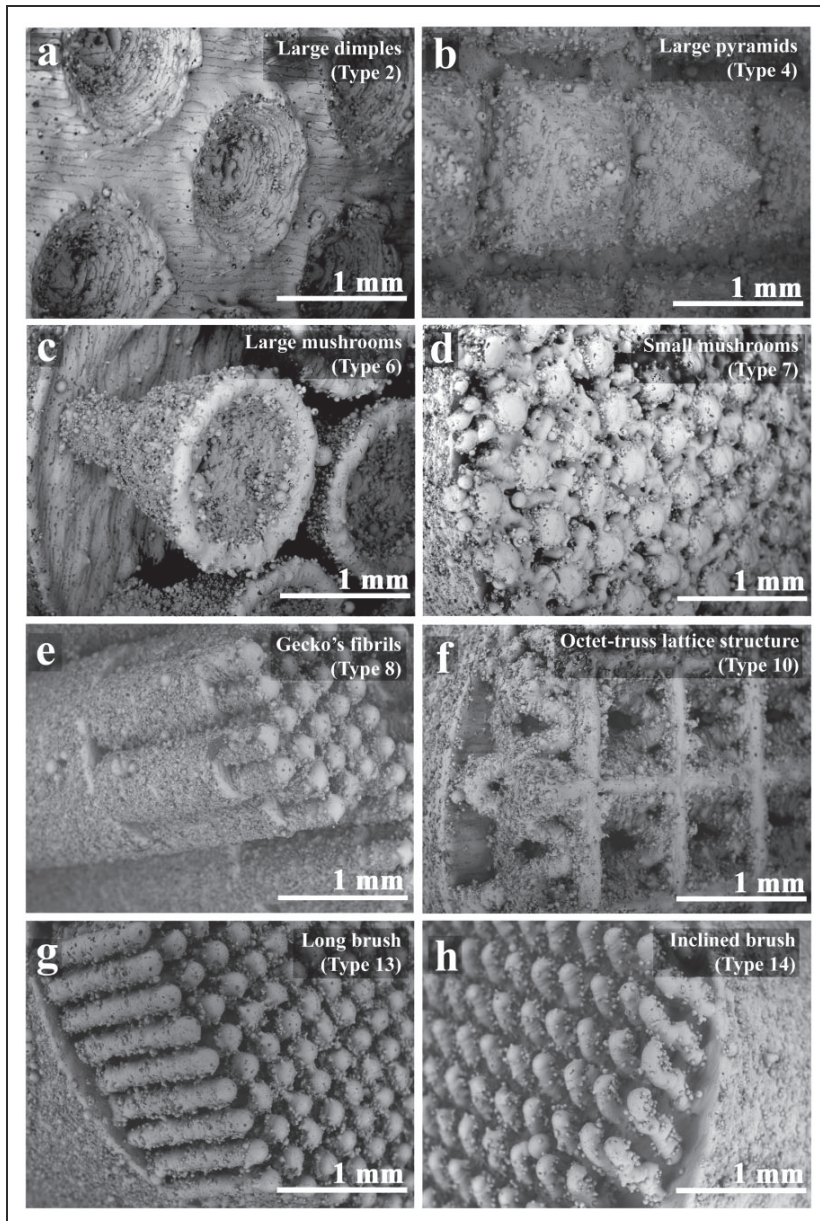
Figure 4. SEM images of 3D printed samples inclined by angle of 45° with the indication of the types.

surfaces independently on the pattern type. Small mushrooms pattern (type 7) exhibits a pronounced distortion as compared to the 3D model (Figures 3(e) and 4(d)) due to SLM process features and current printing resolution. The pyramids shown in Figure 4(b) have quite a sharp tip. Octet-truss lattice with the diameter of 200 μm (Figure 4(f)) and even with the diameter of 150 μm was successfully produced. The edge of dimples (Figure 4(a)) was fully removed during preliminary polishing while large mushrooms had the cup-shaped cap even after polishing (Figure 4(c)). Straight brush patterns are more close to the desired shape while inclined brush fibrils have sufficient distortion (Figure 4(g) and (h)). Laser treatment in SLM process is done point by point, track by track, layer by layer. According to
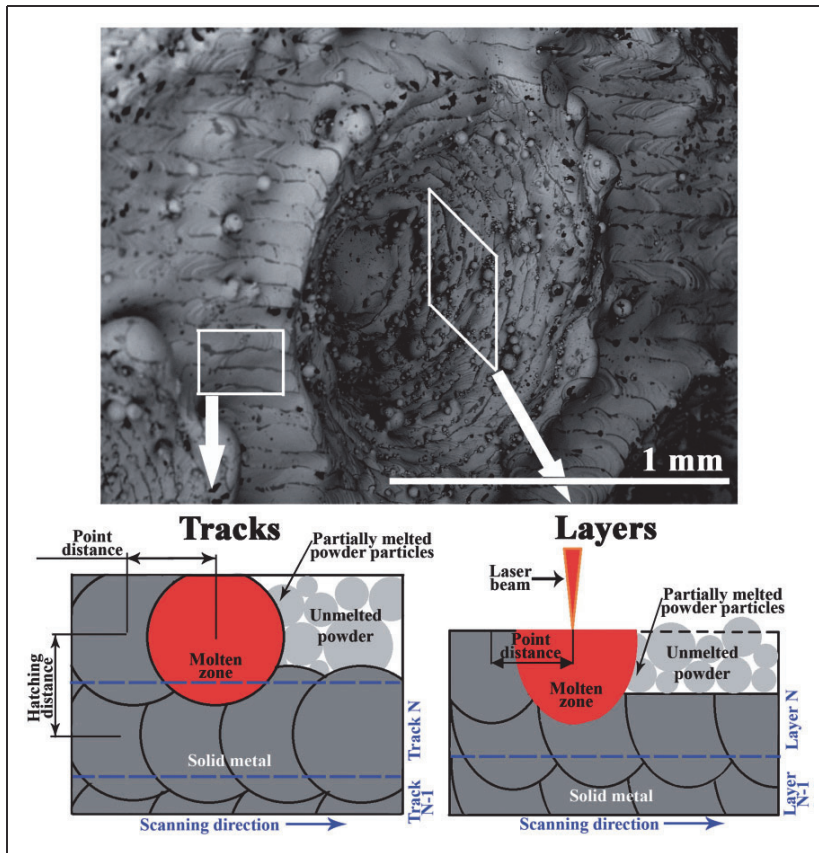
Figure 5. Layers and scanning tracks visible on the surface and schematic explanation of their origin.

such hierarchy of the process, separate layers and scanning tracks can be visible. Figure 5 shows places where tracks and layers related phenomena are clearly observed on the surface of the sample with pattern type 2 (large dimples), which is schematically explained below. As shown on the scheme (Figure 5), a single layer of powder is melted track by track. Each point was in liquid state during some time (called melt pool). The diameter of each circle is determined by the combination of laser power, exposure time, and laser spot size. It is required to provide overlapping of neighboring melt pools and tracks respectively to produce fully solid material. Point distance is a few times smaller than melt pool size to move the melt pool in the liquid state along the track during scanning.

During melting of the next layer, one or few previous (already solidified) layers can be partially or fully remelted depending on layer thickness, laser power, and exposure time. This provides bonding of layers and rise of bulk density. Bonded powder particles (without complete melting) are inevitable and appear on the boundary of the part.

Tribological behavior

Graphs showing the effect of load on the coefficient of friction of various surface patterns are given in Figure 6. The worst frictional behavior was observed in the case of type 1 pattern (flat). COF was rising from 0.2 to 1.0 and was extremely unstable with a high-frequency noise. In order to avoid damage of the device, the test was stopped when the load reached 90 N. Dimples (types 2 and 3) provided a positive effect to the frictional behavior by stabilizing the sliding (reduced variation in COF). The friction force was significantly reduced for the whole range of loads. The large dimples (diameter 1000 μm) were less efficient than the small (diameter 400 μm) dimples while the volume of all dimples and the contact area for both types of samples were similar. The pyramids (types 4 and 5) were able to increase the COF only in the beginning of the test (types 4 and 5). After the load of 15 N (blunting of the tips), the frictional behavior of these samples was similar to the surface with dimples. If high COF is required for a longer time, it is theoretically possible to apply hard thin coatings on
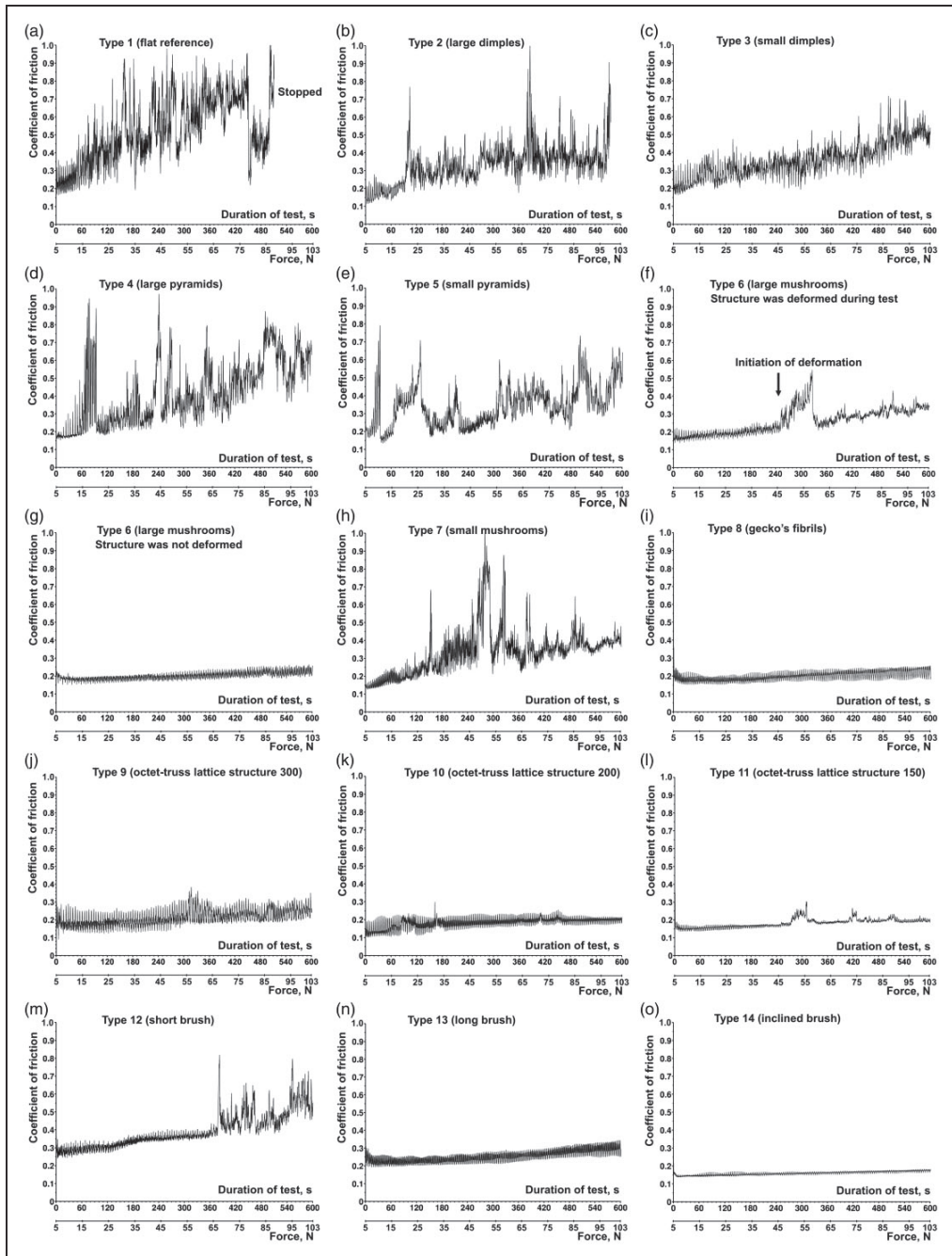
Figure 6. Graphs showing the effect of load on coefficient of friction of various types of surface patterns.

the top of such structures to increase their hardness and reduce wear. Bending and fracturing of the large mushrooms (type 6) and the gecko's fibrils (type 8) was found in some cases (approximately every third

sample was severely deformed). The process of deformation was observed during the test and it was progressive and not abrupt. First single failed element was pushing next elements (features) and finally

causing their failure. Besides, after the failure of the first element the remaining elements experienced higher specific load.

The small mushrooms with the flat caps (type 7) were not providing increased COF in the whole range of loads (as it was expected) and were always fractured during the test since it was not possible to provide preliminary polishing of such structures. As a result, height of all the elements was varied causing overloading of the highest elements, which contact a mating disc, and their progressive deformation. Similar to the large mushrooms (type 6), the gecko's fibrils (type 8) were providing a stable low coefficient of friction in the whole range of loads. This behavior is completely different from what was expected for such type of structures (one of the lowest, instead of highest COF). Figure 7 presents a possible explanation of this phenomenon. In the case of a flat specimen, the solid-phase welding (strong adhesion) of contacting bodies is initiated (Figure 7(a)). The fragment keeping between the bodies is carrying the whole load that results in rolling and sliding of such fragments along the whole diameter (width) of the pin (if it is flat). During the rolling and sliding, the fragment is growing and damaging both the surfaces (Figure 7(b) and (c)). Such rough irregular surface provides conditions for generation of new fragments. In the case of a discontinuous surface consisting of many small elements, the probability for development and growth of wear fragments is reduced. Besides, the space between elements of the surface pattern provides the space for storing of such fragments that

might later escape due to inevitable vibration of bodies and appearance of the gap between them. When the pattern elements are printed with diameters comparable to ones existing in nature (several μm in the case of gecko's finest fibrils) then it will be possible to expect a change in wear behavior and value of COF. The octet-truss lattice (type 9–11), the long brush (type 13), and the inclined brush (type 14) structures are also providing low and stable friction coefficient in the whole range of loads due to the mechanism described above. Types 10 and 11 (the octet-truss lattices with a strut diameter of 200 or 150 μm), 13 and 14 (the long and inclined brushes) are having the lowest COF even at the highest load of 103 N (COF = 0.2) that is five times lower than that observed for the flat sample (type 1, COF = 1.0) providing the evidence of possibility to control the friction by engineering the material surface patterns.

The short brush (type 12) with the length of fibrils being even longer than that of the gecko's ones (while with the same diameter) has increased friction at higher loads. It can be explained by the fact that tips of the gecko's fibrils pattern can be moved to higher distance (in direction of sliding) due to the hierarchical structure. The coefficient of friction of the inclined brush is the lowest and the most stable.

Figures 8 and 9 give some insight on the mechanism of wear of pins and disc. Blunting of the tips of pyramids is seen in Figure 8(a). Metal chips are visible between pyramids. Not all of the empty space between features is filled with the metal debris. The size of such chips is up to 1000 μm in length. The octet-truss
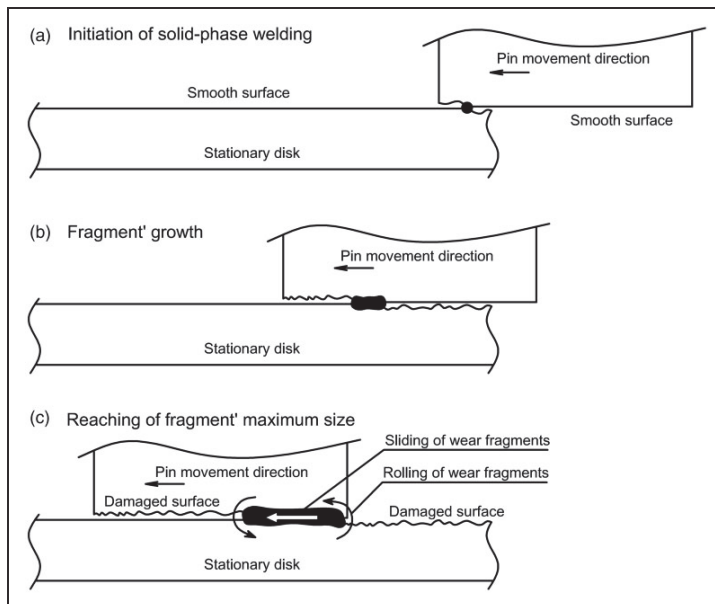

Figure 7. Schematic representation of wear fragments formation in case of flat mating surfaces.

lattice structure with the largest (300 µm) diameter of struts has some gaps that are completely filled by the wear debris (Figure 8(b)) while the same type of structure with the smaller struts (150 µm, type 11, Figure 8(c)) has no visible presence of the wear debris inside the pattern. In all probability, the size of gaps (free space) should be larger than the size of wear debris to provide their cyclic cleaning (removal of debris) due to vibration. COF of the type 9 (octet-truss lattice 300) structure was less stable than that of type 10 or 11 due to clogging of the gaps (Figure 6(j) to (l)). After clogging of the gaps by wear debris, the pattern of type 9 starts to behave similarly to the pattern type 1 (flat). Even higher friction coefficient was observed for the type 12 pattern (short brush) that is explained by complete clogging of the gaps and formation of solid-phase welding spots (Figure 8(d)) similar to that observed in case of the flat mating surfaces. Increase in length of brush fibrils reduces the clogging

(Figure 8(e)). No clogging and worn contact areas at the tips of the inclined brush fibrils are seen in Figure 8(f).

In order to provide confidence on the performance of the self-cleaning process of type 11 structure (the octet-truss lattice 150), the test with the same sample was repeated four times. The behavior during second and third tests was similar while during the fourth test the sudden rise of COF was observed that was caused by wear of the pattern. The COF started to rise as soon as more than 50 % of the height of the octet-truss lattice was removed. Probably, removal of wear debris through the lateral faces was also of high importance. Such removal is not available in the structure with dimples that have higher COF (compare Figure 6(l) and (o) with 6(b) and (c)).

The size of wear fragments present on the surface of the stainless disc are the largest in the case of flat
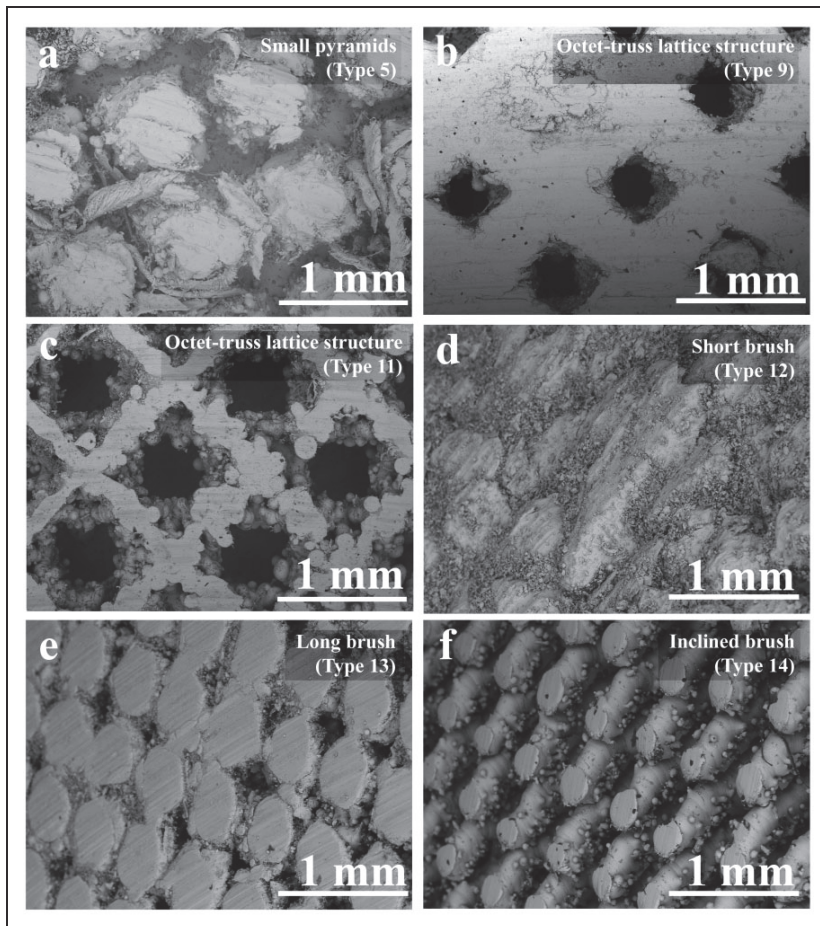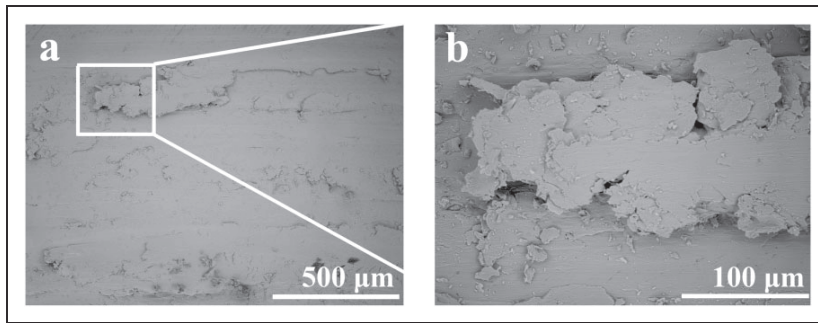

Figure 8. SEM images of the worn structures with indication of types.

Figure 9. SEM image of disc after test with type 1 (flat) pin.

reference sample (Figure 9). They can reach up to 1500 μm in length. Fragments of slightly smaller size are observed in case of the surface with both the large or small dimples (types 2 and 3). The large pyramids and the gecko's fibrils-type patterns (types 4 and 8) produce separated tracks with wear fragments size up to 50 μm. Similar size of fragments is found after sliding wear by the octet-truss lattice structure (type 11). The similarity in size of wear fragments after testing of the large pyramids and the gecko's fibrils-type patterns while taking into account their different coefficients of friction turns to a conclusion that more flexible pattern elements are preferred. They can bypass the irregularities of the counterbody; besides if adhesive bonding takes place then bending of an element can facilitate its withdrawal. The importance of flexibility of elements is confirmed by testing of the inclined brush pattern providing the lowest friction coefficient and almost no damage to the disc. It can be concluded that at least four factors should be taken into account to achieve the low COF of stainless steel tribocouple during dry sliding: (1) minimization and (2) flexibility of surface pattern elements, (3) space for storing of wear debris, (4) removal of wear debris from the storing locations. The results of current work can be used for design of new surface patterns or composite materials intended for various areas of applications where wear and friction aspects are crucial (sliders, clamping parts, plain bearings, etc). It can be expected that patterns having the lowest coefficient of friction in dry conditions will work well under lubricated conditions as well.

Conclusions

The study of frictional behavior of different stainless steel surface patterns prepared by the SLM has been conducted, and the following conclusions can be withdrawn:

- Minimizing of surface pattern elements is limited by the current capability of the SLM machine. It was possible to produce straight columns (pillars) of 170 μm in diameter for gecko's fibrils- and brush-type structures without distortion. The smaller pillar diameter can be achieved by optimizing the SLM parameters.
- The flat reference pin shows the highest and the most unstable values of the coefficient of friction caused by the formation of large (up to 1500 μm in length) wear fragments and solid-phase welding.
- The Gecko's fibrils, octet-truss, long brush, and inclined brush (the best) type structures provided the lowest and the most stable coefficient of friction (COF = 0.2) being up to five times lower as compared to the flat pins.
- The pyramids had a high coefficient of friction only at the first stage of testing before the blunting of tips.

References

1. Hagedorn YC. *Additive manufacturing of high performance oxide ceramics via selective laser melting*. PhD thesis, Aachen University, Germany, 2013.
2. Yan C, Hao L, Hussein A, et al. Evaluations of cellular lattice structures manufactured using selective laser melting. *Mach Tools Manuf* 2012; 62: 32–38.
3. Blau PJ. Friction, lubrication, and wear technology. In: *ASM metals handbook*. vol. 18, 10th ed. New York: ASM International, 1992.
4. Lin D, Nian Q, Deng B, et al. Three-dimensional printing of complex structures: Man made or toward nature. *ACS Nano* 2014; 8: 9710–9715.

5. Gorb S, Varenberg M, Peressadko A, et al. Biomimetic mushroom-shaped fibrillar adhesive microstructure. *J R Soc Interface* 2007; 4: 271–275.

6. He LW, Yan SP, Chu JR, et al. Directional adhesion of gecko-inspired two-level fibrillar structures. *Eur J Mech* 2014; 47: 246–253.

7. Li M, Zhao A, Jiang R, et al. Regulation of the elastic modulus of polyurethane microarrays and its influence on gecko-inspired dry adhesion. *Appl Surf Sci* 2011; 257: 3336–3340.

8. Voigt D, Schuppert JM, Dattinger S, et al. Sexual dimorphism in the attachment ability of the Colorado potato beetle Leptinotarsa decemlineata (Coleoptera: Chrysomelidae) to rough substrates. *J Insect Physiol* 2008; 54: 765–776.

9. Gahlin R and Jacobson S. The particle size effect in abrasion studied by controlled abrasive surfaces. *Wear* 1999; 224: 118–125.

10. Qiu Y and Khonsari MM. Experimental investigation of tribological performance of laser textured stainless steel rings. *Tribol Int* 2011; 44: 635–644.

11. Roy T, Choudhury D, Ghosh S, et al. Improved friction and wear performance of micro dimpled ceramic-on-ceramic interface for hip joint arthroplasty. *Ceram Int* 2015; 41: 681–690.

12. Gutsev D, Antonov M, Hussainova I, et al. Effect of SiO_2 and PTFE additives on dry sliding of NiP electroless coating. *Tribol Int* 2013; 65: 295–302.

Publication IV

Auriemma, Fabio; **Holovenko, Yaroslav,** Performance of Additive Manufactured Stacks in a Small Scale Thermoacoustic Heat Engine. *SAE Technical Paper 2019-01-1534*, (2019), 1–10.

Performance of Additive Manufactured Stacks in a Small Scale Thermoacoustic Heat Engine

Fabio Auriemma and Yaroslav Holovenko Tallinn University of Technology

Abstract

Thermoacoustic heat engines (TAHEs) are external combustion engines primarily designed to convert thermal power into acoustic power and, eventually, into mechanical, electric or other forms of high grade power. TAHEs rely on the presence of a porous core, often referred to as "*stack*". A temperature gradient is established along the porous core and quasi-adiabatic heat exchanges occur between the solid walls of the pores and the surrounding gaseous medium undergoing pressure fluctuations. The internal geometry of the stack has tremendous impact on the efficiency of thermal-to-acoustic power conversion.

In this study, the selective laser melting (SLM) has been used to produce stacks. The SLM is an additive manufacturing (AM) technique designed for 3D metal printing. It is based on high power- density laser which melts and fuses metallic powders together. Three sets of stacks, provided with different hydraulic radii and internal geometries, have been produced. Each set is constituted by two stacks with similar hydraulic radii, one with internal parallel plates and one with internal oblique pin array. The SLM provides precise control of the features of the printed object, allowing to explore geometries which are difficult to manufacture with conventional technologies but, possibly, more effective in the heat exchange process. This is the case of pin (and oblique pin) array geometries, which provide a reduced amount of viscous losses when the working fluid has Prandtl number Pr < 1, e.g. air.

The printed stacks have been tested in a small scale standing-wave TAHE set up in Tallinn University of Technology (TalTech). Temperatures are monitored in proximity of the hot and cold heat exchangers, as well as the sound pressure within the engine resonator. The measured quantities are shown in time and frequency domain to analyze the onset and the stability of the thermoacoustic phenomenon.

Introduction

Thermal-to-acoustic power conversion has been effectively reproduced in Rijke and Sondhauss tubes since the '50s of the 19th century [1]. Lord Reyleigh described this effect as the result of providing heat to acoustic waves at the moment of greatest condensation and detracting heat at the moment of greatest rarefaction (Rayleigh's criterion) [2]. Rott first published the governing equations in 1969 [3]. However, the largest contributions to the development of TAHEs came later, with the works by Swift and coworkers, since 1983 [4]. The Swift's textbook, published in 2001, is still regarded as a fundamental reference in this field [5].

A TAHE is a device where low grade thermal energy is partially converted into acoustic waves with high sound pressure levels. The acoustic waves generated in TAHEs can be harvested in many different ways, for instance into purely mechanical energy, into electric energy, or used as sound excitation in thermoacoustically driven thermoacoustic refrigerators. There are several advantages of thermoacoustic devices - heat engines and refrigerators - related to the intrinsic simplicity of these machines: low number of constituting components, at most one moving part, low-weight, high reliability, non-polluting working fluid (air or any inert gas), low fabrication and maintenance costs.

The porous core is the most important component of the TAHE. Located within a waveguide sandwiched between a hot and a cold heat exchanger, it is subject to a temperature gradient along the direction of the gas particle displacement. Due to its high heat capacity, the porous core acts as a thermal reservoir providing irreversible heat exchanges between the solid, immobile, surface and the surrounding fluid. In order for the thermal-to-acoustic power conversion to occur, the above mentioned Reyleigh's criterion must be satisfied. This means that the hot and cold sides of the porous core are able to, respectively, provide and take away sufficient heat during, respectively, the phase of greatest condensation and that of greatest rarefaction. This condition results in sound amplification of waves at the frequency of the first - most unstable - acoustic mode of the device. The necessity of having a *porous* element is related to the fact that heat exchanges take place within the so called *thermal boundary layer* (δ_k), which has submillimeter thickness and requires similar order magnitude of the pore size. The whole process is regulated by the phase shift between pressure, particle velocity and temperature fluctuations of the medium within the porous material. Due to

the presence of submillimetre apertures within the stack, the thickness of the *viscous boundary layer* (δ_v) is also of the same order magnitude of the pore size. Technically, the Shear number ($Sh = d/2\delta_v$, where d is a characteristic dimension of the pores) is $\mathcal{O}(1)$. As a consequence, large viscous losses take place in the fluid within the stack. This condition, typically utilized in sound absorptive elements (see [6, 7]), is undesired in TAHEs which, inevitably, suffer from substantial viscous losses [5].

TAHEs can be generally categorized into two groups: standing-wave and travelling-wave, according to the phase difference between pressure and acoustic velocity oscillations. This paper aims to explore the potentiality of additive manufacturing in form of selective laser melting (SLM) for the production of the porous core for small scale standing-wave TAHE. In this engine, the waveguide is a quarter-wavelength resonator (a closed-open tube) and the porous core is typically referred to as *stack*, according to the original terminology of Swift [5].

In a standing-wave TAHE, the stack should be able to provide local heat capacity for the fluid while ensuring temporally isothermal boundary condition and minimizing viscous dissipation [5]. Stacks made of loose-weave screens and reticulated vitreous carbon (RVC) have been proven to work reasonably well, also in travelling-wave TAHEs, [8, 9, 10]. On-shelf commercial metal, ceramic and plastic honeycombs can be used, as well, as inexpensive stacks. From the studies by Rott [3] and by Arnott et al. [11] on circular, square, rectangular and triangular pores, it is possible to conclude that parallel sided pore geometries exhibit better performance than other hollow pore geometries. The spiral configuration is one way to build stacks with approximately parallel sided pores [5]. Spiral stacks can also be made with long spacers parallel or nearly parallel to the longitudinal dimension, for example by using minute nylon "rods" such as monofilament fishing line as spacers [12]. However, Swift et al. [13] have theoretically shown that stacks with convex pores geometries, e.g. pin array stacks, perform better than any hollow pore stack, including parallel plate stacks. In fact, in this case a smaller amount of viscous losses is involved in the thermoacoustic process if the working fluid has Prandtl number (Pr) < 1, e.g. air [13]. Nonetheless, pin array stacks are extremely difficult to build accurately, especially for small gas thermal penetration depths (i.e., high pressure or high frequency). Manufacturing issues further increase for oblique pin array stacks which, on the other hand, would have the advantage of having longer pins (thus, reduced heat flow) between the hot and the cold ends of the stack.

Recent trends have seen tremendous growth of the potentialities of additive manufacturing also to print features of submillimetre size. The application of additive manufacturing for production of stacks for TAHE is a new and, to the authors' knowledge, not yet sufficiently explored subject. In this paper, three sets of stack geometries, manufactured by SLM, are tested by monitoring temperatures and sound pressure levels in a small scale standing wave TAHE. Each set includes one stack with parallel plates and one with oblique pin array provided with similar hydraulic radii. Different sets are characterized by different hydraulic radii. This study will be followed by an upcoming investigation about the

optimization of the performance of metal 3D printed stacks including the use functionally graded materials (see [14, 15, 16, 17, 18]).

Theoretical Background

A schematic representation of a standing-wave TAHE is shown in figure 1, which also includes the pressure/particle velocity distribution within the resonator at the first natural frequency and a magnification of fluid particle motion within the stack. In this device, imperfect heat transfers between the gas and the solid material are realized to produce significant time delay between the movement of the gas and its expansion (or contraction) to meet Rayleigh's criterion, see figure 2a. In fact, if the thermal contact was too poor (e.g. in large pore or ducts) the gas would not experience any heat exchange at all with the solid walls, as in figure 2b. On the other hand, if the thermal contact was perfect, the gas temperature would remain simply close to that of the stack and no thermodynamic cycle would be experienced (see figure 2c). If the thermal contact is imperfect but the thermal gradient is so that the particle temperature matches the temperature of the stack, the thermoacoustic effect does not yet occur and the situation is still qualitatively similar to that of a perfect thermal contact. However, that temperature gradient is referred to as "critical temperature gradient" because a small increase of that gradient establishes the thermoacoustic *effect*.

The previously mentioned non-dimensional parameters, i.e. the thermal boundary layer (or thermal penetration depth)

Standing-wave thermoacoustic heat engine. a) Schematic setup; b) pressure and particle velocity field; c) heat exchange of fluid particle within the stack.
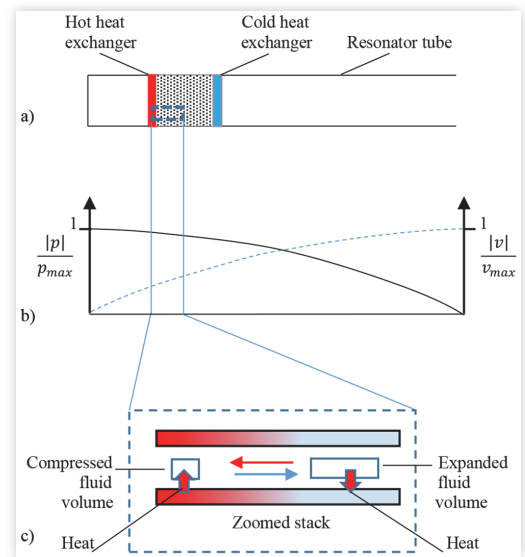
FIGURE 2 Temperature distribution of the stack (straight lines) and of the particles (ellipses) vs particle displacement (x). a) imperfect thermal contact, b) poor thermal contact; c) nearly perfect thermal contact / critical temperature gradient.
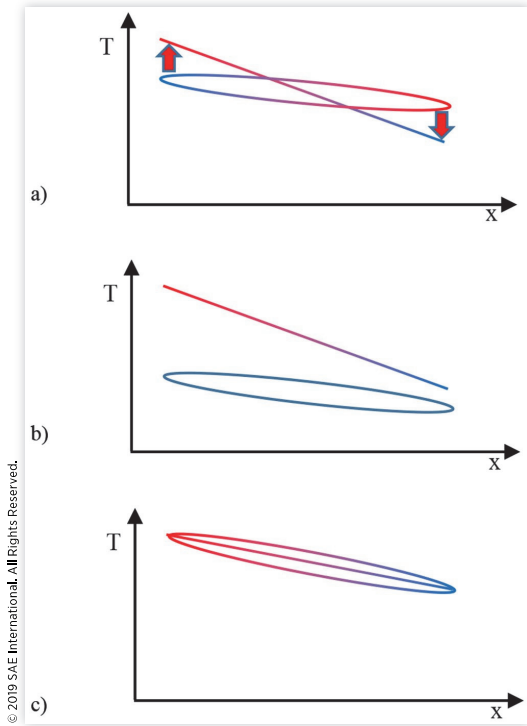
and the viscous boundary layer (or viscous penetration depth), are mathematically defined as:

$$\delta_k = \sqrt{\frac{2\kappa}{\omega}} \quad \text{and} \quad \delta_v = \sqrt{\frac{2\mu}{\omega}}, \tag{1}$$

Here κ is the thermal diffusivity of the medium and v is its kinematic viscosity. δ_κ and δ_v represent a measure of the length scale for the oscillatory thermal and viscous diffusion. In other terms, δ_κ and δ_v are the distances from the solid wall where heat and momentum can diffuse laterally during the time T/π, where T is the period of the acoustic oscillation (see [19], [20], [21]). At longer distances, the fluid responds adiabatically to the acoustic perturbation, whilst in the very proximity of the walls the response is isothermal. At intermediate distances of order δ_κ the response is somehow in the between ("imperfect" thermal contact) representing the condition typically desired in standing-waves TAHEs.

The Prandtl number of the gas, defined as the ratio:

$$\Pr = \frac{v}{\kappa} = \left(\frac{\delta_v}{\delta_\kappa}\right)^2 \tag{2}$$

is close to unity for typical gases, so viscous and thermal penetration depths are comparable. This explains why

thermoacoustic heat engines and refrigerators typically suffer from substantial viscous effects [5]. However, more precisely, Pr is 0.71 for air (and for several other gasses) at 20°C and slightly decreases up to 350 °C. This means that the viscous penetration depth is slightly smaller than the thermal penetration depth. This fact can be advantageously used to build stacks where the total volume involved in the thermal diffusion, V_κ, is sensibly larger than the total volume involved in the viscous losses, V_v. This goal can be achieved by using stacks provided with internal convex surfaces, such as pin-array stacks, instead of concave surfaces, such as hollow pores of any shape.

In figure 3, the cross sections of a pin-array stack and of a circular pore-array stack are represented. In the figure, the thermoacoustic and viscous areas (A_κ and A_v respectively), corresponding to the cross sections where thermal and momentum diffusions occur, are quantitatively shown as well. From figure 3 it is easy to deduce that convex radii of curvature, of the order of δ_κ or δ_v, increase the ratio A_κ/A_v significantly in comparison with concave radii [12]. Obviously, the situation represented in figure 3b is the worst case scenario (i.e. circular pores) for stack with concave surfaces. When the stack is constituted by parallel plates the surfaces involved in the thermo-viscous effects are flat and concave at the vertexes, thus the ratio A_κ/A_v is higher than in circular pore stacks but still lower than that of pin-array stacks.

In mathematical terms, the linearized equation of motion can be used to relate the acoustic particle velocity (u_1) and the pressure in the stack (p_1) according to the equation proposed by Rott [3]:

$$\langle u_1 \rangle = -\frac{1}{i\omega\rho_m}\frac{dp_1}{dx}\left(1 - f_v\right) \tag{3}$$

where < > is the spatial average, i is the imaginary unit, ω is the angular frequency, ρ_m is the mean gas density and f_v is typically referred to as "the Rott's function" [3]. f_v is a function of δ_v and of the distance from the solid wall. In the

FIGURE 3 Qualitative sketch of thermoacoustic and viscous areas (A_k and A_v) involving thermal and momentum diffusion in: a) pin-array stack, b) circular pore-array stack.
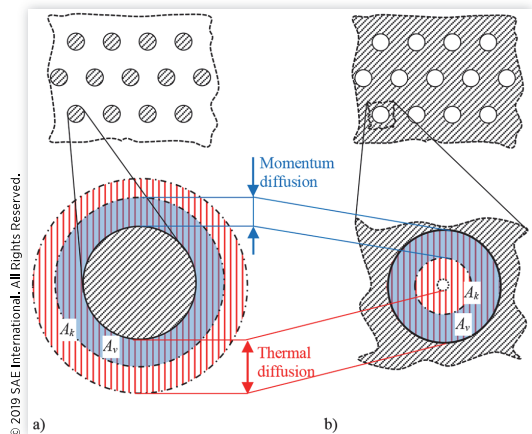
hypothesis of isothermal solid-fluid interface, an equation similar to Eq.3 can be derived to relate the spatial average of the oscillating temperature, $<T_1>$, to p_1. In this case, a function f_κ is used, anyhow related to f_v. In [11] it has been proven that thermoacoustic heat transport and work are proportional to $\mathrm{Im}[f_\kappa]$, in the standing-wave inviscid limit, and that acoustic power dissipated by viscosity is proportional to $\mathrm{Im}[f_v]/|1 - f_v|^2$ when $dT_m/dx = 0$. As a consequence, in [12], the ratio $\sqrt{\mathrm{Pr}}\,\mathrm{Im}[f_\kappa][1-f_v]^2/\mathrm{Im}[f_v]$ has been used as a figure of merit for comparison of different stack geometries. The figure of merit of pin-array stacks has been shown to be significantly superior to other stack geometries for a large range of radii of the pins and for Prandtl numbers typical of gases [12]. This circumstance thoroughly explains what has been intuitively observed by looking at the figure 3.

Another important factor which affects the behavior of the stack is the thermal conduction along the direction of particle displacement. The thermal conduction must be sufficiently low to guarantee the temperature difference, along the stack, responsible for the thermal-to-acoustic power conversion. As the heat flow is proportional to the cross-sectional area of the stack made of solid material, it results that pin-array stacks are favored, in comparison with other geometries, because the amount of solid fraction in the stack is minimized. Furthermore, oblique pins present the advantage of having longer pins arranged between the hot and the cold ends of the stack, thus less heat is transmitted. Although considerations about viscous and thermal effects would lead to design pin-array stacks with arbitrarily small diameter of the stack, this is generally not a good choice. In fact, in order for the stack to behave as a thermal reservoir, the gas-solid interface must remain temporally isothermal along the stack. To this aim, it is necessary to find a trade-off for the diameter of the pins because too small diameters would result in too small heat capacity and the temperature of the pins could be affected by the pressure fluctuations.

The comparison between stacks in focus in this paper is based on the assumption that the hydraulic radius (R_h), i.e. the ratio of gas area to solid perimeter in the generic cross section, is an independent variable. In other words, stacks provided with different internal geometries but similar hydraulic radii are compared. This assumption is generally valid for straight pore stacks, such as parallel plate and parallel pin array stacks and it has been used in this work also for oblique pin array stacks.

SLM Process for Stack Production

The selective laser melting (SLM) is a powder bed fusion process which provides part building by selective melting of metallic powder layer by layer. For the production of the stacks used in this work, the SLM has been performed by a Realizer SLM50® machine. Stainless steel AISI 316L powder with particle size 10-45 μm is used as a feedstock. The thermal conductivity of AISI 316L is 16.3 W/mK and 21.5 W/mK, at 100°C and 500°C respectively.

In the production process, CAD and beam models of stacks are sliced into layers with 0.35 μm thickness. Each slice contains the scanning information. Two different types of scanning strategies have been applied in the present study in order to produce stacks consisting of parallel plates and pin arrays. (figure 4). Parallel plates have been printed by using boundary scanning and hatches. Hatch direction undergoes 60° rotation at each new layer (figure 4a). The distance between two neighboring hatches is set to 60 μm.

To produce pin array stacks, lattice structures have been printed by using pulsed laser scanning strategy. Now, one slice of the lattice beam model contains a set of discrete points which define the coordinates of the laser exposure (figure 4b). The thickness of the struts, in this case, is related to the melt pool size and it is defined by the combination of laser power and exposure time in each point.

For plate stacks the laser power utilized has been ~60 W, the scanning speed for boundaries has been 0.25 m/s and 0.4 m/s for hatches. For the lattice structures of the pin array stacks the laser power utilized has been ~70 W and the exposure time 700 μs. The SLM process has been performed

FIGURE 4 Scanning strategies for parallel plates and lattice structure for: a) parallel plate stack, b) pin array stack.
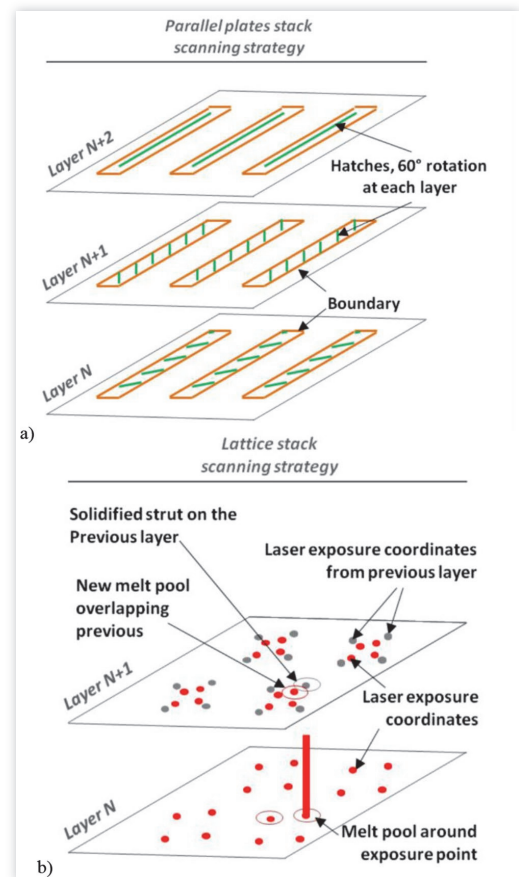
in nitrogen protective atmosphere keeping oxygen level less than 0.2 %. Porous stacks can also be obtained directly by SLM or by using indirect methods in order to improve material properties (see [22, 23]).

Characteristics of the Stack Samples

The Table 1 contains the main geometrical parameters of the stacks, including the sizes of the CAD models, as well as the real-as-printed parts. The parameter D represents the thickness of the plates or the diameter of the pins, H is the distance between plates or pins, ρ is the porosity (ratio between fluid and solid volumes in the stack) and HD is the hydraulic radius, previously defined. In figure 5, a photo of two samples and the scanning electron microscopy (SEM) of the same specimens (performed with an Hitachi TM1000 microscope) are shown as well. The side surface in both cases is covered by bonded particles which stick to the melt pool or are partially melted. However, the geometrical data related to real-as-printed stacks have been calculated by neglecting the presence of bonded particles, since these ones are difficult to take into account due to their random nature. Moreover, some of the bonded particles are removed by means of mechanical vibrations. No CAD data are provided in Table I for the sample S6 because this sample has a diamond-shaped lattice structure resulting from a simple set of coordinates of laser exposure points, where no thickness is involved.

TAHE Setup

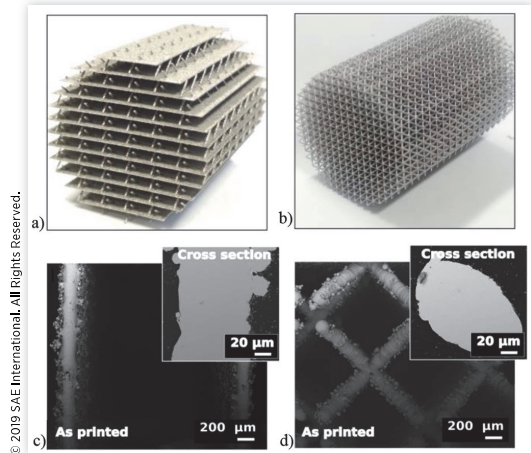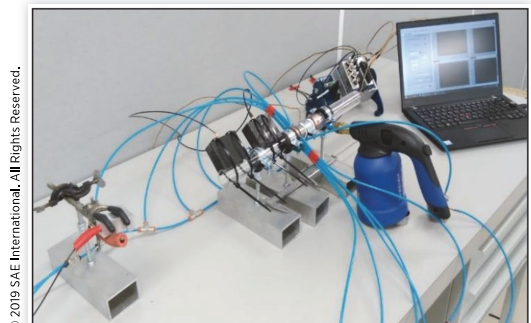The TAHE set up implemented in the Acoustic Laboratory of Tallinn University of Technology (TalTech) is shown in

figure 6. It consists of a focused heat source, a resonator tube, two heat exchangers and a porous stack.

The tube resonator has diameter $D_r = 28mm$, length $L_r = 640mm$, first resonance frequency $F_r = 132$ Hz. The hot heat exchanger, located next to the heat source, heats up the first end of the stack, whilst the cold one cools down the second end. The temperatures are monitored by means of 2 k-thermocouples located in proximity of the hot and cold heat exchangers. The sound is measured by a set of three ¼" prepolarized pressure microphones (type 40BD G.R.A.S.®, equipped with preamplifiers 26CB G.R.A.S.®): an external one, placed at 150mm from the open-end, and two flush-mounted ones with separation distance s1 = 150 mm. The signal acquisition has been performed by a dynamic signal analyzer (National Instruments® NI NIcDAQ 9174 and NI 9234), controlled by PC based virtual instrument (LabVIEW®).

TABLE 1 Main geometrical parameters of the stacks.

Sample name	Stack type	Domain	D [mm]	H [mm]	ρ	HD [mm]
S1 (VIII)	Parallel plates	CAD	0,16	0,9	0,819	0,354
		Real	0,18	0,88	0.766	0,329
S2 (IV)	Oblique pins	CAD	0.16	0.9	0.916	0.464
		Real	0.18	0.89	0.873	0.370
S3 (II)	Parallel plates	CAD	0,15	0,75	0,813	0,280
		Real	0,18	0,73	0,787	0,286
S4 (VII)	Oblique pin	CAD	0,19	0,65	0,892	0,408
		Real	0.21	0.63	0,869	0,343
S5 (XII)	Parallel plates	CAD	0,16	2	0,921	0,869
		Real	0,18	1,98	0,912	0,859
S6 (XI)	Oblique pins	CAD	-	-	-	-
		Real	0.18	1,5×1,5×2*	0,964	0,864

* A diamond shaped lattice structure has been used for Sample S6 and the size of the unit cell is provided here.

FIGURE 6 Setup of the TAHE.

Results

All tests shown in this paragraph include the measurement of the acoustic pressure, performed by the microphone located at 200 mm from the open end, and the plot of the temperature difference measured by the thermocouples. It is important to notice that, since the thermocouples are located in proximity of the heat exchangers, there is always a gap between the measured temperatures and the temperatures of the hot and cold ends of the stack.

The results shown in figures 7 to 12 are related to tests conducted by using the same heat flow, for which equal temperature slopes are exhibited over time in the first part of the tests. On the other hand, the results shown in figures 13 to 16 are obtained by using higher heat power and the

FIGURE 7   Thermoacoustic behavior of stack S01.
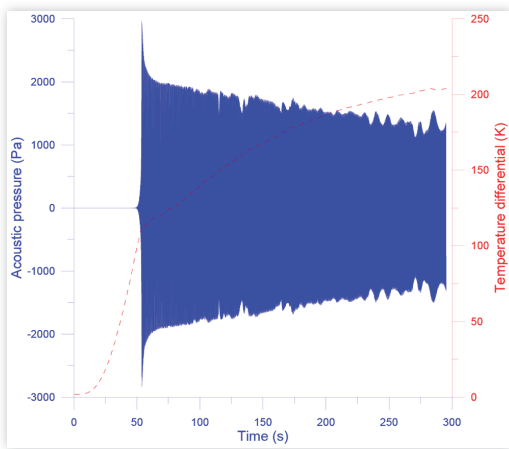
FIGURE 8   Thermoacoustic behavior of stack S02.
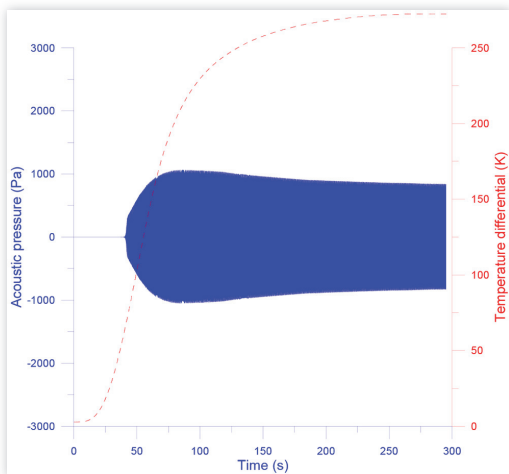
FIGURE 9   Thermoacoustic behavior of stack S03.
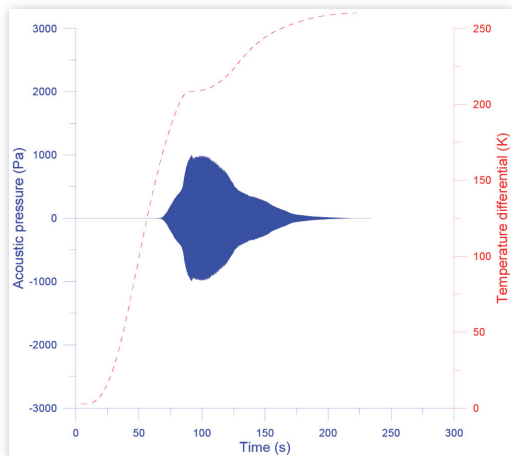
FIGURE 10   Thermoacoustic behavior of stack S04.
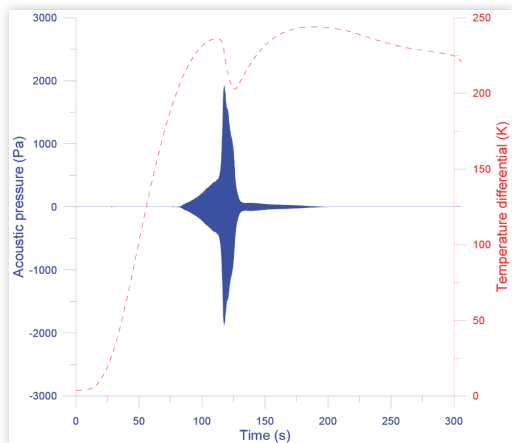
temperature slopes are slightly steeper, at least at the beginning of the tests. In general, when the temperature difference between the ends of the stacks reaches a certain threshold (100-150 K), the thermoacoustic *effect* takes place and the temperature distribution within and around the stack is strongly affected by the thermo-fluid-dynamic characteristics of the stack. Generally, when large thermal-to-acoustic conversions begin, high acoustic pressures and particle velocities are generated which can reduce the slope of the temperature difference curve.

In figures 7 and 8, the results of the tests of the first two samples, S01 and S02, are shown. The stacks have similar hydraulic radii (HR ~0.33m for S01 and 0.37mm for S02), but S01 is provided with parallel plates whilst S02 with oblique pins. In the first case, the acoustic emission becomes evident around the 50th second with a fast increase of pressure

FIGURE 11 Thermoacoustic behavior of stack S05.
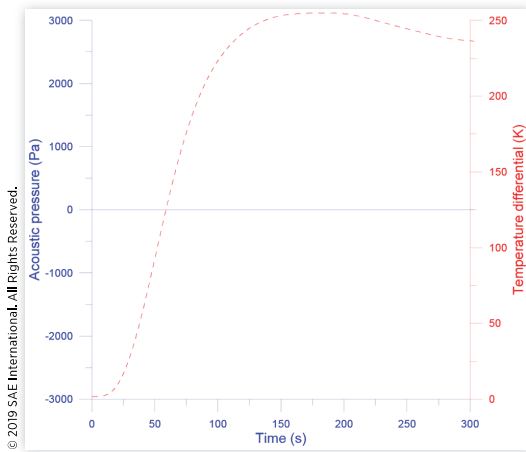
FIGURE 12 Thermoacoustic behavior of stack S06.
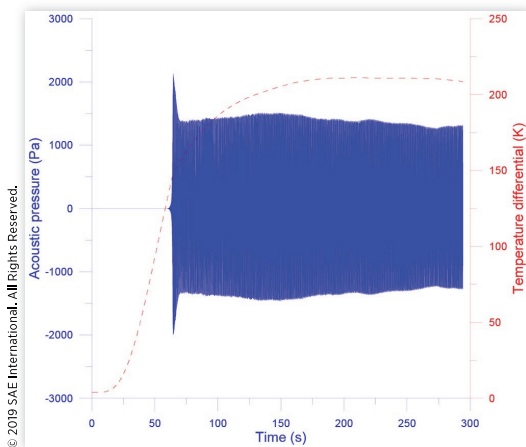
FIGURE 13 Thermoacoustic behavior of stack S01 with greater heat power.

amplitude, up to ~2800 Pa, and a subsequent sudden decrease, down to ~1800 Pa, occurring in ~ 6 seconds. From the 62nd second the behavior is more stable but there is a constant decrease of amplitude of ~ 6.4 Pa/s. Moreover, evident fluctuations in the pressure amplitudes are evident, especially in the last part of the test. On the other hand, for the sample S04, the acoustic emission becomes evident after a shorter time interval, i.e. at the 40th second. The increase of sound emissions is smooth for the subsequent 45 seconds when the pressure amplitude reaches ~1060 Pa. A gradual descent of amplitude follows, until the it stabilizes, towards the end of the test, at ~ 850 Pa.

The results related to the second set of samples, S03 and S04 (with HI~0.29 mm and HI~0.34mm, respectively), are plotted in Figures 9 and 10. Here, by means of a relatively small reduction of the hydraulic radii, a remarkable drop in the acoustic performance is exhibited. In fact, by

comparing these results with the ones in figures 7 and 8, the onset of the thermoacoustic effect is delayed, the pressure amplitudes are smaller and the sound emissions cease after ~ 140 seconds (for S03) and ~ 110 seconds (for S04) from the onset. The slope of the temperature difference increases when the thermoacoustic effect reduces. Most likely, for S03 a slight decrease and subsequent stabilization of the temperature difference would follow after the time monitored. In case of S04, the decrease of temperature difference is visible already.

Finally, S05 and S06 are the stacks with parallel plates and oblique pin array, provided with the largest hydraulic radii (HR~0.86mm in both cases). As mentioned earlier, the sample S06 is characterized by a diamond shaped lattice structure. This structure has been found to be a feasible option to provide enough mechanical resistance to stacks with oblique pins and high porosity. The corresponding results are plotted in figures 11 and 12. From the latter one it is possible to notice that, for the conditions provided in our tests, there is no major conversion of heat into sound and the temperature difference follows the trend of a conductive material which undergoes heating on one end.

Conversely, the behavior of S11 shown in figure 12 is marked by an evident thermal-to-acoustic conversion after approximately 60 seconds. A sharp peak of ~2100 Pa is exhibited followed by a drop to a more stable level, from second 73 to the end of the test, with magnitudes ~1350 Pa. The temperature difference has a smooth trend because the oblique pin array is characterized by low heat transmission due to the small cross section and the orientation of the pins. The temperature difference stabilizes around 210 K.

Due to the very different behaviors of S05 and S06, despite the almost identical hydraulic radii, it is possible to confirm that the HR parameter cannot be considered as unique independent parameter when comparing straight pores (as in parallel plate stacks) with tortuous pores (as with oblique pin stacks provided with diamond shaped lattice structure).

The samples S01 and S06 have been tested also by using greater heat power. The results are shown in figure 13, for S01, and in figures 14 to 16 for S06. In the first case, the trend shown in figure 7 with the smaller heat power is confirmed. Now the pressure magnitudes are larger and the decrease rate is ~4.5 Pa/s. However, after ~210 s from the beginning of the sound emissions, the acoustic pressure drops and, in the time interval of ~10 seconds, the engine shuts down. Also in this case, the temperature difference exhibits a reduction in slope when the thermoacoustic conversion begins.

As previously pointed out, the graph of temperature differences plotted in these figures does not represent the actual temperature difference between the hot and cold ends of the stack. The latter is rather the temperature difference measured close to the heat exchangers. This difference increases at the shut-down because the cooling effect, related to the heat transport exerted by the acoustic waves, ceases. On the contrary, most likely the shut-down is related to the
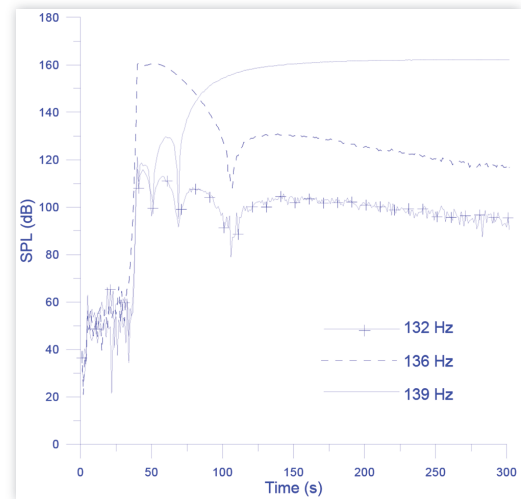
FIGURE 14 Thermoacoustic behavior of stack S06 with greater heat power.
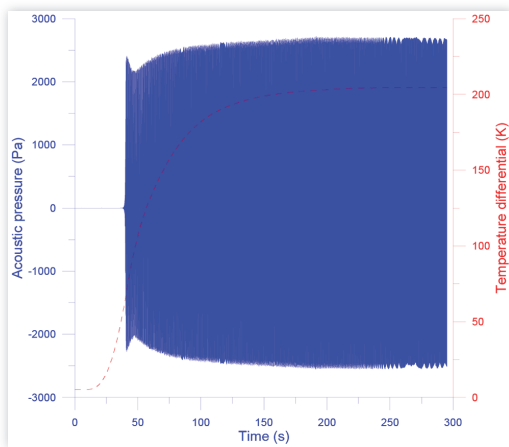
FIGURE 15 Contour plot showing the time dependence of the frequency spectrum in the test of the stack S06 with greater heat power.
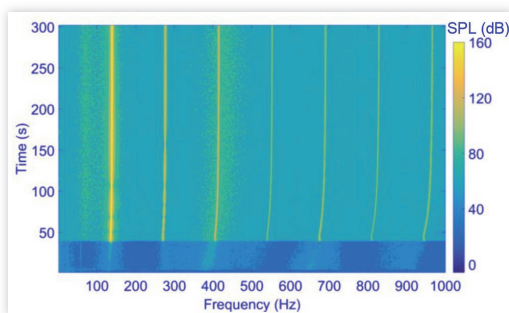
FIGURE 16 Sound pressure level measured at the frequencies 136 Hz and 139 Hz in the test of the stack S06 and greater heat power.

reduction of the temperature gap, between the hot and cold end of the stack, below the critical value. This circumstance is not directly visible in the graphs, which show the effect (the increase of the temperature gap between the heat exchangers) rather than the cause (decrease of the temperature gap between the ends of the stack) of the engine shut down.

The figure 14 shows the behavior of the sample S06 when greater heat power is applied. The thermoacoustic conversion is particularly efficient, which is noticeable from: the anticipated onset, occurring at ~38 s; the pressure levels reached (up to ~2700 Pa, corresponding to 163 dB); the short transient and the stability of the behavior until the end of the test. Moreover, the temperature difference exhibited at the end of the test is very similar to the one shown in figure 12, despite the greater heat power used now. Clearly, this fact shows that a larger fraction of heat power has been converted into acoustic power, indicating an essentially nonlinear thermoacoustic behavior of the stack.

For completeness, other two graphs are shown in figures 15 and 16, representing the time dependence of the sound pressure levels measured in the test of the stack S06 with greater heat power. In the first case, a contour plot is presented, containing the sound frequency content in the range 20-1000 Hz. As expected, the largest contribution to the sound emissions derives from the resonance frequency of the device (132 Hz) but higher harmonics are also excited. To be precise, the plot shows that: the largest contribution is given at the frequency 139 Hz; minor influence is given by the first subharmonic; the 5th and 7th harmonics provide larger contribution than the 4th and 6th ones. These characteristics of the acoustic field within the resonator are deeply related to the non-linear behavior exhibited by the TAHE when high pressure levels are reached.

In this regard, it is also interesting to look at the results in figure 16, where the sound pressure levels at the frequencies 132 Hz, 136 Hz and 139 Hz are plotted as functions of time. The first frequency of the set is the theoretical resonance frequency of a 640mm long quarter wave resonator, purely related to the nominal length of the resonator. However, the major contribution at the onset of the thermo-acoustic emission is provided at the frequency 136 Hz, where the sound pressure level abruptly reaches ~ 160 dB at ~38 s. After the onset, the sound pressure level at 136 Hz decreases over time, but contemporarily the level at 139 Hz increases up to 162 dB with tendency to stabilize. This behavior is likely related to the non-linear energy transfer occurring between different frequencies in non-linear regimes ([5, 24]). Non-linear energy transfer also takes place at the higher order harmonics, as clearly visible in figure 14 for the 7th harmonic.

Conclusions

This paper assesses the possibility of using additive manufacturing in form of selective laser melting (SLM) to 3D print porous cores (stacks) for a small scale standing-wave thermoacoustic heat engine. A number of stack samples have been produced by using steel powder in the SLM process and tested within the engine by monitoring acoustic pressure within the resonator tube and temperatures in proximity of the heat exchangers. Two types of geometries have been investigated: stacks with internal parallel plates and stacks with internal oblique pins. Samples provided with the same hydraulic radii have been compared.

Stacks with internal parallel plates exhibit unstable behavior characterized by initial transient with high pressure amplitudes followed by a constant decrease of the amplitudes. This condition can, eventually, end up in engine shut-down. The slope of the temperature difference monitored next to the hot and cold exchangers reduces during the thermoacoustic conversion due to the cooling effect of the standing waves. The thermoacoustic behavior of the parallel plate samples is largely affected by the heat conduction occurring along the plates. This parameter has not been directly monitored, but it is most likely the main reason for the decrease of sound pressure amplitudes in parallel plate stacks.

Samples provided with oblique pin array, difficult to manufacture in a controlled way with traditional technologies, are obtained by printing lattice structures. The sample tested with lowest hydraulic radius exhibits an excellent behavior characterized by high acoustic pressure amplitudes and stability over time. In this case, the temperature difference shows a smooth trend with tendency to stabilize over time. The frequency spectrum of the sound pressure level exhibits typical non-linear behavior with non-linear energy transfers. The remarkable performance of oblique pin array stacks can be ascribed to three factors: the low heat transmission throughout the stack due to the small cross section of the pins; the oblique displacements of the pins which increases the actual length in the heat transmission; the reduced ratio between momentum diffusion (viscous effects) and thermal diffusion occurring for convex geometries in fluids like air.

References

1. Bisio, G. and Rubatto, G., "Sondhauss and Rijke Oscillations, Thermodynamic Analysis, Possible Applications and Analogies," *Energy* 24(2):117-131, 1999.

2. Rayleigh, J.W.S., *The Theory of Sound vol. II* (London: Macmillan, 1878).

3. Rott, N., "Damped and Thermally Driven Acoustic Oscillations in Wide and Narrow Tubes," *Z. Angew. Math. Phys.* 20:230, 1969.

4. Wheatley, J.C., Hofler, T., Swift, G.W., and Migliori, A., "Understanding Some Simple Phenomena in Thermoacoustics with Applications to Acoustical Heat Engines," *American Journal of Physics* 53(2):147-162, 1985, doi:10.1119/1.14100.

5. Swift, G.W., *Thermoacoustics - A Unifying Perspective for Some Engines and Refrigerators* (New York: Acoustical Society of America, 2002).

6. Auriemma, F. and Tiikoja, H., "On the Acoustic Impedance of a Fibreless Sound Absorptive Element," *SAE Int. J. Engines* 8(5):2268-2275, 2015, doi:10.4271/2015-24-2462.

7. Auriemma, F., Rämmal, H., and Lavrentjev, J., "Extended Investigations on Micro-Grooved Elements - A Novel Solution for Noise Control," *SAE Int. J. Mater. Manf* 7(1):184-194, 2014, doi:10.4271/2013-24-0068.

8. Hofler, T.J. and Reed, M.S., "Measurements with Wire Mesh Stacks in Thermoacoustic Prime Movers," *Journal of Acoustical Society of America* 99:2559, 1996.

9. Adeff, J.A., Hofler, T.J., Atchley, A.A., and Moss, W.C., "Measurements with Reticulated Vitreous Carbon Stacks in Thermoacoustic Prime Movers and Refrigerators," *Journal of Acoustical Society of America* 104:32-38, 1998.

10. Abduljalil, A.S., Yu, Z., Jaworski, A.J., "Performance Studies of Travelling-Wave Thermoacoustic Engine for Selected Low-Cost Regenerators," in *Proceedings of SEM Annual Conference*, Albuquerque NM, June 1-4, 2009.

11. Arnott, W.P., Bass, H.E., and Raspet, R., "General Formulation of Thermoacoustics for Stacks Having Arbitrarily Shaped Pore Cross Sections," *J. Acoust. Soc. Am.* 90:3228, 1991.

12. Hofler, T.J., "Thermoacoustic Refrigerator Design and Performance," Ph.D. thesis, Physics Department, University of California, San Diego, CA, 1986.

13. Swift, G.W. and Keolian, R.M., "Thermoacoustics in Pin-Array Stacks," *Journal of Acoustical Society of America* 94:941-943, 1993.

14. Aiello, R. and Auriemma, F., "Optimized Vibro-Acoustic Design of Suspended Glass Panels," *Structural and Multidisciplinary Optimization* 58(5):2253-2268, doi:https://doi.org/10.1007/s00158-018-2014-3.

15. Majak, J., Kuttner, F., Pohlak, M., Eerme, M. et al., "Application of Evolutionary Methods for Solving Optimization Problems in Engineering," in *Proceedings of NordDesign, 39-48, NordDesign 2008 Conference*, Tallinn, Estonia.

16. Majak, J., Pohlak, M., Karjust, K., Eerme, M. et al., "New High Order Haar Wavelet Method: Application to FGM

Structures," *Composite Structures* 201:72-78, doi:10.1016/j.compstruct.2018.06.013.

17. Shvartsman, B.S., Majak, J., and Kirs, M., "Numerical Method for Stability Analysis of Functionally Graded Columns," in *Proceedings of the International Conference of DAAAM Baltic Industrial Engineering, Volume 2014, 65-70. 9th International Conference of DAAAM Balti*, Tallinn, Estonia, 2014.

18. Dragonetti, R., Napolitano, M., Di Filippo, S., and Romano, R., "Modeling Energy Conversion in a Tortuous Stack for Thermoacoustic Applications," *Applied Thermal Engineering* 103:233-242, 2016, doi:10.1016/j.applthermaleng.2016.04.076.

19. Tiikoja, H., Auriemma, F., and Lavrentjev, J., "Damping of Acoustic Waves in Straight Ducts and Turbulent Flow Conditions," SAE Technical Paper 2016-01-1816, 2016, doi:10.4271/2016-01-1816.

20. Tiikoja, H., Lavrentjev, J., Rämmal, H., and Åbom, M., "Experimental Investigation of Sound Reflection from Hot Subsonic Flow Duct Termination," *Journal of Sound and Vibration* 333:788-800, 2014, doi:10.1016/j.jsv.2013.09.030.

21. Auriemma, F., "Study of a New Highly Absorptive Acoustic Element," *Acoustics Australia* 45(2):411-419, 2017, doi:10.1007/s40857-017-0087-6.

22. Holovenko, Y., Kollo, L., Jõeleht, M., Pohlak, M. et al., "Effect of Hot Isostatic Pressing on Cellular Lattice Structures Obtained by Selective Laser Melting," in *World PM2016 Congress & Exhibition*, Hamburg, Germany, October 9-13, 2016, European Powder Metallurgy Association.

23. Minasyan, T., Liu, L., Aghayan, M., Kollo, L. et al., "A Novel Approach to Fabricate Si3N4 by Selective Laser Melting," *Ceramics International* 44:13689-13694, 2018, doi:10.1016/j.ceramint.2018.04.208.

24. Moezzi, R. and Auriemma, F., "Observation of Nonlinear Vibro-Acoustic Phenomena in the Presence of Elastic Membrane with Different Boundary Conditions," in *Euronoise 2018*, Crete, EAA, HELINA, ISSN: 2226-5147.

Contact Information

Corresponding author:
Fabio Auriemma
TalTech - Tallinn
University of Technology
Ehitajate tee 5, 12616, Tallinn
fabio.auriemma@taltech.ee

Acknowledgements

Curriculum vitae

Personal data

Name: Yaroslav Holovenko
Date of birth: 17.04.1992
Place of birth: Dubno, Rivne region, Ukraine
Citizenship: Ukraine

Contact data

E-mail: yaholo@taltech.ee, yaruk.ssa@gmail.com

Education

2015–2019 Tallinna Tehnikaülikool (TalTech) – PhD
2013–2015 National Technical University of Ukraine 'Kyiv Polytechnic Institute' – MSC
2009–2013 National Technical University of Ukraine 'Kyiv Polytechnic Institute' – BSC
1999–2009 Dubno state school №6

Language competence

Ukrainian – Native
English – Fluent
Russian – Fluent
Estonian – Basic

Professional employment

2014–2015 National technical university of Ukraine "Kiev Polytechnic Institute", Research Assistant
2015–2015 Navigator NII, engineer
2018–2019 FACT industries, additive manufacturing consultant

Projects

IUT19-29 "Multi-scale structured ceramic-based composites for extreme applications (1.01.2014–31.12.2019)", Principal investigator: Jakob Kübarsepp, Tallinn University of Technology, School of Engineering, Department of Mechanical and Industrial Engineering.

B56 "Innovative polycrystalline diamond (PDC) drag bit for soft ground tunnel boring machines (1.05.2016–30.04.2019)", Principal investigator: Maksim Antonov, Tallinn University of Technology, School of Engineering, Department of Mechanical and Industrial Engineering.

Intellectual property

Invention: Multifunctional composite material and method for its preparation; Owners: Tallinna Tehnikaülikool; Authors: Maksim Antonov, Yaroslav Holovenko; Priority number: P201900006; Priority date: 24.01.2019.

Elulookirjeldus

Isikuandmed
Nimi: Yaroslav Holovenko
Sünniaeg: 17.04.1992
Sünnikoht: Dubno, Rivne maakond, Ukraina
Kodakondsus: Ukraina

Kontaktandmed
E-post: yaholo@taltech.ee, yaruk.ssa@gmail.com

Hariduskäik
2015–2019 Tallinna Tehnikaülikool – PhD
2013–2015 Ukraina Riiklik Tehnikaülikool "Kiievi Polütehniline Instituut" – MSC
2009–2013 Ukraina Riiklik Tehnikaülikool "Kiievi Polütehniline Instituut" – BSC
1999–2009 Keskharidus

Keelteoskus
Ukraina keel – Emakeel
Inglise keel – Kõrgtase
Vene keel – Kõrgtase
Eesti keel – Kesktase

Teenistuskäik
2014–2015 Ukraina Riiklik Tehnikaülikool "Kiievi Polütehniline Instituut", teadur assistent
2015–2015 Navigator NII, insener
2018–2019 FACT industries, lisaaine tootmise konsultant

Projektid
IUT19-29 "Mitmeastmeliselt struktureeritud keraamika-baasil komposiitmaterjalid kasutamiseks ekstreemtingimustes (1.01.2014–31.12.2019)", Vastutav täitja: Jakob Kübarsepp, Tallinna Tehnikaülikool, Mehaanikateaduskond, Tallinna Tehnikaülikool, Inseneriteaduskond, Mehaanika ja tööstustehnika instituut .

B56 "Innovatiivsed polükristallilisest teemandist kuluvosad pehme pinnase tunneli puurimisseadmete tarbeks (1.05.2016–30.04.2019)", Vastutav täitja: Maksim Antonov, Tallinna Tehnikaülikool, Inseneriteaduskond, Mehaanika ja tööstustehnika instituut.

Tööstusomand
Patentne leiutis: Multifunktsionaalne komposiitmaterjal ja meetod selle valmistamiseks; Omanikud: Tallinna Tehnikaülikool; Autorid: Maksim Antonov, Yaroslav Holovenko; Prioriteedi number: P201900006; Prioriteedi kuupäev: 24.01.2019.